Spring 2022

Observing and Modeling Water Electrolysis Performance Limitations Attributed to Gas Generation and Porous Media Properties

Joseph S. Lopata

Observing and Modeling Water Electrolysis Performance Limitations Attributed to Gas Generation and Porous Media Properties

by

Joseph S. Lopata

Bachelor of Science
Rochester Institute of Technology, 2016

Submitted in Partial Fulfillment of the Requirements

For the Degree of Doctor of Philosophy in

Chemical Engineering

College of Engineering and Computing

University of South Carolina

2022

Accepted by:

Sirivatch Shimpalee, Major Professor

John W. Weidner, Committee Member

William E. Mustain, Committee Member

Parastoo Hashemi, Committee Member

Melissa A. Moss, Committee Member

Tracey L. Weldon, Interim Vice Provost and Dean of the Graduate School

DEDICATION

For my grandfather, Vern Moffatt, in memoriam.

“When the going gets tough, the tough get going.”

ACKNOWLEDGEMENTS

Funding for this research was obtained from the University of South Carolina, the National Science Foundation (NSF) Integrated Graduate Education and Research Traineeship (IGERT) program, the Department of Energy (DOE) Office of Science Graduate Student Research (SCGSR) fellowship, Korea Institute of Energy Research (KIER), Guangju Institute of Science and Technology (GIST), the Energy Research and Development Institute (ERDI) at Nakornping, and BASF.

Simulations were built with Star-CCM+, from Siemens Product Lifecycle Management (PLM) Software. CAD geometries were designed in Solidworks, from Dassault Systèmes. The open-source platform ImageJ was used in parts of this research.

This work was possible with the kind help of my advisor, Dr. Sirivatch Shimpalee; my doctoral committee consisting of Dr. John W. Weidner, Dr. William E. Mustain, and Dr. Parastoo (Parry) Hashemi; the helpful experts who hosted me and assisted with experimental setups at the National Renewable Energy Laboratory (NREL), Dr. Guido Bender, Dr. Bryan Pivovar, Consuelo Montano, Dr. Zhenye (Allen) Kang, James Young, Ellis Klein, Alex Badgett, and Dr. Shawn Alia; my fellow colleagues Dr. Pongsarun (BOOM) Satjaritanun, Dr. Drew J. Pereira, Dr. Ben Meekins, Kris Likit-Anurak, Mitchell Sepe, and Hunter Teel; my friends Dr. Christopher Isely, Dr. Charles Fricke, Dr. Gregory Tate, Utkarshani Jaimini, Candice Cheung, Dr. Kate McCullough, Cody Wilkins, Stephanie Sanchez, Dr. Pravin Bosco, and Dr. Jeremiah Lipp; and, of course, my supportive parents, grandparents, and sister.

ABSTRACT

Water electrolysis has been a simple method of hydrogen production for over two centuries, but the exploration of its nuances is still accelerating. This work compiles numerous mechanisms via which electrolysis efficiency is influenced by phenomena that occur within, adjacent to, and nearby functional porous media. Computational and experimental methods are applied to electrolysis systems to quantify the impact of two-phase flow patterns and porous media properties on energy losses, primarily those linked directly to the presence of the gas phase.

First, an introduction to the chemistry and operating principle of water electrolysis is presented and relevant works from the literature are compiled and summarized in order to explain important topics that are still under investigation. The pseudo-two-phase mixture model employed to study fluid flow in three-dimensional cell geometries is described later, followed by demonstrations of its use simulating proton exchange membrane and alkaline diaphragm water electrolysis devices. In these studies, the kinetic limitations attributed to the gas-phase reaction are computed across entire electrodes to elucidate the connection between fluid flow and the local gas evolution reaction environment. Finally, detailed experimental investigations of the effects of porous transport layer surface properties are presented in order to draw conclusions concerning two-phase transport at interfaces between the separator/catalyst-coated membrane and adjacent functional porous media.

PREFACE

This dissertation is intended to be a guide for the new students that join electrochemical groups at the University of South Carolina. Of course, it is open for everyone interested to read. Some sections of the introduction explain concepts that are widely known among the electrochemical community, but perhaps not to the general scientific public. This should be a helpful resource for anyone wishing to become involved in electrochemical research, particularly pertaining to electrolysis. Those individuals may want to continue the path of this work or at the least use the bibliography. Hopefully, many who read this will discover that there are many branches that can grow from the ideas comprised within (whether they originate here or elsewhere), and that our collective understanding of phenomena within electrolysis systems still scratch the surface of what can be discovered.

TABLE OF CONTENTS

LIST OF TABLES

LIST OF FIGURES

LIST OF SYMBOLS

A	Area
$\underline{\boldsymbol{A}}$	Control volume surface area vector
A^*	Dimensionless specific area
a	Activity
$\boldsymbol{a}$	Example vector (see Appendix)
B	Bulge parameter
b	Bruggeman approximation exponent
$\boldsymbol{b}$	Example vector (see Appendix)
$\mathcal{B}$	Bulge factor
$\mathscr{b}$	Ratio of the maximum ion transport radius to the separator thickness
C	Molar concentration
c_P	Constant-pressure specific heat capacity
D	Diffusion coefficient
$\mathcal{D}$	Dinkelacker function
$\underline{\underline{\boldsymbol{E}}}$	Strain tensor
F	Faraday's constant
$\underline{\boldsymbol{f}}$	Body force vector
f	Favorability
G	Specific Gibbs free energy

H Specific dynamic enthalpy

h Specific static enthalpy

h_r Relative humidity

$\mathcal{H}$ Hofmann parameter

$\underline{\underline{\boldsymbol{I}}}$ Identity matrix

$\underline{\boldsymbol{i}}$ Current density

$\boldsymbol{i}$ Boundary-normal current density

i_0 Exchange current density

$\boldsymbol{J}$ Leverett function

j Transfer current density

j_0 Exchange transfer current density

j_1^* Dimensionless transfer current density at $z^* = 1$

K Mass transfer coefficient

k Relative permeability

L Through-plane distance

l Characteristic length

$\boldsymbol{M}$ Molecular weight

m Molal concentration

$\underline{\boldsymbol{N}}$ Molar flux

N_{Sc} Schmidt number

$\underline{\boldsymbol{n}}$ Mass flux

$\boldsymbol{n}$ Boundary-normal mass flux

P Pressure

$\tilde{P}$	Mixture pressure
Q	Average volumetric flow rate
$\underline{\boldsymbol{q}}$	Heat flux
q	Boundary-normal heat flux
R	Electronic/ionic resistance
$\underline{\underline{\boldsymbol{R}}}$	Porous viscous resistance
$\mathscr{R}$	Universal gas constant
r	Radius
S	Entropy
$\mathcal{S}$	Source term
s	Liquid volume fraction, a.k.a. liquid saturation
s_i	Volume fraction of entity i
T	Temperature
$\underline{\underline{\boldsymbol{T}}}$	Viscous stress tensor
U	Convective heat transfer coefficient
u	Ionic mobility
$\underline{\hat{\boldsymbol{v}}}$	Mass-weighted average velocity
$\underline{\boldsymbol{v}}_L$	Liquid-phase velocity with respect to the grid or geometry
w	Weight fraction
x	Mole fraction in the aqueous phase
y	Mole fraction in the vapor phase
z	Through-plane coordinate
α	Transfer coefficient

γ	Surface tension
ϵ	Porosity
η	Overpotential
θ	Wetting angle
κ	Intrinsic permeability
λ	Thermal conductivity
μ	Dynamic viscosity
ν	Stoichiometric coefficient
ν^{eo}	Electroosmotic drag coefficient
ξ	Rate order
$\underline{\boldsymbol{\xi}}$	Inner normal unit vector
ρ	Density
σ	Electronic/ionic conductivity
τ	Tortuosity
$\Upsilon_{\pm,m}$	Mean molal activity coefficient
υ	Relative mobility
φ	Generalized property
ϕ	Electric potential
$\underline{\boldsymbol{\Phi}}$	Generalized flux
χ	Areal porosity

LIST OF SUBSCRIPTS

a	Anodic
act	Of activation
ad	Alkaline diaphragm
app	Apparent
avg	Average
C	Due to capillary forces
CL	Catalyst layer
c	Cathodic
$cell$	Across the cell
cs	Cross-sectional
cv	Of a control volume
$diff$	Of diffusion or apparent diffusion
e	Of the electrolyte
eff	Effective
eq	At equilibrium
esi	Electrode/separator interface
FF	Flow field
f	Of a face
G	Gas-phase
i	Species i

$i-j$	Of species i moving through species j
$i-m$	Of species i moving through medium m
int	Interfacial
L	Liquid-phase
m	Of the matrix phase
max	Maximum
mt	Of mass transport
p	Diaphragm space between pores
pem	Proton-exchange membrane
PTL	Porous transport layer
S	Superficial
s	Surface
sat	At saturation
set	Setpoint
tk	Thermodynamic and kinetic
tn	Thermoneutral
tot	Total
vap	Of vaporization
w	Liquid water
wv	Water vapor
Δ	Heat
Π	Of phase Π
Ω	Ohmic

∞	Of the surrounding environment
$+$	At the +z side of the boundary
$-$	At the -z side of the boundary

LIST OF SUPERSCRIPTS

co	Due to crossover
eo	Due to electroosmotic drag or electroosmotic flow
$evap$	Due to evaporation
$init$	Initial
new	New
old	Old
red	Reduction
ref	At reference state
rxn	Due to reaction
sat	At saturation
vap	Of vaporization
$\circ$	At standard temperature
$*$	Dimensionless

LIST OF ABBREVIATIONS

%LFL ..... Percentage of the lower flammability limit

1D..... One-dimensional

2D..... Two-dimensional

3D..... Three-dimensional

ADWE..... Alkaline diaphragm water electrolysis

AGSD..... Average grain surface diameter

A-HER ..... Acidic hydrogen evolution reaction

A-OER ..... Acidic oxygen evolution reaction

A-OER(G)..... Acidic oxygen evolution reaction in the gas phase

A-OER(L) ..... Acidic oxygen evolution reaction in the liquid phase

APOD..... Average pore opening diameter

B-HER..... Basic hydrogen evolution reaction

B-OER..... Basic oxygen evolution reaction

CCM..... Catalyst-coated membrane

CFD..... Computational fluid dynamics

CL ..... Catalyst layer

CRC..... Chemical Rubber Company

DI ..... Deionized

DLP ..... Differential liquid pressure

EIS..... Electrochemical impedance spectroscopy

ESI..... Electrode/separator interface

FVM..... Finite volume method

H2P ..... Dry-basis hydrogen purity

HFR.....High frequency resistance

LDH ..... Layered double hydroxide

LGA ..... Dimensionless liquid/gas interfacial area

MEA..... Membrane-electrode assembly

NIST.....National Institute of Standards and Technology

NREL .....National Renewable Energy Laboratory

P2PM.....Pseudo-two-phase mixture

PEMWE .....Proton exchange membrane water electrolysis

PTL ..... Porous transport layer

TC ..... Thermocouple

URF.....Under-relaxation factor

VOF..... Volume-of-fluid

CHAPTER 1

INTRODUCTION

Electrolysis is the non-spontaneous destruction, or lysis, of chemical bonds under sufficient electrodynamic polarization, i.e. a potential difference across which net current and charge transfer is allowed. This dissertation is concerned with the low-temperature electrolysis of liquid water in particular. In a water electrolysis system, deionized water, caustic, lye, or brine is pumped through an electrolysis cell, where it is consumed in an endergonic electrochemical reaction forming hydrogen and oxygen gases,

$$H_2O_{(l)} \rightarrow H_{2(g)} + \frac{1}{2}O_{2(g)} \qquad \Delta G^{\circ}_{rxn} = +237.2 \frac{\text{kJ}}{\text{mol } H_2O} \tag{1.1}$$

which are ideally kept separated and are purified in a downstream process. Most water is unconsumed and the residual water exiting the cell is generally recycled and combined with the infeed. The product gases, especially hydrogen, are saved for electricity generation in a fuel cell, a downstream chemical process, or sale.

Computational fluid dynamics (CFD) is the study or method of solving the equations for the conservations of mass and momentum at a finite number of positions within a flow field using a systematic sequence of improving guesses. It has widespread use in many science and engineering disciplines such as aerospace, internal combustion, meteorology, and chemical processing. The overall reaction in water electrolysis obviously requires water, therefore it is dependent on the flow of water and gas inside the cell. This rationalizes the use of CFD to understand electrolysis processes as it has been utilized to

model other electrochemical systems such as fuel cells (Shimpalee, et al. 2019) and flow batteries (Aparicio-Mauricio, et al. 2020).

Motivation

Hydrogen is an immensely important industrial product used by many industries including agriculture, petrochemicals, food processing, metal fabrication, and aerospace. Most hydrogen is produced from the thermochemical steam reforming of methane gas, which produces carbon dioxide emissions. It also indirectly results in methane emissions from the drilling methods and infrastructure used to extract and transport methane. Due to economies of scale, steam reforming is the most cost-effective way of producing hydrogen in bulk.

However, the costs associated with distributing hydrogen from these centralized sources for energy applications are great. Hydrogen is being considered as an energy carrier in the energy and transportation sectors. Its implementation would result in a large demand increase for hydrogen and, subsequently, natural gas if steam reforming remained the predominant production method. This would incur undue environmental, societal, and economic costs that humanity is beginning to witness as a result of climate change. However, the hydrogen economy is bottlenecked in part by the cost of building and maintaining an extensive hydrogen supply chain. It is costly to distribute large quantities of hydrogen from a centralized source of production. In this scenario, it would be financially beneficial to produce hydrogen gas at small scales where it is consumed in order to avoid costs associated with delivery.

Electrolysis units are generally expensive to operate if not to build them. They require electrical energy, which is relatively costly compared to natural gas. However, with

the declining cost of renewable electricity, variable costs could become practical in years to come. If electrolyzers were powered by excess grid energy that would otherwise be wasted due to harsh demand cycles, they could be economical while also reducing the cost of electrical power production, especially in the context of intermittent renewables such as wind and solar power. The other major cost is that of cell production, which often requires precious or noble metals. One prominent objective of electrolysis research has been to design cell components that reduce catalyst loadings or the amount of material used to construct the electrolyzer. Research itself is fairly costly, with small bench-scale cells easily costing thousands of U.S. dollars each, and potentiostats costing tens of thousands.

CFD modeling can be employed to design cell components such as flow channels, manifolds, and porous media. Developed computational methods can reduce the time and capital involved in research and development by evaluating cell designs and helping to identify areas of improvement, thereby allowing a cell to operate more efficiently and produce satisfactory returns on investment.

Operating Principle

A description of underlying mechanisms and cell assembly components are provided in this section for the two classes of water electrolysis processes studied in this dissertation. These are proton exchange membrane water electrolysis (PEMWE) and alkaline diaphragm water electrolysis (ADWE), classified according to the material used to separate the anode and cathode. Herein the anode is the positive electrode and the cathode is the negative electrode. For those familiar with the opposite convention, this one is chosen to accommodate the study of charge transfer inside the cell, where positive charge

travels from anode to cathode, as opposed to charge transfer in the external circuit, where the opposite is true.

Proton Exchange Membrane Electrolysis.

In PEMWE, water is converted to hydrogen and oxygen under acidic conditions facilitated by the proton-conducting membrane (Carmo, et al. 2013). At the anode, water is oxidized on the surface of a positively polarized electrocatalyst, usually IrO_2, in the acidic oxygen evolution reaction (A-OER). The A-OER requires the catalyst to be in electrical contact with the external circuit and in physical contact with water and an acidic polymer electrolyte. The work of Mo et al. (Mo, Kang and Retterer, et al. 2016, Mo, Kang and Yang, et al. 2017) emphasizes the importance of this so-called triple-phase boundary. Mo et al. (Mo, Kang and Retterer, et al. 2016) used imaging of a transparent cell to visualize bubble generation at the anode, which preferentially occurred where the porous transport layer (PTL) contacted the catalyst layer (CL) at the pore edges. Later (Mo, Kang and Yang, et al. 2017), it was found via the same technique, using tungsten wire and a polymer fiber to bridge the pore, that bubbles would form adjacent to the tungsten wire, but not the polymer fiber, indicating that it was electrical contact, not favorable nucleation topology, that led to preferential evolution sites.

Because the electrolyte exists in the solid phase, there is no need for an aqueous electrolyte, so the A-OER can proceed in both phases, consuming both liquid water and water vapor. Because there have been prior experimental investigations of the vapor-phase reaction (Schuler, Kimura, et al. 2020), the two-phase reaction is a confirmed phenomenon. Each phase has different standard molar Gibbs free energy requirements:

$$\frac{1}{2}H_2O_{(l)} \rightarrow \frac{1}{4}O_{2(g)} + H^+ + e^- \qquad \Delta G^\circ_{rxn} = +118.6\frac{\text{kJ}}{\text{mol } e^-} \tag{1.2}$$

$$\frac{1}{2}H_2O_{(g)} \rightarrow \frac{1}{4}O_{2(g)} + H^+ + e^- \qquad \Delta G^\circ_{rxn} = +114.3\,\frac{\text{kJ}}{\text{mol } e^-} \tag{1.3}$$

From this point forward, all stoichiometric coefficients are defined such that that of the electron is equal to 1, eliminating the need to specify the number of participating electrons in electrochemical equations. As oxygen is produced, charge is transferred simultaneously through the electrolyte and the external circuit. H^+ migrates through the polymer electrolyte membrane, typically a cation-conducting perfluorosulfonic acid membrane such as Nafion®, and electrons travel through an external circuit to the cathode. At the cathode, hydrogen is produced from the reaction of protons and electrons on the negatively polarized surface of another electrocatalyst, which is typically C-supported Pt, in the acidic hydrogen evolution reaction (A-HER):

$$H^+ + e^- \rightarrow \frac{1}{2}H_{2(g)} \qquad \Delta G^\circ_{rxn} = 0.0\,\frac{\text{kJ}}{\text{mol } e^-} \tag{1.4}$$

Due to the highly corrosive conditions at the anode, i.e. high positive overpotentials combined with oxygen and an acidic environment, titanium and precious metals are used for the construction of the cell components at the anode (Carmo, et al. 2013). At the cathode, graphite is an acceptable material because of the lack of oxygen. Graphite and other carbon materials corrode at the anode, expelling carbon dioxide and degrading the conducting materials.

A schematic of a PEMWE system is provided in Figure 1.1. Deionized water is fed to the anode and cathode in a wet/wet operating configuration or, contrarily and rather typically, fed to only the anode in a wet/dry configuration. Liquid water feed is introduced from the water supply, through the cell manifolds, to flow field channels that are machined into the current collector (CC), which electrically contacts the PTL and terminal. The flow field is physically separated by an electrically conducting PTL, which provides pathways

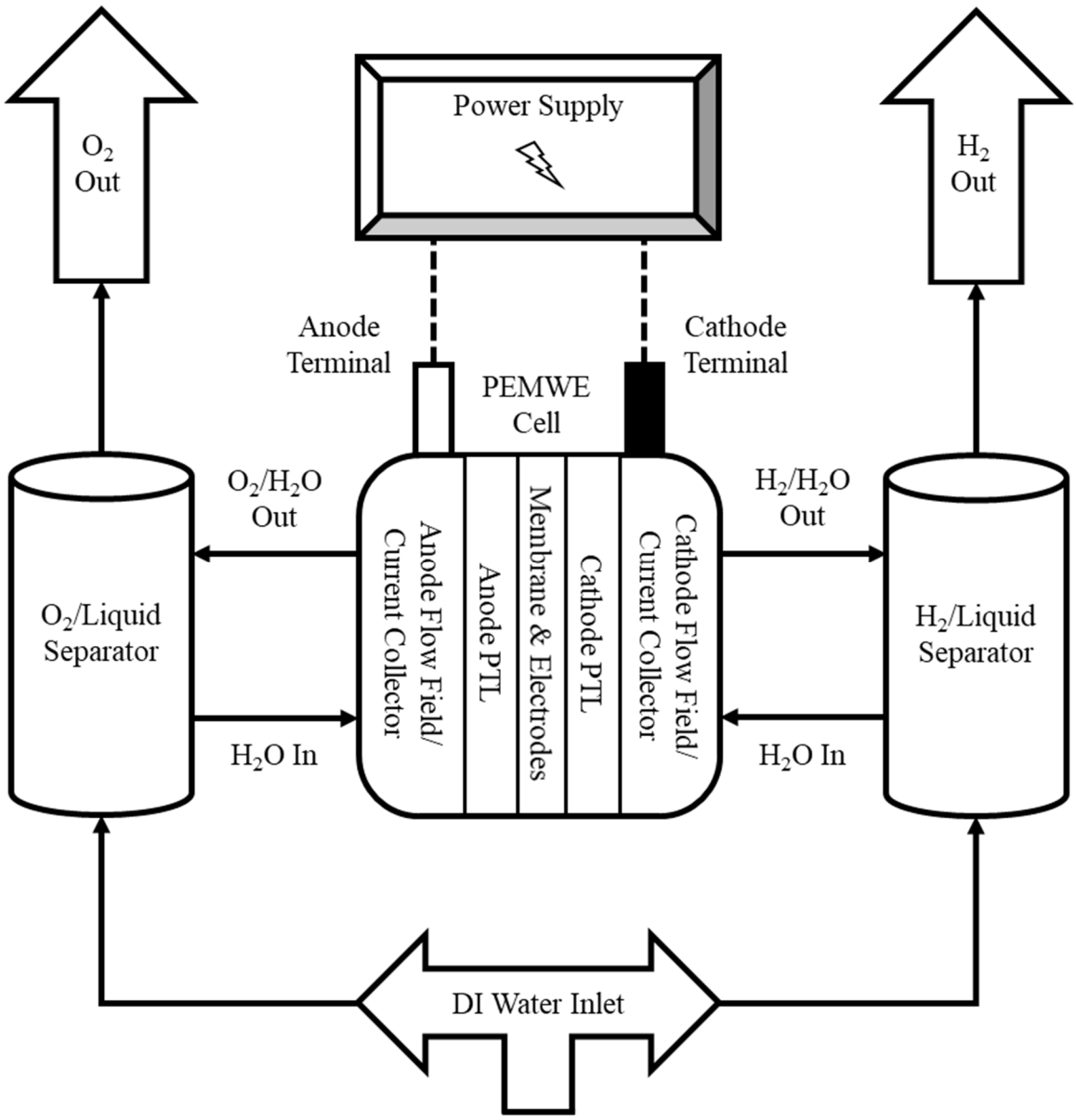

Figure 1.1: Schematic of a proton exchange membrane water electrolysis system.

for incoming liquid water and expelled gas while conducting electrons from the anodic CL to the CC. The PTL functions as a means of transporting electrons and fluid between the CC and CL.

Alkaline Diaphragm Electrolysis.

In ADWE, water is split under alkaline conditions promoted by lye or caustic. ADWE cells have been used for industrial purposes since the 1920s as a means of mass-producing hydrogen prior to the development of steam reforming (Zeng and Zhang 2010). This technology, which predates PEMWE, is therefore widely established and has undergone significant advancement to date. The basic oxygen evolution reaction (B-OER) and basic hydrogen evolution reaction (B-HER) occur via a mechanism different from Equations 1.2-4:

$$OH^-_{(aq)} \rightarrow \frac{1}{4}O_{2(g)} + \frac{1}{2}H_2O_{(l)} + e^- \qquad \Delta G^\circ_{rxn} = +38.7\frac{\text{kJ}}{\text{mol } e^-} \tag{1.5}$$

$$H_2O_{(l)} + e^- \rightarrow \frac{1}{2}H_{2(g)} + OH^- \qquad \Delta G^\circ_{rxn} = +80.0\frac{\text{kJ}}{\text{mol } e^-} \tag{1.6}$$

Figure 1.2 shows a schematic of operation for an ADWE system. A 20-30% KOH solution (Zeng and Zhang 2010, Carmo, et al. 2013) is fed to the anode and cathode in a wet/wet configuration, as the electrolyte is needed at both electrodes to participate in the reaction and to carry charge. The aqueous KOH is fed from a reservoir to the flow field, then distributed among the reaction sites of a porous electrode, which is electrically contacted with the CC. The porous electrode, e.g. a Ni-foam-supported NiFe layered double hydroxide (LDH) at the anode and Ni-foam-supported Raney Ni at the cathode, provides reaction sites at its internal surfaces and allows gas bubbles to escape through the pores. In ADWE devices, the ionic charge carrier is OH^-, which migrates from cathode to anode while electrons travel through the external circuit from anode to cathode.

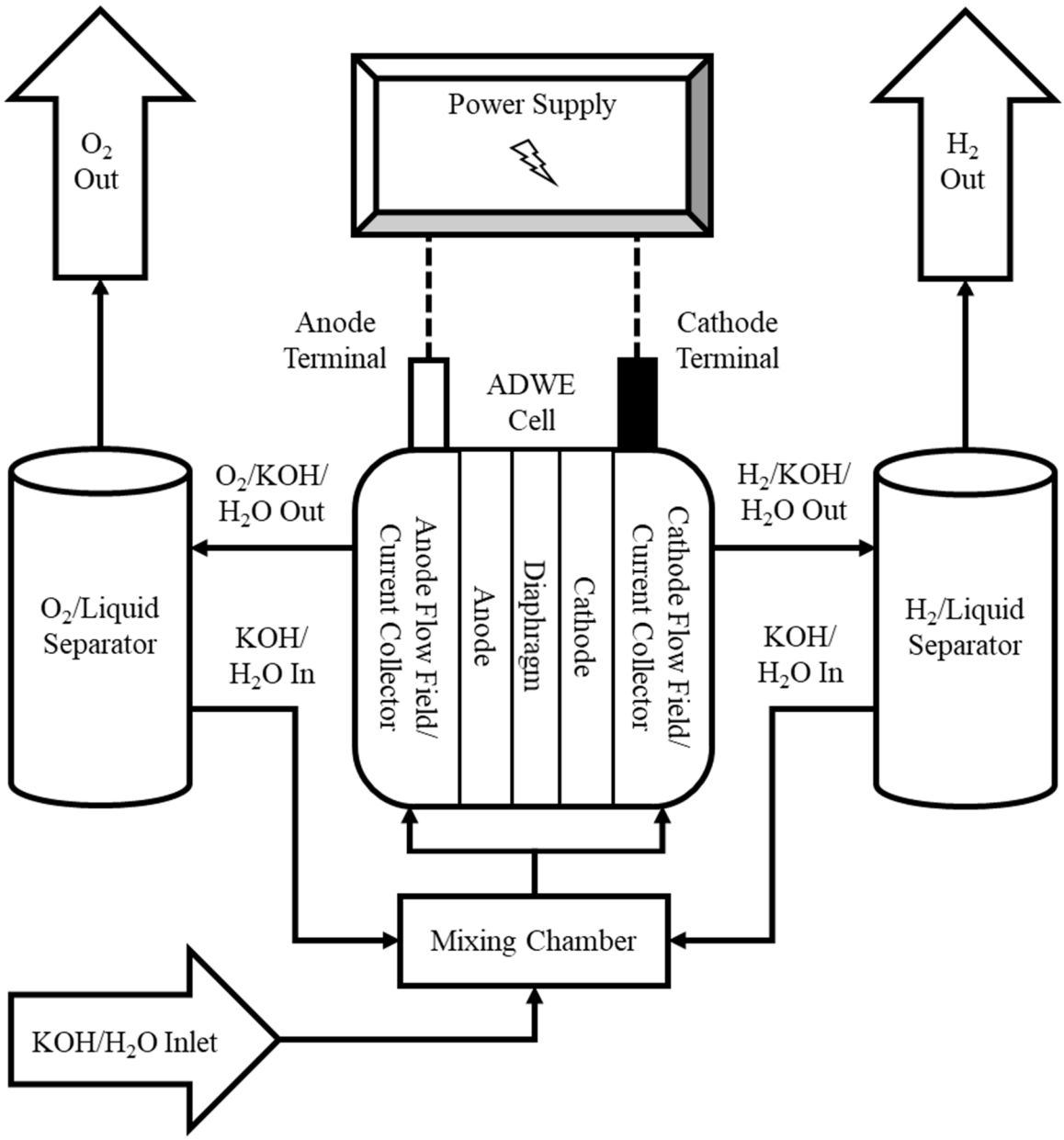

Figure 1.2: Schematic of an alkaline diaphragm water electrolysis system.

The anode and cathode are separated by an insulating porous material, which, unlike Nafion®, is not ion-selective. The state-of-the-art material is ZrO_2 with a polysulfone binder, such as Zirfon®. These separators are porous, allowing ions to migrate through the impregnating solution. Excessive gas crossover is prevented by their hydrophilicity and small pore sizes.

This technology has a few limitations, some leading to the development of PEMWE – its characteristically high ionic resistance, narrow electrical load range, and inability to operate at high differential pressure without dangerous levels of gas crossover, for example. However, the alkaline environment is much more suitable for non-precious metals such as Ni and Fe at the anode, so ADWE cells are much less costly to construct than PEMWE cells (Carmo, et al. 2013). Additionally, recent advances in ADWE cell design, such as the state-of-the-art Zirfon® separator and zero-gap configuration, have ameliorated some of the difficulties, allowing ADWE to remain widespread as PEMWE enters commercialization.

Thermodynamics of Water Electrolysis

The minimum energy per quantity required for an electrochemical reaction to proceed is the equilibrium potential,

$$\phi_{eq} = -\frac{\Delta G^{\circ}_{rxn}}{F} + \int_{T^{\circ}}^{T} \frac{\Delta S_{rxn}}{F}\, dT - \frac{\mathscr{R}T}{F} \ln\left\{ \prod_i a_i^{\nu_i} \right\} \tag{1.7}$$

In Equation 1.7, ΔS_{rxn} is the change in molar entropy from reactants to products, F is Faraday's constant, 96,485.332 C mol^{-1}, $\mathscr{R}$ is the universal gas constant, 8.31446 J mol^{-1} K^{-1}, T is temperature, a_i is the activity of species i, and ν_i is the stoichiometric coefficient of i. The reference state, typically 25 °C and 1 atm absolute pressure, is denoted by the superscripted circle. For temperatures in this application, the integral term in Equation 1.7

can then be approximated as a linear function of the temperature deviation from the reference,

$$\phi_{eq} = \phi_{eq}^{\circ} + \frac{\Delta S_{rxn}^{\circ}}{F}(T - T^{\circ}) - \frac{\mathscr{R}T}{F}\ln\left\{\prod_i a_i^{\nu_i}\right\} \tag{1.8}$$

Energy loss is the conversion of some input energy, in this case electrical energy, to heat as opposed to work. Electrochemical processes are characterized by the magnitudes of energy losses via different mechanisms. These losses, which are reported in units of energy per unit charge (V), can be categorized into three classes: kinetic, resistive, and transport losses. Respectively, these are commonly referred to as the anodic and cathodic activation overpotentials ($\eta_{act,a}$ and $\eta_{act,c}$), resistance overpotential (η_{Ω}), and mass transport overpotential (η_{mt}). In an electrolytic cell, the total cell potential, $|\phi_{cell}|$, must exceed $|\phi_{eq}|$ by an amount equal to $|\eta_{act,a}| + |\eta_{act,c}| + \eta_{\Omega} + \eta_{mt}$ to promote the net transfer of electrons. $\eta_{act,a}$ and $\eta_{act,c}$ determine the reaction rates and thereby the current density. They represent the activation energy required to elevate reactant species to their transition states, and they result in waste heat generation. η_{Ω} is the energy loss associated with charge transport through cell components, primarily the electrolyte, which generates heat also. Charged particles such as electrons and ions must acquire enough energy to jump from one site to another. η_{mt} is the loss associated with the transport of species, which can limit the reaction rate or the effective ionic conductivity and generate waste heat. The focus of this dissertation is to identify factors impacting η_{mt} and present models that aid in understanding the link between mass transport and cell performance.

LeRoy et al. (LeRoy and Bowen 1980) describe the methodology of calculating the equilibrium and thermoneutral potentials of an alkaline water electrolyzer, and in doing so, explain how heat is generated by overpotential and entropic energy dissipation. This is a

very useful paper for learning or refreshing electrochemical thermodynamics. The thermoneutral potential is the potential at which an electrochemical cell neither generates nor consumes heat, which for electrolysis is when the rate of heating due to charge transfer and charge transport losses is equal to the rate of cooling due to the reaction and water evaporation. Neglecting phase change, it can be expressed as

$$\phi_{tn} = -\phi_{eq} + \frac{T\Delta S_{rxn}}{F} \tag{1.9}$$

and the total cell heating, as considered by Ulleberg (Ulleberg 2003) and Hammoudi et al. (Hammoudi, et al. 2012), is equal to the total current times the total energy losses per unit charge, $I(\phi_{cell} - \phi_{tn})$. More conveniently for use at a single electrode, the enthalpy production per area is the sum of the free and entropic energy production,

$$q = \left|\underline{\boldsymbol{i}} \bullet \underline{\boldsymbol{\xi}}\right| \left(\left|\eta_{s,a,c}\right| - \frac{T\Delta S_{rxn}}{F} \right) \tag{1.10}$$

as exemplified by Onda et al. (Onda, et al. 2002) and Ni et al. (Ni, Leung and Leung 2008), who developed one-dimensional (1D) heat transfer models for PEMWE and ADWE, respectively. In Equation 1.10, $\underline{\boldsymbol{i}} \bullet \underline{\boldsymbol{\xi}}$ is the charge flux normal to the electrode boundary, and $\eta_{s,a,c}$ is the surface overpotential of either the anode or cathode. The surface overpotential will be defined as the sum of the activation and mass transport overpotentials,

$$\eta_{s,a,c} = \eta_{act,a,c} + \eta_{mt,a,c} \tag{1.11}$$

Losses Attributed to Porous Media

In both PEMWE and ADWE, porous media properties influence the cell overpotential. In these following sections, phenomena attributed to porous media are placed in the following categories: interfacial resistance between the porous medium and separator, effective conductivity of the electrolyte, and bubble coverage of the electrode

surface. The loss mechanisms differ among the two types of electrolysis cells but are analogous and fall under these categories.

Proton Exchange Electrolysis.

There have been numerous experimental studies that explain the impacts of porous material properties on cell performance. A typical first mention that is cited throughout literature is the work of Grigoriev et al. (Grigoriev, et al. 2009), who developed a fabrication procedure giving precise control over sintered titanium powder plate porosity and pore size, which allowed them to compare performance among PTL properties confidently. The takeaway of their results was that the optimal pore/powder sizes recommended by the authors was around 12/50-75 μm. Mass transport limitations were apparently observed with smaller pore sizes and high contact resistance was observed with larger pore/powder sizes. They demonstrated that mass transport limitations may account for losses of between 50 and 100 mV at above 0.4 A cm^{-2} and that PTL property variations can account for contact resistance losses on the order of 100 mV at or above 1 A cm^{-2}. In the following subsections, the various manners through which porous media may increase the overpotential, particularly at the anode, are elaborated.

Electronic Resistance in the Catalyst Layer.

It is important to mind that the results of Grigoriev et al. (Grigoriev, et al. 2009) summarized in the section introduction are not universal. The catalyst they selected was iridium black, and its mass loading was 2.0 mg Ir cm^{-2}, so this study used a highly conductive CL. If the more durable IrO_2 is substituted for iridium black and the catalyst mass loading is reduced, this reduces the CL conductivity and thereby increases interfacial resistance. A similar study conducted with titanium fiber PTLs and a slightly less

conductive IrO_2/Pt anode CL found that performance improved with decreasing mean pore diameter, with the smallest pore size being 12.7 μm (Ito, et al. 2013). The authors attributed this to low cell resistance when using smaller pore sizes and increased mass transport limitations with large pore sizes. According to the authors' speculations, higher cell resistance was observed using a PTL with large pore sizes because the larger bubbles formed from these pores in the flow field channels resisted the flow of liquid water to the anode more so than smaller bubbles. Reduced water content would lead to membrane dehydration, which directly impacts the cell resistance. This explanation was formed in part by a substantial resistance increase with increasing current density, with larger bubbles being formed at higher gas generation rates.

In light of earlier experimental work, including that from Mo et al. (Mo, Kang and Retterer, et al. 2016, Mo, Kang and Yang, et al. 2017) already described in the "Operating Principles" section, the actual cause of heightened resistance in large-pore materials may have been within the CL. Kang et al. (Kang, Mo, et al. 2017b) conducted an experimental and numerical investigation of thin, perforated PTL materials in a PEMWE device. The properties of these materials, namely the porosity and pore size, could be very accurately and precisely tuned, allowing the authors to examine the effects of one variable. Their model considered in-plane CL resistance within the pores by subdividing the pore opening region into a number of small tori and using a transmission line model to calculate the overall resistance, with each torus being an element of the transmission line. Additionally, a 1D two-phase transport model was applied to determine the gas concentrations and thereby the diffusion overpotential. By modeling the current distribution within the pores, the simulations fit experimental data very well. They showed that increased porosity and

decreased pore size led to the best performance because it reduced the in-plane resistance contribution. These findings were applied in practice in later works (Kang, Yang, et al. 2018, Kang, Yu, et al. 2019) when micro- and nano-porous layers were deposited onto the thin PTLs in order to improve the electrical contact between the anodic CL and PTL. It was evident that the in-plane CL resistance was the greatest contributor to overall resistance and low catalyst utilization.

Schuler et al. (Schuler, De Bruycker, et al. 2019, Schuler, Schmidt and Büchi 2019) extensively analyzed the link between PTL structure and electrolysis performance, providing a better understanding of mass transport overpotentials. By calculating the residual overpotentials, they quantified mass transport overpotentials with magnitudes reaching relatively high levels of approximately 200 mV. These values were used to compare the six fibrous PTL materials used at the anode; three with relatively low porosity and three with relatively high porosity, each group with materials of varying pore size. The PTLs were characterized in part by normalized surface parameters describing the topology of the surface, considering that upon compression and humidification of the membrane, that it would swell into pore openings, influencing the contact area. They found that decreased contact area and cumulative triple-phase line lengths led to lower catalyst utilization, while increased non-contact area had the same impact. Finally, they proposed three processes that could limit catalyst utilization: fluid transport in the PTL and CL, ion transport in the CL ionomer network, and electron transport through the catalyst particles. The authors reasoned that electron transport is the most prominent mechanism limiting catalyst utilization and supported their conclusion with SEM images showing that the in-plane conductivity of the CL can be significantly reduced by mechanical-stress-induced

cracking. Furthermore, they speculate, noting lack of proof, that other proposed voltage loss mechanisms such as reduced ionomer conductivity and bubble coverage are unlikely to result in limited catalyst utilization. The following subsections describe these other mechanisms.

Effect of Mass Transport Limitations on Ionic Conductivity.

The solid electrolyte phase of the CL is often Nafion®, whose conductivity is a function of its water content. It is common to use the model presented by Springer et al. (Springer, Zawadzinski and Gottesfeld 1991), which defines an activation energy for proton conduction. It is important to note that the study focuses on the water activity dependence of ionic conductivity and that the activation energy was determined from data at two temperatures, 30 and 80 °C. More recently, a correlation between Nafion® 117 membrane conductivity, temperature, and relative humidity was developed using an expanded experimental dataset and a four-point probe method (Yadav and Fedkiw 2012). The latter model uses an activation energy dependent on relative humidity, and has reasonable accuracy.

Some ionomer is in contact with the liquid phase, and some with the gas phase. The ionomer adjacent to the vapor phase possesses a water content proportional to the activity of water vapor, leading to low proton conductivity when water vapor is undersaturated. This leads to an increased η_{Ω} at constant current.

Revisiting the work of Ito et al. (Ito, et al. 2013), mass transport overpotential was quantified via subtracting the thermodynamic, kinetic, and resistive components of cell potential from the total and comparing the residual overpotential among materials. The authors observed a 40 mV rise in mass transport overpotential with increasing current

density due to higher gas coverage. Comparing their set of PTL materials, they found that the PTLs with the largest pores exhibited the highest mass transport limitations. They reasoned that because bubble evolution size is directly proportional to pore size, larger pores caused bubbles to further impede liquid water flow through the flow field channels. In turn, this would have led to high void fractions at the electrode. One possible result of high void fraction is a reduction in the conductivity of the membrane and the CL ionomer. The authors cited reduced ionomer conductivity as the explanation for the more pronounced increase in cell resistance and mass transport overpotential when using a PTL with a large pore size. Note that this explanation is plausible but does not consider CL delamination or other possible causes discovered more recently, such as membrane swelling and CL compression (Babic, Schmidt and Gubler 2018), and CL fracturing (Schuler, Schmidt and Büchi 2019).

Babic et al. (Babic, Schmidt and Gubler 2018) suggested another reasoning for the relationship between pore size and resistance. In their experimental study, they measured the CL ionomer resistance using potentiostatic electrochemical impedance spectroscopy (EIS) experiments under nitrogenated water and hydrogen flow to the working and counter electrodes. Using a transmission line model, they discovered that the CL ionomer resistance increased with increasing pore size, notably to a greater degree than the resistance increase reported by Ito et al. (Ito, et al. 2013) Their work strongly suggested that increased resistance was due to more non-uniform CL compression with larger PTL pores, as more compression reduces porosity and promotes better contact in the ionomer network. It is important to add that the in-situ experimental results may not describe the

actual ionic resistance of the CL under cell operation at high current densities, which may induce drying and higher resistances.

Schuler et al. (Schuler, Schmidt and Büchi 2019) state that it is possible for ionomer drying to occur at high current densities, which would cause reduced catalyst utilization in the vicinity of the dry ionomer due to the increased resistance. The authors did not expect the increase in resistance to be this consequential, but the extent of drying, hence the increase in resistance, depends on the ease of mass transport. It is known from PEMWE segmented cell studies that when the liquid water feed rate is reduced to near its lower limit, the local high-frequency resistance (HFR) increases, first near the flow field outlet, then upstream. Immerz et al. (C. Immerz, et al. 2018, C. Immerz, et al. 2019) demonstrated the phenomenon of membrane and CL ionomer dehydration with a 50 cm segmented PEMWE cell using EIS procedures at each pair of CCs. When the stoichiometric feed rate was reduced to below 5, they noticed the HFR increase at the end of the channel when current density exceeded 0.5 A cm^{-2}, accompanied by an increase in the cell potential under constant current. Furthermore, their Nyquist plots indicate an increase in the impedance attributed to mass transport, possibly indicating that diffusion was rate-limiting.

Mass transport can limit catalyst utilization by dehydrating not only the ionomer, but the catalyst itself. This concept is explained in more detail in the following subsection.

Kinetic Limitations Due to the Gas Phase.

In PEMWE anodes, the reactant water exists in the liquid and vapor phases within the CL, which is a conglomerate of the typically precious electrocatalytic material, solid ionomer electrolyte, and sometimes a catalyst support, e.g. platinum (Choi, Bessarabov and Datta 2004) or high loads of an inexpensive and low-conductivity material such as

TiO_2 (Mazúr, et al. 2012) to enhance overall conductivity. During the A-OER, aqueous oxygen is produced and it nucleates to form a gas phase under supersaturation. Vogt (Vogt 1990) proposed this to be the case and used this as the basis of an experimentally validated concentration overpotential model for aqueous electrolysis. This idea has been applied to PEMWE as well. Nouri-Khorasani et al. (Nouri-Khorasani, et al. 2017) modeled bubble nucleation using classical nucleation theory in order to calculate the nucleation time, which was used along with growth times to estimate bubble coverage in a PEMWE model. The growth of the gas phase is accompanied by interfacial mass transport in the form of evaporation, which humidifies the gas phase. Water vapor then diffuses through the gas phase toward the catalyst surface, where it too reacts to form more oxygen. This detail is a well-established and important concept. The gas-phase A-OER (A-OER(G)) has been studied to extract kinetic parameters for IrO_2 from in-situ experiments, including the rate exponent that accounts for the kinetic impact of relative humidity (Schuler, Kimura, et al. 2020). They utilized a vapor-fed PEMWE cell in order to vary the water activity. To do this, they determined the range of current densities that resulted in minimal mass transport limitations with which to conduct Tafel analyses for the transfer coefficient and exchange current density as functions of temperature. Varying the water activity allowed them to determine a semi-empirical rate order for the calculation of gas-phase current density. In the liquid phase, it is safe to assume that the activity of water is unity, so that $\eta_{mt} = 0$. In the gas phase, the partial pressure of water vapor, and thus its activity, can vary. An activity less than 1 leads to a mass transport loss. The magnitude of its effect on cell performance depends on the phase composition, which is commonly quantified by the volume fraction of the liquid phase, also known as liquid saturation. Liquid saturation is related to the

fraction of the total catalyst area that is in contact with the liquid phase. Low liquid saturation combined with low water vapor activity leads to reduced electrochemical active area, which increases the $\eta_{s,a}$ requirement to maintain a desired current density. This discussion is illustrated in Figure 1.3. In Figure 1.3a, the equilibrium potentials of the liquid-phase A-OER (A-OER(L)) and A-OER(G) are plotted versus relative humidity in the range at which the values intersect in the temperatures of interest, essentially the points where the two reactions are thermodynamically favored equally. This occurs at a relative humidity between 0.05 and 0.44, with the A-OER(G) being more thermodynamically favorable at lower relative humidity as temperature is reduced. Figure 1.3b, which plots the kinetic favorability of the A-OER(G):

$$f_{kin,G} = h_r^{2.07-\alpha/2} \tag{1.12}$$

shows that the A-OER(G) is never kinetically favored, as was just mentioned. However, when thermodynamic and kinetic factors are combined as in Figure 1.3c, which plots the overall favorability of the A-OER(G),

$$f_{tk,G} = h_r^{2.07-\alpha/2} \exp\left\{\frac{\alpha F\left(\phi_{eq,L} - \phi_{eq,G}\right)}{RT}\right\} \tag{1.13}$$

one finds that overall, the A-OER(G) can be more favorable than the A-OER(L) at a sufficiently high relative humidity.

Therefore, it is important to understand evaporation and what influences its rate. Evaporation rates have been studied for fuel cell applications in ex-situ experiments. Utilizing X-ray computed tomography, Zenyuk et al. (Zenyuk, et al. 2016) observed a decrease in the overall area of a liquid/gas front with decreased liquid saturation of the GDL, but if a specific area is calculated on the basis of the liquid volume, this quantity

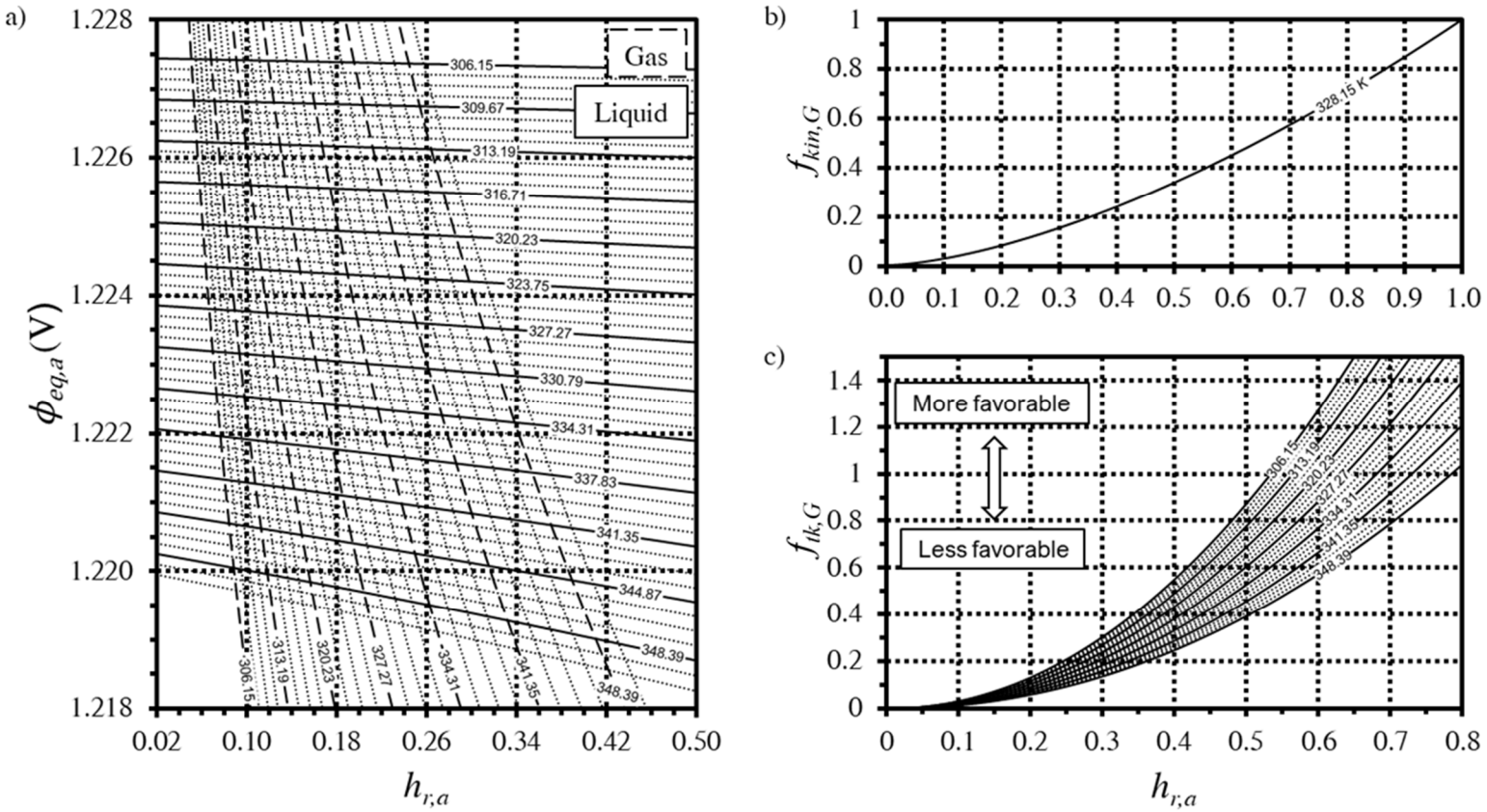

Figure 1.3: Thermodynamic and kinetic favorability of the gas-phase acidic oxygen evolution reaction. a) Anodic equilibrium reduction potentials for the liquid- and gas-phase reactions at different relative humidities and temperatures, particularly at which the thermodynamic favorability (low potential = high favorability) is similar. b) Relative kinetic favorability of the A-OER(G) at different relative humidities and temperatures. The insert shows the function across the full range of relative humidities at one temperature because the temperature sensitivity was miniscule. c) Relative overall favorability of the A-OER(G) at different relative humidities and temperatures, in which values above 1 indicate that the A-OER(G) is the preferred reaction (Lopata, Weidner, et al. 2022).

increased with decreasing liquid saturation. The evaporation rate was measured and was found to be highest at lower liquid saturations. When the liquid saturation decreases, the characteristic length scale of the liquid/gas interface shrinks, so the specific interfacial area increases. Since then, other authors have conducted similar trials (Mularczyk, et al. 2021, Lal, et al. 2018). Note that because the application of these studies was the fuel cell GDL, the nature of the interface was different from what is expected in PEMWE. Electrolysis PTLs are quite hydrophilic and because gas is evolved, gas moves via convection through the PTL from the anode to the channel through preferential pathways (Satjaritanun, et al. 2020, Lee, et al. 2019, Arbabi, et al. 2016), which might affect the interfacial area. However, the use of similar methods to capture the liquid/gas interface surrounding evolving bubbles would be more challenging, if not impossible, because of the shorter time scale of this process compared to the length of a CT scan. Furthermore, titanium PTLs tend to strongly attenuate X-rays and reduce the signal-to-noise ratio (Lopata, Weidner, et al. 2022).

Experimental EIS studies have shown that impedance associated with mass transport processes is measurable, implying that mass transport may contribute to reduced catalyst utilization. Dedigama et al. (Dedigama, et al. 2014) observed evidence of a mass transport limitation in Nyquist plots, which was dependent on the cell potential and liquid water feed rate. They noticed the mass transport impedance artifact emerge upon increasing voltage and then disappear upon further increasing it. Based on their results, they concluded that the transport limitation was caused by bubble formation and that a change in flow regime from bubbly to slug flow eliminated the limitation. Babic et al. (Babic, Schmidt and Gubler 2018) reported Nyquist plots that show increased mass transport impedance when

using a PTL with larger pores and particles, indicating that PTL properties may significantly affect mass transport to a degree that it becomes limiting, at least locally.

The model of Kang et al. (Kang, Mo, et al. 2017a) neglects any reaction that may occur where the CL is compressed by the thin-plate PTL, but agrees well with experiments. This suggests that it is extremely difficult for in-plane transport to occur between these regions and the pore, so much so that modeling it was not necessary when using these materials. Kang et al. (Kang, Yu, et al. 2019) presented Nyquist data for cells containing composite PTLs with thin perforated plates in contact with the CL, and they show mass transport impedance artifacts. These are not visible in Kang et al. (Kang, Yang, et al. 2018), but in that earlier work, the current density was fairly low, at 0.2 A cm^{-2}, so catalyst utilization was likely limited by electron transport only. This concept of evolved gas dominating the spaces in between the solid phase of porous conductors and the separator is not new, as will be explained in the later discussion of porous media effects on ADWE performance. It is a likely explanation for the increased mass transport overpotential with larger pore sizes observed by Ito et al. (Ito, et al. 2013), as described previously. Not only did the pore sizes differ among their PTLs, but so did the fiber diameter. Large pores were accompanied by large fibers; these fibers were pressed into the CL, and this may have prevented gas from escaping to a large extent in those compressed locations.

It can be argued based on this literature analysis that two-phase transport, ionomer dehumidification, and electron transport are all significant mechanisms limiting catalyst utilization, but their effects are localized on length scales consistent with the PTL pore and particle sizes, and the behavior of a CL is heterogeneous.

Alkaline Diaphragm Electrolysis.

Reduction of Effective Ionic Conductivity by Bubbles.

Conventionally, ADWE devices consisted of two solid plate electrodes immersed in a stagnant or flowing solution with a porous separator preventing gases from mixing. This design inherently had high resistance because a gap was needed between the electrodes and separator to allow gases to escape. When there are many bubbles in the electrolyte, they impede the migration of ions by forcing them to travel tortuous and bottlenecked paths, thereby decreasing the effective ionic conductivity of the cell. Mat and Aldas (Mat, Aldas and Ilegbusi 2004) modeled this effect in a vertical-channel aqueous electrolyzer with large gaps between the electrodes and separator. They included relationships describing the effect of void fraction on the effective electrolyte conductivity, effective ion diffusivity, and electrode bubble coverage. Their model estimated a current distribution along the length of the channel and was validated by comparing their void fraction distributions with experimental observations of Reigel et al. (Reigel, Mitrovic and Stephan 1998)

Narrower gaps generally lead to lower resistance because ions must travel shorter distances, but this could make it harder for gas to leave the cell. Nagai et al. (Nagai, et al. 2003) noted the existence of an optimal gap width in a stagnant reservoir cell containing 10 wt% KOH solution with solid plate electrodes and a separator. The optimal distance between electrodes increased with an increase in current density due to a greater presence of gas bubbles. At current densities slightly less than 1 A cm^{-2}, the optimal gap between the electrodes and separator was found to be about 1 mm. Using forced convection with a solution inlet at the bottom of the anode and cathode reservoirs, the optimal gap width can

be reduced because forced convection and buoyancy act in conjunction to drive the flow of bubbles toward the outlet. Forced convection also helps bubbles to detach from the electrodes with smaller sizes, limiting the bubble coverage. Hine et al. (Hine, et al. 1975) demonstrated the effect of gap width and convection on the effective conductivity of an electrolyte solution. They measured the potential across the cathodic electrolyte, or catholyte, using a current interruption procedure in a vertical-channel electrolysis cell operated with various catholyte gap widths and feed rates of dilute NaOH solution to the cathode. The authors observed a decrease in the resistance overpotential with respect to gap width, but also an increase in the resistivity relative to the bubble-free solution. The relative resistivity increased with more gas phase present and decreased with higher catholyte feed rates. An empirical relationship was presented for the relative resistivity as a function of void fraction, the gap width, the gas:liquid velocity ratio, and parameters dependent on the channel geometry.

Provided that the diaphragm is capable of suppressing gas crossover, gap widths can be safely reduced from their conventional sizes without too great a risk of forming explosive gas mixtures. Improvements in electrode design allowed the optimal gap width to be further reduced while still allowing evolved gases to escape the gap. Perforated plate electrodes were the first step in developing what is now known as a zero-gap cell, any cell with less than 1 mm of space between the electrode and separator (Ursúa, Gandía and Sanchis 2012). The use of perforated plates further reduces the necessary gap width because they allow bubbles to escape through the holes shortly after formation rather than traveling along the narrow electrolyte gap. Kienzlen et al. (Kienzlen, Haaf and Schnurnberger 1994) visualized the gas evolution from perforated plate electrodes, proving

that bubbles form between the electrode and separator and are expelled through the pores of the electrode. The authors went on to suggest that the electrolyte gap should be on the same order of magnitude as the pore diameter, however there was little experimental evidence bolstering this. They did notice that pores with a diameter of 60 μm did not allow bubbles to pass, which allowed them to suggest a minimum pore size of about 200 μm. Their work was motivated by a disagreement in literature concerning the two-phase transport mechanism in such a cell, namely that between Hofmann (Hofmann 1980) and Dinkelacker (Dinkelacker 1989). Hofmann postulated that gas is generated on the backside of the electrode, away from the separator, and ions migrate through the pores of electrodes. Dinkelacker proposed an opposing mechanism in which gas bubbles are generated between the electrode and separator and ions migrate between solid electrode surfaces. While Kienzlen et al. (Kienzlen, Haaf and Schnurnberger 1994) use their visualization results to confirm the Dinkelacker mechanism for their electrode, the Hofmann mechanism does hold merit, which will be explained later.

Ultrasound has been investigated as a means of reducing bubble detachment size by adding mechanical energy to the electrode surface and disturbing the liquid/gas interface. Hung et al. (Hung, et al. 2012) demonstrated how ultrasound reduces the cell voltage in this way, but it is important to note that implementing ultrasound in a system requires care to avoid using too much energy to generate an ultrasonic field. In their investigation, they use a 50 W ultrasound source on a cell operating at up to 3 W, but larger cells and smaller sources may make this method economical. Despite these innovations, conventional ADWE devices still have very high resistance compared to PEMWE cells due to the electrolyte gap.

The use of metal foams as supports for porous catalytic electrodes led to the true zero-gap cell, in which the electrodes are in physical contact with the separator. These electrodes facilitate the reaction throughout the thickness of the electrode and have higher surface areas than solid or perforated plates. If the length scale of the matrix phase, i.e. the thickness of the foam structure, is sufficiently small, it should prevent the accumulation of gas near the separator and resultant mass transport limitations to cell performance. However, despite no electrolyte gap existing between the electrodes and diaphragm, the resistance of the true zero-gap cell was still found to be higher than what is predicted based on the known properties of Zirfon® and the KOH electrolyte. Rodríguez et al. (Rodríguez, et al. 2019) measured the area-specific resistance and calculated the tortuosity of the Zirfon Perl UTP 500® separator in 30 wt% KOH solution. They compared three measurement procedures and found the zero-gap EIS to be the most accurate and precise, giving a resistance of 0.2935 Ω cm^2 at room temperature for a fresh sample. The authors made clear that their potentiostatic EIS procedure used a 10-mA-amplitude oscillating input voltage about the open circuit potential to prevent gas formation. One interesting aim of the study besides identifying the best measurement procedure was to compare the resistances of new and aged diaphragms. After galvanostatic aging at 200-400 mA cm^{-2} and 60 °C for 130 h, the area-specific resistance increased by about 50% of the starting value, corresponding to an increase in tortuosity from 1.89 to 2.84. They did not seem to consider any change in diaphragm porosity because a porosity measurement procedure is not given, but care was taken in achieving good contact between the electrodes and separator without compressing the separator. The results presented by the authors provide a means of estimating theoretical resistances and comparing them to experimental values. Others have

acknowledged the interfacial resistance in ADWE cells, most notable for the scope of this work being de Groot and Vreman (de Groot and Vreman 2021), who developed a two-dimensional (2D) model of the electrode/separator interface (ESI). Their model offers a quantitative theoretical basis for the resistance contribution associated with the ESI, which convincingly proposes that while gas bubbles form between the electrode and separator, ions primarily travel through pore space because bubbles in the gaps impede ion transport. Therefore, the mechanisms suggested by Hofmann (Hofmann 1980) and Dinkelacker (Dinkelacker 1989) are both correct, but to varying degrees depending on electrode properties and operating conditions.

Kinetic Limitations Via Bubble Coverage.

The electrolyte in ADWE is in the aqueous phase, so if there is any water vapor consumption at all, perhaps at an interface between the catalyst and solution, the reaction should be so biased toward the liquid phase that the gas phase reaction can be considered negligible. Most, if not all, ADWE models that consider bubble coverage apply this assumption (Mat, Aldas and Ilegbusi 2004, Hammoudi, et al. 2012, Henao, et al. 2014, Abdin, Webb and Gray 2017), though it is not always explicit. Perhaps the imaginable reaction of water vapor in ADWE devices simply has not been explored, but the exclusion of the gas-phase B-OER and B-HER can be rationalized. Envision a growing bubble attached to the surface of an electrode. The bubble grows because it is fed by hydrogen or oxygen that is supersaturated in the surrounding solution near the electrode surface (Eigeldinger and Vogt 2000, Balzer and Vogt 2003, Vogt and Balzer 2005, Kadyk, Bruce and Eikerling 2016). Ions participate in the reaction at the electrode surface, but if a bubble is in contact with or very close to the surface, the ionic resistance between the bulk of the

solution and the would-be reaction site becomes extremely high compared to elsewhere, preventing any significant reaction in that location. Thus, this process can be thought of as a small-length-scale electrolyte resistance that presents itself in the macroscale as an apparent kinetic limitation. This differs from PEMWE because the solid electrolyte may still contain water when in contact with a humid gas phase, thereby having a non-zero ionic conductivity. In ADWE, regardless of relative humidity, bubbles obstruct the path of ion migration. Ions are much less likely forced to migrate around dry ionomer regions in PEMWE than around bubbles in ADWE. Therefore, only the liquid-phase reactions are considered in Equations 1.5 and 1.6. Despite this, humidity in the gas phase may still affect the equilibrium potential by reducing the partial pressure of hydrogen or oxygen gases. Figure 1.4 plots the overall equilibrium potential of the cell versus relative humidity. A maximum of 0.62 is set due to the limited activity of the water in the concentrated solution. The sensitivity of the equilibrium potential to relative humidity in ADWE is miniscule compared to that in PEMWE. Under the assumption of no gas-phase current contribution, during the B-OER and B-HER, gases reduce the electroactive area by an amount equal to the bubble coverage area. This effectively decreases the magnitudes of $\eta_{act,a}$ and $\eta_{act,c}$. Note that in PEMWE, the cathodic electroactive area is unaffected by the gas phase because water does not participate in the A-HER.

Safety Considerations Pertaining to Gas Crossover.

In light of eliminating the gap width through electrode design, it is necessary to highlight improvements in the porous diaphragms, which must be strong inhibitors to gas crossover. Gas crossover can be hazardous at low operating current density or in the event of pump failure or advanced degradation of the separator. Industrial ADWE cells operated

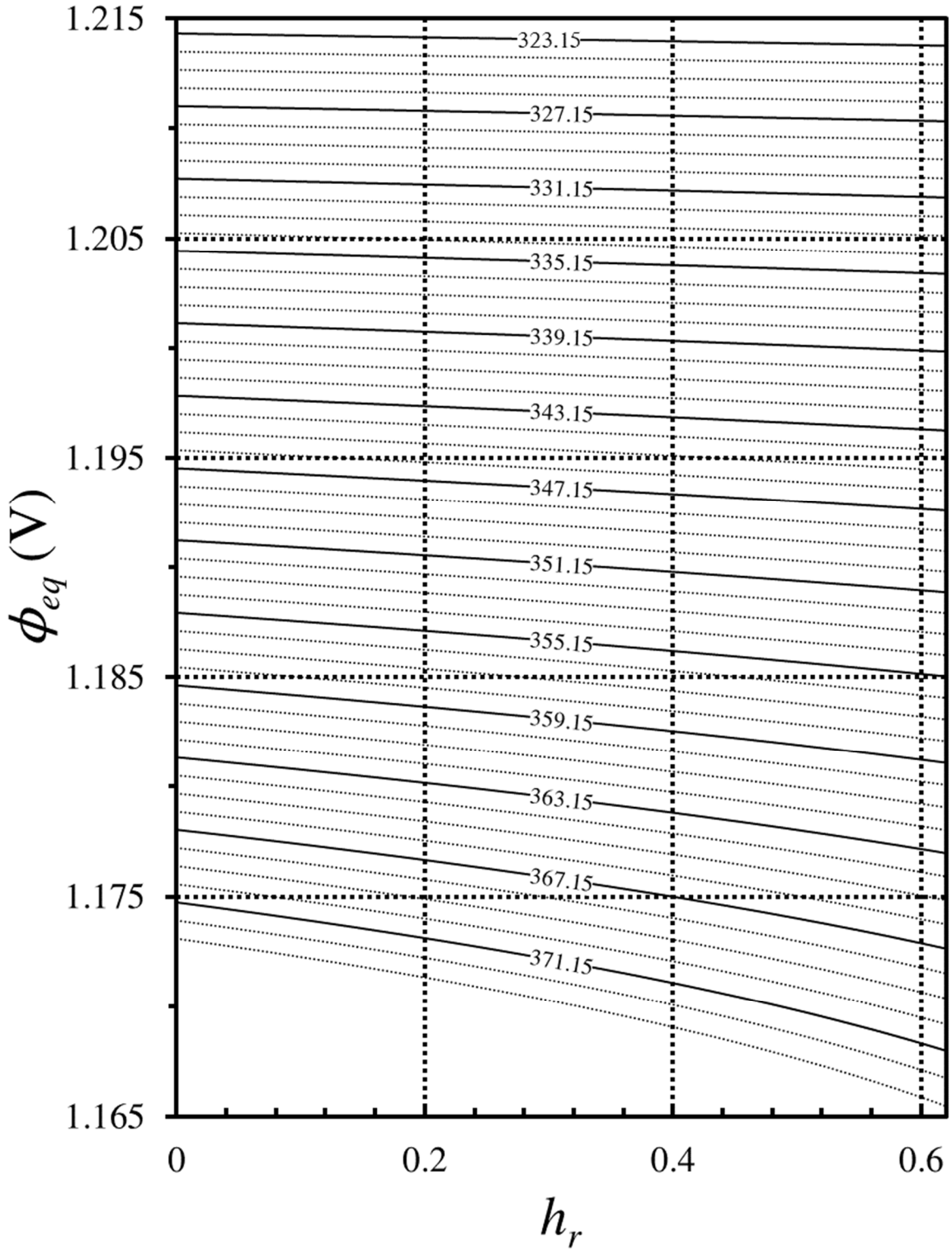

Figure 1.4: Overall equilibrium reduction potential of the basic oxygen and hydrogen evolution reactions at various temperatures versus relative humidity. Temperature labels are in K. A water activity of 0.62 was used for this calculation, so this is used as the cutoff value for the relative humidity.

in the early 20th century used asbestos separators that were highly effective at limiting gas crossover due to their hydrophilicity. Unfortunately, asbestos is very harmful to human health and must be avoided. Upon discontinuing the use of asbestos, immediate porous polymer replacements did not possess the desired hydrophilicity to discourage gas mixing. To enhance wettability, hydrophilic powders were added to the polymers to form functional composites (Brauns, et al. 2021). A well-known substitute for asbestos diaphragms is Zirfon®, which is a porous composite of ZrO_2 and polysulfone. The hydrophilicity and high bubble point of oxide-impregnated materials prevents severe gas mixing even when a porous electrode is pressed against the separator. More studies have been conducted to reduce or mitigate gas crossover to further advance ADWE technology. To obtain insight about the mechanisms of gas crossover, the reader is directed to refer to Schalenbach et al. (Schalenbach, Lueke and Stolten 2016), who developed useful empirical relationships for hydrogen diffusivity and solubility as functions of temperature at various KOH concentrations. They describe three crossover mechanisms: the diffusion of dissolved gases through solution within the diaphragm, the convective transport of solution while carrying dissolved gases, and the bubbling of gases through the diaphragm pores. Trinke et al. (Trinke, et al. 2018) add that supersaturation of gases in solution may play a role. They compare the mechanisms and severity of crossover among PEMWE and ADWE and discuss several ways to prevent or mitigate gas crossover. Recent diaphragm fabrication studies have yielded higher bubble point pressures, which inhibit gas permeation crossover and allow greater flexibility for operating conditions involving pressure differentials across the diaphragm (Lee, Mehdi, et al. 2020b, Lee, Dung, et al. 2020a).

Computational Fluid Dynamics Principles

In the following sections, the governing equations used in the presented models are provided, and then brief overviews of computational methods used to obtain flow solutions are given.

Governing Equations.

The goal of any numerical solver for CFD is to iteratively approach a solution that satisfies equations of the form

$$\frac{\partial \varphi}{\partial t} = \nabla \bullet \underline{\boldsymbol{\Phi}} + \mathcal{S} \tag{1.14}$$

in which φ is a generalized concentration, $\underline{\boldsymbol{\Phi}}$ is a generalized flux, and $\mathcal{S}$ is a volumetric source of the entity of interest. At steady state, which is the scope of this work,

$$\nabla \bullet \underline{\boldsymbol{\Phi}} + \mathcal{S} = 0. \tag{1.15}$$

The solutions presented later apply the steady-state conservation of mass, momentum, neutral species, charged species, energy, and charge, which are presented once in order below:

$$\nabla \bullet \left(\varepsilon \overline{\rho} \hat{\underline{\boldsymbol{v}}}\right) = \sum\nolimits_i \mathcal{S}_i \tag{1.16}$$

$$\nabla \bullet \left(\varepsilon^2 \overline{\rho} \hat{\underline{\boldsymbol{v}}} \otimes \hat{\underline{\boldsymbol{v}}}\right) = -\nabla P \bullet \underline{\underline{\boldsymbol{I}}} + \nabla \bullet \underline{\underline{\boldsymbol{T}}} - \underline{\underline{\boldsymbol{R}}} \bullet (\varepsilon \hat{\underline{\boldsymbol{v}}}) + \underline{\boldsymbol{f}} + \varepsilon \hat{\underline{\boldsymbol{v}}} \sum\nolimits_i \mathcal{S}_i \tag{1.17}$$

$$\nabla \bullet \left(w_{S,i} \rho_i \hat{\underline{\boldsymbol{v}}}\right) = -\nabla \bullet \underline{\boldsymbol{n}}_i + \mathcal{S}_i \tag{1.18}$$

$$\nabla \bullet \left(\boldsymbol{C}_{S,i} \check{\underline{\boldsymbol{v}}}\right) = -\nabla \bullet \underline{\boldsymbol{N}}_i + \mathcal{S}_i / \boldsymbol{M}_i \tag{1.19}$$

$$\nabla \bullet \left(\varepsilon \overline{\rho} h \hat{\underline{\boldsymbol{v}}}\right) = -\nabla \bullet \underline{\boldsymbol{q}} + \nabla \bullet \left[\underline{\underline{\boldsymbol{T}}} \bullet \left(\varepsilon \hat{\underline{\boldsymbol{v}}}\right)\right] + \mathcal{S}_\Delta \tag{1.20}$$

$$\nabla \bullet \underline{\boldsymbol{i}} = j \tag{1.21}$$

The concentrations expressed above are the density ρ, superficial mass fraction $w_{S,i}$, and superficial molar concentration $\boldsymbol{C}_{S,i}$. The material properties ε, $\boldsymbol{M}_i$ and h are the continuum

porosity, molecular weight, and specific enthalpy of the fluid, respectively. The various fluxes are bold with underscores and consist of the volume flux $\underline{\boldsymbol{v}}$, mass flux $\underline{\boldsymbol{n}}_i$, molar flux $\underline{\boldsymbol{N}}_i$, heat flux $\underline{\boldsymbol{q}}$, and charge flux $\underline{\boldsymbol{i}}$. Tensor quantities are also bold and given two underscores, and they include the identity matrix $\underline{\underline{\boldsymbol{I}}}$, the viscous force tensor $\underline{\underline{\boldsymbol{T}}}$, and the porous viscous resistance tensor $\underline{\underline{\boldsymbol{R}}}$. The vector $\underline{\boldsymbol{f}}$ represents the body force vector. Mass-, mole-, and volume-weighted average properties are accented with hats, overbars, and breves, respectively.

Though the wording of the classical conservation laws state that matter and energy cannot be created or destroyed, source terms are provided for mass, momentum, energy, and charge equations. This is in absence of the assumption that a particular region of interest is a closed system. A region can contain multiple phases, only one of which may be of interest, so when matter or energy passes from one phase to another, there is an apparent source or sink. The source terms $\mathcal{S}_i$, $\mathcal{S}_\Delta$, and j denote the component mass source, heat source, and transfer current density, respectively.

Finite Volume Method.

The finite volume method (FVM) discretizes a continuous domain into a finite set of control volumes, or cells, bound by faces in a process also known as “meshing.” Convex cells with high quality, or small aspect ratios, are preferred, because they reduce the magnitudes of numerical corrections necessary to compute fluxes normal to the faces of the cell. Intensive properties and volumetric terms are evaluated at the centroids of cells while fluxes are evaluated at their faces. This strategy requires the transformation of the governing equations by integrating over the volume V and applying Gauss’s Divergence Theorem to obtain a convenient form containing an integral over the control volume

surface area $\underline{\boldsymbol{A}}$,

$$\nabla \bullet \underline{\boldsymbol{\Phi}} + \mathcal{S} = 0 \rightarrow \int \underline{\boldsymbol{\Phi}} \bullet d\underline{\boldsymbol{A}} + \int \mathcal{S} \bullet dV = 0 \tag{1.22}$$

that is then discretized into an equation whose residual can be computed in each cell,

$$\sum\nolimits_f \underline{\boldsymbol{\Phi}}_f \bullet \underline{\boldsymbol{A}}_f + \mathcal{S}_{cv} V_{cv} = 0 \tag{1.23}$$

in which the subscript f denotes a face and the subscript cv denotes the entire control volume.

An iteration of the FVM is laid out in Figure 1.5 as a flow chart. The solver computes approximations of concentration gradients and uses them to calculate fluxes for the current iteration. Fluxes at boundaries containing Neumann or Robin boundary conditions are computed based on the specified boundary condition. Equation 1.23 is then solved for concentration using these fluxes. The newly calculated concentrations vary from the previous ones by a correction term. Usually, it is beneficial to dampen the corrections to avoid numerical divergence, so they are multiplied by an under-relaxation factor (URF) between 0 and 1. The concentrations are updated, excluding those at boundaries that are fixed by Dirichlet conditions. Equation 1.23 is solved again, using the new concentrations, for corrected fluxes. The flux correction is under-relaxed in a similar manner, and then face fluxes are updated, leaving boundary condition fluxes undisturbed. This completes one iteration of the FVM via what is known as the SIMPLE algorithm.

Objectives

Two-phase flow in PEMWE cells has been studied using three-dimensional (3D) CFD simulations in literature. Olesen et al. (Olesen, Rømer and Kær 2016) compared mass flow distributions through the channels of an interdigitated circular cell among two models – one two-phase mixture model with uniform gas generation at the electrode and another

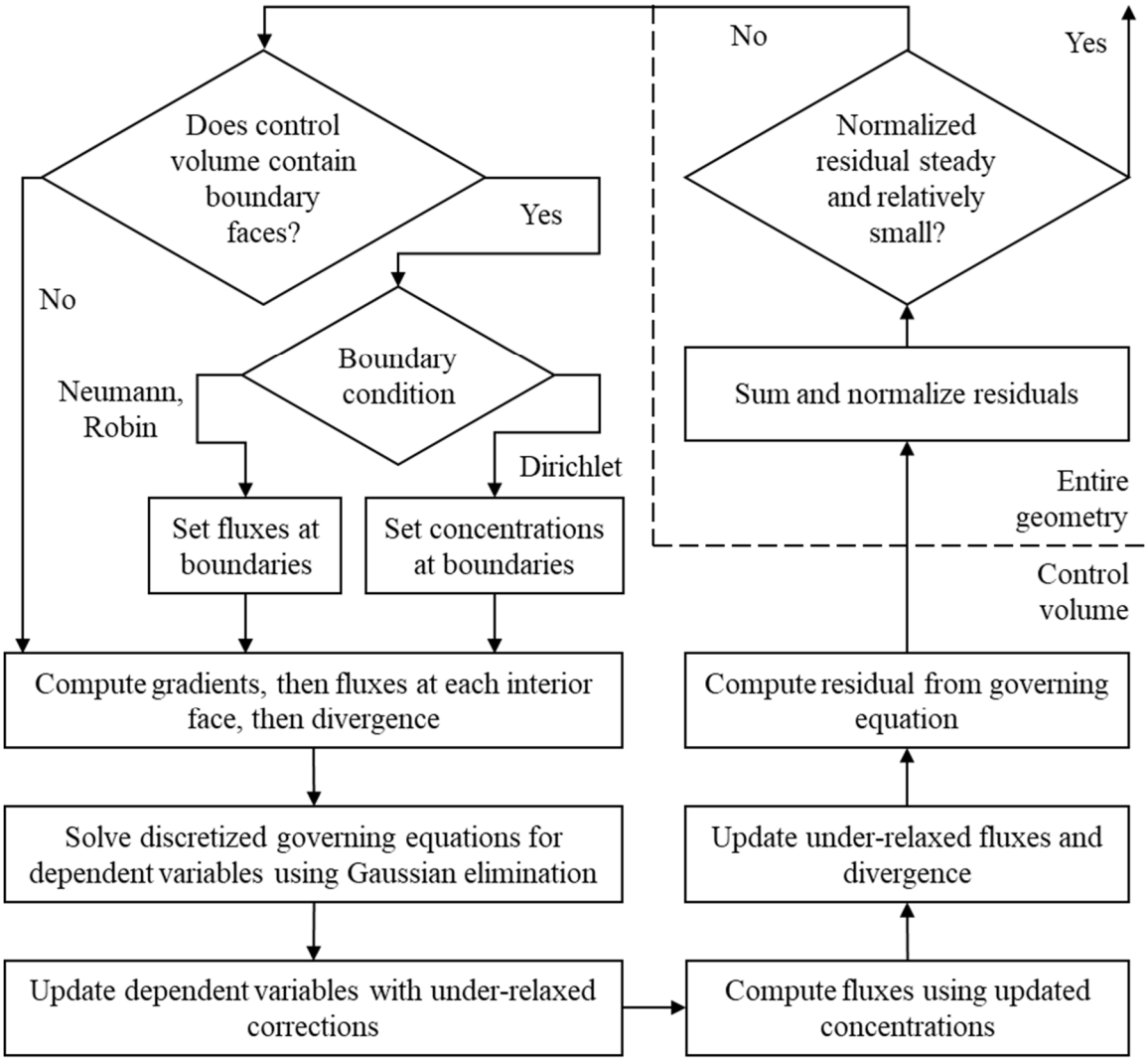

Figure 1.5: Flow diagram of the finite volume method iteration process.

single-phase model without gas generation, or what is known as “cold flow.” They found that in their system, despite predicted void fractions of up to 0.39 in the PTL, the change in the mass flow distribution was miniscule. The authors warn that at lower feed rates, the result may not be the same. Lafmejani et al. (Lafmejani, Olesen and Kær 2017) developed a volume-of-fluid (VOF) model to resolve the interface between the liquid and gas phases in channels. While their results were favorable when compared to flow visualization experiments, they did not use the entire interdigitated circular cell geometry to compare flow distributions between the VOF and mixture models. VOF modeling has a high computational load, which is likely the reason. These two studies used a constant current density assumption and neglected phase change.

CFD methods enable studying the connection between fluid flow and current distributions. 3D models can incorporate effects driven by manifold or flow field geometry as well as porous media properties. Toghyani et al. (S. Toghyani, E. Afshari, et al. 2018) developed a 3D PEMWE model using CFD and used it to predict that a single-path serpentine flow field configuration was the most effective, offering the highest cell performance. Current density was higher adjacent to the flow field ribs than near the channels, which the authors mention but do not explain. This was likely caused by the shorter electron path through the PTL near the ribs. Current density distributions were obtained from the anode, showing a high current density at the inlet that decreased along the channels as water was consumed and became less available. In later work, Toghyani et al. (Toghyani, Afshari and Baniasadi 2018) used a similar model to compare cell performance among four types of flow fields, with the model predicting that using a nickel foam in a single large channel as a flow distributor resulted in better performance.

Thereafter, the model was then applied to a novel flow field pattern (Toghyani, Afshari and Baniasadi 2019). While current density distributions are obtained, these three papers assume that water exists only in the vapor phase, despite usually existing below the boiling point. The authors claim that two-phase flow effects are negligible at low current density and that a gas-phase model is sufficient for obtaining current distributions. However, the models underpredict cell potential quite significantly at current densities of 1.0 A cm^{-2} or higher when compared to experimental data from others (Hansen, et al. 2012, Debe, et al. 2012), The poor fit is likely related to resistance and is not necessarily attributed to flow. Nevertheless, two-phase flow is very important to understand for the reasons mentioned in this introduction.

From the literature review, one can gather that there is a need to understand how two-phase flow affects current distributions in three dimensions. Elucidating effects of flow channel geometry on local quantities of variables that impact the efficiency of the OER and HER is necessary for the enlightened design of flow fields and porous media. 3D models will be presented in Chapters 2 through 4 to address this need, and Chapter 5 will evaluate the cause of resistance at interfaces between porous media and separators.

CHAPTER 2

THE PSEUDO-TWO-PHASE MIXTURE MODEL

Model Development

The pseudo-two-phase mixture (P2PM) assumption describes a two-phase mixture with miscible phases occupying the same pressure field. Volume fractions are calculated from superficial mass fractions and densities of species, and the volume fractions are used for weighted averaging of the appropriate governing equation terms. This requires one equation each for mass and momentum. Phase slip is considered using Equation 1.18. At extremely low liquid volume fractions, occurring often for low-feed-rate PEMWE, the liquid weight fraction and gradient thereof were on an order comparable to those of the gaseous species, thus the problem was well-scaled under these scenarios. The P2PM model was used to determine the electrode reaction conditions and hence the cell performance for both PEMWE and ADWE cells.

Theoretically speaking, given sufficient information, such a model should be able to accurately describe steady-state volume fraction distributions in porous media representing the time-averaged state of a heterogeneous, transient two-phase system with moving phase boundaries within a detailed pore structure. Mixture assumptions become more impactful in flow field channels, where bubble growth and agglomeration affect the flow of liquid water. The P2PM is likely to influence the fluid composition at the interface between the channels and the PTL.

In porous media, provided there are enough pores to cause separate phases to behave as though they are mixed, the load-bearing assumptions pertain to the components of the governing equations themselves, rather than the chosen mathematical method. Here, these assumptions are listed in order of importance: 1) capillary pressure and capillary diffusivity may be described accurately using a Leverett function, which adequately captures the effects of the PTL pore structure – this is not necessarily the case, as the Leverett function utilized in this work is not universal and should vary with pore structure; 2) relative permeabilities are adequately described by the Wyllie model – this does not consider any properties of the porous medium, only the interaction between the liquid and gas phases; 3) porous viscous resistance and capillary force are mean quantities that apply to the entire fluid volume – this may impact the average velocity, but as long as the velocities of the liquid and gas phases with respect to the average are somewhat large, the effect of this, if any, should be minimal.

Governing Equations.

The general forms of the governing equations are already given in Equations 1.14-19, so this section provides the specific terms of those equations. To start, the respective mass-, mole-, and volume-weighted average properties are defined simply as

$$\hat{\varphi} = \sum_i w_{S,i}\varphi_i \tag{2.1}$$

$$\breve{\varphi} = \sum_i y_{S,i}\varphi_i \tag{2.2}$$

$$\bar{\varphi} = \sum_i s_i\varphi_i \bigvee \sum_{\Pi} s_{\Pi}\varphi_{\Pi} \tag{2.3}$$

with $w_{S,i}$, $y_{S,i}$, and s_i being the superficial weight, superficial mole, and volume fractions. The liquid saturation will be denoted, without subscripts, s. This variable is also known as the liquid saturation. Indices i and Π denote a single species and a multi-component phase,

respectively. The OR operator used in Equation 2.3 implies that properties may sometimes be weighted differently within a single phase; for this reason, volume-weighted averages will be defined hereafter if they are not calculated using the term preceding the OR operator.

Capillary Forces.

There is assumed to be one pressure field in which the characteristic pressure is that of the gas phase, so the pressure-driven momentum transport term is $-\nabla P \bullet \underline{\underline{\boldsymbol{I}}} = -\nabla P_G \bullet \underline{\underline{\boldsymbol{I}}}$, with the subscript G representing the gas phase. The capillary force is derived using the definition of a relative-mobility-weighted average pressure (Wang and Beckermann 1993),

$$-\nabla \tilde{P} = -v_G \nabla P_G - v_L \nabla P_L \tag{2.4}$$

in which the relative mobilities are functions of the relative permeabilities k_G and k_L,

$$v_G = \left(1 + \frac{k_L \rho_L \mu_G}{k_G \rho_G \mu_L}\right)^{-1} \tag{2.5}$$

$$v_L = \left(1 + \frac{k_G \rho_G \mu_L}{k_L \rho_L \mu_G}\right)^{-1} \tag{2.6}$$

The capillary force is assigned to the body force term $\underline{\boldsymbol{f}}$ such that

$$-\nabla \tilde{P} = -\nabla P_G \bullet \underline{\underline{\boldsymbol{I}}} + \underline{\boldsymbol{f}} \tag{2.7}$$

Substituting the definition of P_L as the difference between the gas and capillary pressures into Equation 2.4,

$$-\nabla \tilde{P} = -v_G \nabla P_G - v_L \nabla P_G + v_L \nabla P_C \tag{2.8}$$

with P_C being the capillary pressure. The sum of relative mobilities is unity, so the result for the capillary force term is

$$\underline{\boldsymbol{f}} = \upsilon_L \nabla P_C \tag{2.9}$$

The capillary pressure is a function of the liquid surface tension (γ) and the contact angle (θ), porosity (ε), and permeability (κ) of the porous medium. It is often defined using a Leverett function (J), an empirical quantity that assumes a relationship with liquid saturation (Udell 1983):

$$P_C = \gamma \cos\{\theta\} \sqrt{\varepsilon/\kappa}\, J \tag{2.10}$$

$$J = 1.417(1 - s) - 2.12(1 - s)^2 + 1.263(1 - s)^3 \tag{2.11}$$

The liquid surface tension is dependent on temperature and in the case of an aqueous electrolyte, the concentration. The surface tension of water in N m^{-1} can be found in the National Institute of Standards and Technology (NIST) thermochemical properties database (Lemmon, McLinden and Friend 2017) and a linear function can be fitted to within 0.5% error between 298.16 and 373.16 K:

$$\gamma_w = -1.74272 \times 10^{-4}\, T + 0.124174 \tag{2.12}$$

The surface tension of KOH solution was measured by Dunlap and Faris (Dunlap and Faris 1962) versus solution density, to which Equation 2.13 fits within about 1.0% error over their data range with density in units of kg m^{-3}:

$$\gamma_{KOH} = 7.25394 \times 10^{-5}\, \rho_{KOH} - 9.93253 \times 10^{-4} \tag{2.13}$$

The liquid saturation s is defined by superficial weight fractions:

$$s = \frac{w_{S,w}/\rho_w}{\sum_i w_{S,i}/\rho_i} \tag{2.14}$$

with the densities (kg m^{-3}) of liquid water (Kell 1975), KOH solution (Novotný and Söhnel 1988), and water vapor (fitted to within 0.3% error between 0.6 and 1.5 atm) (Lemmon, McLinden and Friend 2017), respectively, being

$$\rho_w = \big(999.83952 + 16.94517\,T - 0.0079870401\,T^2 - 4.6170461\times10^{-5}\,T^3 + 1.0556302\times10^{-7}\,T^4 - 2.8054253\times10^{-10}\,T^5\big)/(1 + 0.01687985\,T) \quad (2.15)$$

T in °C

$$\rho_{KOH} = 999.65 + 0.20438\,T - 0.06174\,T^{1.5} + 54.59\,C_{KOH} - 0.1156\,C_{KOH}T + 0.001009\,C_{KOH}T^2 - 4.383\,C_{KOH}^{1.5} + 0.02343\,C_{KOH}^{1.5}T - 1.865\times10^{-4}\,C_{KOH}^{1.5}T^2 \quad (2.16)$$

T in °C

$$\rho_{wv} = 5.51107\times10^{-6} * P + 0.037808 \quad (2.17)$$

P in Pa

and the densities of hydrogen and oxygen approximated using the ideal gas law. Finally, relative permeabilities are defined using the well-known Wyllie model, with $k_L = s^3$ and $k_G = (1-s)^3$, fully describing the capillary force term.

Viscous Momentum Losses.

Viscous forces are described using the viscous stress tensor $\underline{\underline{\boldsymbol{T}}}$, which for a compressible Newtonian fluid is

$$\underline{\underline{\boldsymbol{T}}} = 2\bar{\mu}\left[\underline{\underline{\boldsymbol{E}}} - \frac{1}{3}\left(\nabla \bullet \underline{\hat{\boldsymbol{v}}}\right)\bullet \underline{\underline{\boldsymbol{I}}}\right] \quad (2.18)$$

while the strain tensor $\underline{\underline{\boldsymbol{E}}}$ is half the sum of the velocity gradient and its transpose,

$$\underline{\underline{\boldsymbol{E}}} = \frac{1}{2}\left[\nabla\underline{\hat{\boldsymbol{v}}} + \left(\nabla\underline{\hat{\boldsymbol{v}}}\right)^{\top}\right] \quad (2.19)$$

The porous media viscous resistance $\underline{\underline{\boldsymbol{R}}}$ is a relative-permeability-weighted combination of parallel resistances,

$$\underline{\underline{\boldsymbol{R}}} = \frac{1}{\kappa}\left[\frac{k_L}{\mu_L} + \frac{k_G}{\overline{\mu}_G}\right]^{-1} \bullet \underline{\underline{\boldsymbol{I}}} \tag{2.20}$$

The dynamic viscosities of liquid water (Kampmeyer 1952), KOH solution (Chemical Rubber Company (CRC) 1992), water vapor (fitted to within 0.1% error between 0.6 and 1.5 atm) (Lemmon, McLinden and Friend 2017), hydrogen and oxygen (Crane Company 1988, Chemical Rubber Company (CRC) 1984) in Pa s are as follows:

$$\mu_w = T^{1.5} * 10\text{^} \left\{ \frac{7.55865 \times 10^7}{T^3} - \frac{5.47314 \times 10^5}{T^2} + \frac{2.18772 \times 10^3}{T} - 10.795 \right\} \tag{2.21}$$

T in K

$$\mu_{KOH} = 10^{-3} * \exp\{\left(-9.6278 \times 10^{-5}\, T + 0.0324536\right) C_{KOH}^2 + \left(8.00428 \times 10^{-4}\, T - 0.138153\right) C_{KOH} + 6.28356 \times 10^{-5}\, T^2 - 0.0574972\, T + 11.4473\} \tag{2.22}$$

T in K, C_{KOH} in M

$$\mu_{wv} = -3.79625 \times 10^{-17}\, P^2 + 1.7407 \times 10^{-11}\, P + 1.08872 \times 10^{-5} \tag{2.23}$$

P in Pa

$$\mu_{H_2} = \mu_{H_2}^{ref} \frac{T_{H_2}^{ref} + 72}{T + 72}\left(\frac{T}{T_{H_2}^{ref}}\right)^{1.5} \tag{2.24}$$

T in °R

$$\mu_{O_2} = \mu_{O_2}^{ref} \frac{T_{O_2}^{ref} + 127}{T + 127}\left(\frac{T}{T_{O_2}^{ref}}\right)^{1.5} \tag{2.25}$$

T in °R

Constitutive Relationships.

Equations 1.16-19 contain divergence terms describing the material accelerations of neutral species, charged species, energy, and charge fluxes. The neutral species diffusion flux with respect to $\bar{\rho}\underline{\hat{\boldsymbol{v}}}$ is approximated by Fick's law,

$$\underline{\boldsymbol{n}}_i = -\bar{\rho} D_{i-m} \nabla w_{S,i} \tag{2.26}$$

with D_{i-m} being the effective binary diffusivity of i in the medium. D_{i-m} is derived from binary diffusivities D_{i-j}:

$$D_{i-m} = \varepsilon^{1.5} \frac{1 - x_i}{\sum_{j \neq i} x_j / D_{i-j}} \tag{2.27}$$

For gases, D_{i-j} is a function of temperature and pressure and can be calculated using data from Marrero's thesis (Marrero 1970),

$$D_{H_2-wv} = (1-s)^{1.5} D^{ref}_{H_2-wv} \frac{P^{ref}}{P} \left(\frac{T}{T^{ref}_{H_2-wv}} \right)^{1.75} \tag{2.28}$$

T in K, P in Pa

$$D_{O_2-wv} = (1-s)^{1.5} D^{ref}_{O_2-wv} \frac{P^{ref}}{P} \left(\frac{T}{T^{ref}_{O_2-wv}} \right)^{1.75} \tag{2.29}$$

T in K, P in Pa

To allow liquid and gas phases to slip past each other, a phase diffusivity is used to describe the apparent diffusion of liquid water through gaseous species and vice versa. In non-porous regions, the phase diffusivity is assumed to be the volume-weighted average of molecular diffusivities,

$$D_{L-G} = s D_{w-w} + (1-s) D_{H_2,O_2-wv} \tag{2.30}$$

in which D_{w-w} is the self-diffusivity of liquid water. This effectively bases the phase

diffusivity on the volume-weighted average Schmidt number. In porous regions, a capillary diffusivity for two-phase flow with high density ratios is derived from the Muskat generalization of Darcy's Law for multiphase flow,

$$\overline{\rho}\underline{\hat{\boldsymbol{v}}} = -s\rho_L \frac{k_L \kappa}{\mu_L} \nabla P_L - (1-s)\overline{\rho}_G \frac{k_G \kappa}{\overline{\mu}_G} \nabla P_G \tag{2.31}$$

with liquid velocity with respect to the grid (i.e. 0) defined as

$$\underline{\boldsymbol{v}}_{\boldsymbol{L}} = -\frac{k_L \kappa}{\mu_L} \nabla P_L \tag{2.32}$$

the liquid velocity with respect to the mass-averaged velocity can be written

$$\underline{\boldsymbol{v}}_{\boldsymbol{L}} - \underline{\hat{\boldsymbol{v}}} = \left(\frac{s\rho_L}{\overline{\rho}} - 1\right) \frac{k_L \kappa}{\mu_L} \nabla P_L + \frac{(1-s)\overline{\rho}_G}{\overline{\rho}} \frac{k_G \kappa}{\overline{\mu}_G} \nabla P_G = -\varepsilon^{1.5} \frac{D_{L-G}}{w_{S,L}} \nabla w_{S,L} \tag{2.33}$$

Next, recognizing that the density-containing factors in Equation 2.33 are equal and opposite,

$$-\varepsilon^{1.5} \frac{D_{L-G}}{w_{S,L}} \nabla w_{S,L} = \left(\frac{s\rho_L}{\overline{\rho}} - 1\right) \left(\frac{k_L \kappa}{\mu_L} \nabla P_L - \frac{k_G \kappa}{\overline{\mu}_G} \nabla P_G\right) \tag{2.34}$$

then solving for D_{L-G},

$$D_{L-G} = \varepsilon^{-1.5} w_{S,L} \left(1 - \frac{s\rho_L}{\overline{\rho}}\right) \left(\frac{k_L \kappa}{\mu_L} \frac{\nabla P_L}{\nabla w_{S,L}} - \frac{k_G \kappa}{\overline{\mu}_G} \frac{\nabla P_G}{\nabla w_{S,L}}\right) \tag{2.35}$$

The weight fraction gradient is then factored to express the diffusivity in terms of the liquid saturation, which becomes convenient in a later step. Volume averaging the terms in the denominator of Equation 2.14 belonging to gaseous species, setting the mass fraction of gas equal to $1 - w_{S,L}$, and differentiating with respect to $w_{S,L}$, one finds that

$$\frac{\partial s}{\partial w_{S,L}} = \frac{\rho_L \overline{\rho}_G}{\left[w_{S,L}\left(\overline{\rho}_G - \rho_L\right) + \rho_L\right]^2} \tag{2.36}$$

To reduce the number of computations, Equation 2.36 may be approximated as

$$\frac{\partial s}{\partial w_{S,L}} \cong \frac{s^2 \rho_L}{w_{S,L} \overline{\rho}_G} \tag{2.37}$$

so factoring the weight fraction gradient,

$$D_{L-G} = \varepsilon^{-1.5} \frac{s^2 \rho_L}{w_{S,L} \overline{\rho}_G} \left(1 - \frac{s\rho_L}{\overline{\rho}}\right) \left(\frac{k_L \kappa}{\mu_L} \frac{\nabla P_L}{\nabla s} - \frac{k_G \kappa}{\overline{\mu}_G} \frac{\nabla P_G}{\nabla s}\right) \tag{2.38}$$

The liquid pressure gradient can then be decomposed to more convenient terms of gas pressure and capillary pressure gradients,

$$D_{L-G} = \varepsilon^{-1.5} \frac{s^2 \rho_L}{w_{S,L} \overline{\rho}_G} \left(1 - \frac{s\rho_L}{\overline{\rho}}\right) \kappa \left[\left(\frac{k_L}{\mu_L} - \frac{k_G}{\overline{\mu}_G}\right) \frac{\nabla P_G}{\nabla s} - \frac{k_L}{\mu_L} \frac{\nabla P_C}{\nabla s}\right] \tag{2.39}$$

and after substituting the definition of the capillary pressure gradient and simplifying, using a "scalar quotient" defined as the projection of the pressure gradient divided by the square of the magnitude of the liquid saturation gradient (see Appendix A),

$$\begin{aligned} D_{L-G} = \varepsilon^{-1.5} \frac{s^2 \rho_L}{w_{S,L} \overline{\rho}_G} \left(1 - \frac{s\rho_L}{\overline{\rho}}\right) \kappa \left[\left(\frac{k_L}{\mu_L} - \frac{k_G}{\overline{\mu}_G}\right) \nabla P_G \div \nabla s \right. \\ \left. - \frac{k_L}{\mu_L} \gamma \cos\{\theta\} \sqrt{\frac{\varepsilon}{\kappa}} \frac{dJ}{ds}\right] \end{aligned} \tag{2.40}$$

If the liquid saturation is known to be above 0.01 at all locations, such as when the liquid feed rate is very high, the factor at the beginning of Equation 2.40 may be simplified:

$$D_{L-G} = \varepsilon^{-1.5} s(1-s) \kappa \left[\left(\frac{k_L}{\mu_L} - \frac{k_G}{\overline{\mu}_G}\right) \nabla P_G \div \nabla s - \frac{k_L}{\mu_L} \gamma \cos\{\theta\} \sqrt{\frac{\varepsilon}{\kappa}} \frac{dJ}{ds}\right] \tag{2.41}$$

In order to apply Equation 2.40 to cases involving very low liquid saturations of less than 10^{-4}, the beginning factor should have constant lower limits approximately equal to the gas:liquid density ratio (about 10^{-3}) imposed to keep the approximation from underestimating D_{L-G}:

$$D_{L-G} = \varepsilon^{-1.5} \max\left\{10^{-3}, \frac{s^2 \rho_L \left(1 - \frac{s\rho_L}{\overline{\rho}}\right)}{\max\left\{10^{-3}, w_{S,L}\right\} \overline{\rho}_G}\right\} \kappa \left[\left(\frac{k_L}{\mu_L} - \frac{k_G}{\overline{\mu}_G}\right) \nabla P_G \div \nabla s - \frac{k_L}{\mu_L} \gamma \cos\{\theta\} \sqrt{\frac{\varepsilon}{\kappa}} \frac{dJ}{ds}\right] \quad (2.42)$$

The derivative of the Leverett function can be obtained from the differentiation of Equation 2.11. However, this is not applicable when the liquid saturation is extremely low. The data presented by Leverett (Leverett 1940) suggests that the derivative may approach negative infinity at low liquid saturations with the onset depending on the pore hierarchy of the medium, with onsets in clayey sands occurring at higher liquid saturations than in clean sands. To avoid an extremely large capillary force term in the momentum equation leading to local discontinuities, Equation 2.11 was kept as is when calculating capillary pressure. Note that this may have led to underestimated pressure at extremely low liquid saturations. The capillary diffusivity in Equation 2.42 was calculated using the following modification of Equation 2.11 and its derivative:

$$J = 1.417(1 - s) - 2.12(1 - s)^2 + 1.263(1 - s)^3 + 3.\overline{3} \times 10^{10} \exp\{-1500s\} \quad (2.43)$$

$$\frac{dJ}{ds} = 3.789s^2 - 3.338s - 1.868 - 5 \times 10^{13} \exp\{-1500s\} \quad (2.44)$$

Finally, it is important to apply a lower limit on the capillary diffusivity. Equation 2.42 can return negative values before a converged solution is found, but it is sufficient to instead reduce D_{L-G} to Equation 2.30 to form species gradients slowly. The solver cannot handle changes in sign for D_{L-G}, and it is unnecessary. Capillary diffusivity was underrelaxed using a factor of 0.5 at the anode and 0.05 at the cathode to avoid large fluctuations caused by gradient shifting prior to solution convergence (Lopata, Weidner, et al. 2022).

For ADWE, the charged species flux is represented using the Nernst-Planck equation, not including the convective term already given on the left-hand side of Equation 1.19:

$$\underline{\boldsymbol{N}_i} = -z_i C_{S,i} u_{S,i} F \nabla \phi - D_{S,i-L} \nabla C_{S,i} \tag{2.45}$$

in which z_i, $u_{S,i}$, $C_{S,i}$, and $D_{S,i-L}$ are the ion charge number, superficial ionic mobility, superficial concentration, and superficial diffusivity. The superficial values are derived from the actual values and they are required in order to model ion transport through the liquid phase as opposed to the entire continuum. Consider the following equation for diffusive molar flux:

$$\underline{\boldsymbol{J}_i} = -D_{S,i-L} \nabla C_{S,i} = -D_{i-L} \nabla C_i \tag{2.46}$$

The definition of the actual concentration is $C_i = C_{S,i}/s$. Substituting this into Equation 2.46, applying the quotient rule, and solving for $D_{S,i-L}$, assuming that the superficial concentration and liquid saturation gradients are co-parallel:

$$D_{S,i-L} = \frac{D_{i-L}}{s}\left(1 - C_i \frac{\|\nabla s\|}{\left\|\nabla C_{S,i}\right\|}\right) \tag{2.47}$$

Because phase slip occurs on a much smaller time scale than ionic diffusion, the diffusivity of KOH is assumed to be the phase diffusivity, with $D_{i-L} = D_{L-G}$. The superficial mobility, which accounts for the non-ideality of the concentrated KOH solution used for ADWE, is derived by equating Equation 2.46 with a more general equation for flux (Newman and Thomas-Alyea 2004),

$$\begin{aligned} &-z_i C_{S,i} u_{S,i} F \nabla \phi - D_{S,i-L} \nabla C_{S,i} \\ &\qquad = -\frac{D_{KOH}}{RT} \frac{z_j}{t_j\left(z_j - z_i\right)} \frac{m_0}{m_t}\left(1 + \frac{d \ln\{\gamma_\pm\}}{d \ln\{m_i\}}\right)^{-1} C_i \nabla_{\underline{M}_i} \end{aligned} \tag{2.48}$$

with D_{KOH}, z_j, t_j, m_0, m_t, $Y_{\pm}$, m_i, and μ_i denoting the actual mean diffusivity of the electrolyte in liquid water, counter-ion charge number, counter-ion transference number, reference molality, total molality, mean molal activity coefficient, ion molality, and electrochemical potential, respectively. The diffusive term on the left-hand side can be substituted with the right-hand side of Equation 2.46:

$$z_i C_{S,i} u_{S,i} F \nabla \phi + D_{i-L} \nabla C_i = \frac{D_{KOH}}{RT} \frac{z_j}{t_j (z_j - z_i)} \frac{m_0}{m_t} \left(1 + \frac{d \ln\{Y_{\pm}\}}{d \ln\{m_i\}} \right)^{-1} C_i \nabla \mu_i \tag{2.49}$$

Assuming that the concentration gradient is very small, which is almost always true at practical feed rates, $\nabla \mu_i = z_i F \nabla \phi$, and applying the definition of the superficial concentration, the mobility for a uni-univalent electrolyte is therefore

$$u_{S,i} = \frac{D_{KOH}}{2 t_j s RT} \frac{m_0}{m_t} \left(1 + \frac{d \ln\{Y_{\pm}\}}{d \ln\{m_i\}} \right)^{-1} \tag{2.50}$$

Heat flux is given by the following:

$$\underline{q} = -\lambda \nabla T \tag{2.51}$$

in which λ is the effective thermal conductivity of the conducting medium, given in W m^{-2} K^{-1} as linear functions of temperature (K) for gaseous species in the below equations:

$$\lambda_{H_2} = 44.79 + 0.4586\, T \tag{2.52}$$

$$\lambda_{O_2} = 3.36 + 0.0759\, T \tag{2.53}$$

$$\lambda_{wv} = 7.23333 + 0.085\, T \tag{2.54}$$

The charge flux, or current density, is specified by Ohm's Law:

$$\underline{i} = -\sigma \nabla \phi \tag{2.55}$$

in which σ is the effective electrical or ionic conductivity of the conducting medium. The conductivities of the proton exchange membrane Nafion® and the alkaline diaphragm

Zirfon® are as follows:

$$\sigma_{pem} = \frac{0.502513}{-6.03058 \times 10^{-4}\, T + 0.246674} \tag{2.56}$$

$$\begin{aligned} \sigma_{ad} = \varepsilon_{ad}^{b_{ad}} \Big[& -0.342001\, T + 0.001197\, T^2 - 117.298\, C_{KOH} \\ & - 0.516794\, C_{KOH}^2 + 0.328293 T C_{KOH}^2 \\ & + \frac{1.19605 \times 10^4\, C_{KOH}^2}{T} + 0.0624312\, C_{KOH}^3 \\ & - 1.8832 \times 10^{-5}\, (T C_{KOH})^2 \Big] \end{aligned} \tag{2.57}$$

Equation 2.56 is an empirical fit of experimental PEMWE cell conductivity versus temperature when the membrane is fully hydrated, while Equation 2.57 is the KOH conductivity given by See and White (See and White 1997) multiplied by a porous media property factor used to obtain an effective, reduced value for ADWE.

Constant-value properties not specified in this or further sections are provided in Table 2.1 for the PEMWE cell model and Table 2.2 for the ADWE cell model.

Source Terms.

Evaporation is an important process in PEMWE for several reasons. As explained previously, water vapor participates in the reaction, so the rate of evaporation affects the contribution of the gas phase to the total current density. Evaporative cooling also depends on evaporation rate and competes with heat production at the anode and within the membrane to influence the temperature, which impacts kinetics. The composition of the gas phase influences the gas-phase equilibrium potential. When water vapor is present, the density of the gas phase is reduced, possibly affecting the gas volume fraction, also known as void fraction. To control the evaporation rate in the PTL and channels of the cell,

Table 2.1: PEMWE Model Parameters

Symbol	Property	Region/Boundary	Value	
c_{P,H_2}	Specific heat of hydrogen	All fluid regions	14,292.3 J kg^{-1} K^{-1}	
c_{P,O_2}	Specific heat of oxygen	All fluid regions	920.425 J kg^{-1} K^{-1}	
$c_{P,PEEK}$	Specific heat of PEEK		320 J kg^{-1} K^{-1}	
$c_{P,Ti}$	Specific heat of titanium	CCs	528 J kg^{-1} K^{-1}	
$c_{P,w}$	Specific heat of water	All fluid regions	4,181.35 J kg^{-1} K^{-1}	
$D^{ref}_{H_2-wv}$	Reference diffusivity of H_2 in water vapor	All fluid regions	1.012e-4 m^2 s^{-1}	[1]
$D^{ref}_{O_2-wv}$	Reference diffusivity of O_2 in water vapor	All fluid regions	2.82e-5 m^2 s^{-1}	[1]
K	Interphase mass transfer coefficient	Electrodes	0.0325 kg m^{-2} s^{-1}	
		Flow fields	2.00e-8 kg m^{-2} s^{-1}	
		PTLs	7.25e-6 (1.45e-5 PTL1-2Xevap) kg m^{-2} s^{-1}	
P^{ref}	Reference pressure	All fluid regions	1 atm	
$T^{ref}_{H_2}$	Reference temperature for hydrogen viscosity	All fluid regions	528.93 °R	[2]
$T^{ref}_{O_2}$	Reference temperature for oxygen viscosity	All fluid regions	526.05 °R	[2]
$T^{ref}_{H_2-wv}$	Reference temperature for diffusion of H_2 in water vapor	All fluid regions	308.05 K	[1]
$T^{ref}_{O_2-wv}$	Reference temperature for diffusion of O_2 in water vapor	All fluid regions	322.65 K	[1]
U	Convective heat transfer coefficient	External surfaces	35 W m^{-2} K^{-1}	
		Membrane edges	3.5 W m^{-2} K^{-1}	
ε	Porosity	Anode PTL	PTL1: 0.312 | PTL2: 0.218 | Modified: 0.650	
		Cathode PTL	0.312	
θ	Wetting-phase contact angle	PTLs	0.52 radians	
κ	Intrinsic permeability	Anode PTL	PTL1: 1.1e-12 m^2 | PTL2: 3.2e-13 m^2	
		Cathode PTL	1.1e-12 m^2	
λ_w	Thermal conductivity of water	All fluid regions	62.5 W m^{-1} K^{-1}	
$\mu^{ref}_{H_2}$	Reference viscosity of hydrogen	All fluid regions	8.76e-6 Pa s	[2]
$\mu^{ref}_{O_2}$	Reference viscosity of oxygen	All fluid regions	2.018e-5 Pa s	[2]
ν^{eo}_{pem}	Electroosmotic drag coefficient	Electrodes	2.7	[3]
σ	Electrical/ionic conductivity	CCs	24.5 W m^{-1} K^{-1}	
		PTLs	$\frac{1-\varepsilon}{\tau} * 24.5$ W m^{-1} K^{-1}	
		Species	0	

[1] (Marrero 1970)
[2] (Chemical Rubber Company (CRC) 1984, Crane Company 1988)
[3] (Zawodzinski Jr., et al. 1993)

Table 2.2: ADWE Model Parameters

Latin Param.	Value	Unit	
$D^{ref}_{H_2-O_2}$	4.17e-05	$m^2\ s^{-1}$	5
$D^{ref}_{H_2-wv}$	1.012e-04	$m^2\ s^{-1}$	5
$D^{ref}_{O_2-wv}$	2.82e-05	$m^2\ s^{-1}$	5
E_{cell}	{1.6, 1.8, 2.0, 2.2, 2.4}	V	
$E^{\circ}_{eq,a}$	1.2288	V vs. $E^{\circ}_{eq,c}$	
$E^{\circ}_{eq,c}$	0	V vs. $E^{\circ}_{eq,c}$	
F	96,485,333	$C\ kmol^{-1}$	
L_{ad}	4.6e-04	m	
N_{Sc}	100	none	
$P^{ref}_{H_2-O_2}$	101325	Pa	5
$P^{ref}_{H_2-wv}$	101325	Pa	5
$P^{ref}_{O_2-wv}$	101325	Pa	5
Q	{8.10, 4.05, 2.03}	$L\ min^{-1}$	
$\mathscr{R}$	8314.66	$J\ kmol^{-1}\ K^{-1}$	
R_{esi}	1.35e-05	$\Omega\ m^2$	
T_{set}	353.15	K	
T_{∞}	312.15	K	
$T^{ref}_{H_2}$	293.85	K	10
$T^{ref}_{O_2}$	292.25	K	10
$T^{ref}_{H_2-O_2}$	308.05	K	5
$T^{ref}_{H_2-wv}$	308.05	K	5
$T^{ref}_{O_2-wv}$	322.65	K	5
U	100	$W\ m^{-2}\ K^{-1}$	
b_{ad}	2.3	none	4
$c_{P,ad}$	2120	$J\ kg^{-1}\ K^{-1}$	
c_{P,H_2}	14315.8	$J\ kg^{-1}\ K^{-1}$	6
c_{P,O_2}	920.425	$J\ kg^{-1}\ K^{-1}$	6
$c_{P,L}$	2979	$J\ kg^{-1}\ K^{-1}$	7
$c_{P,wv}$	1938.19	$J\ kg^{-1}\ K^{-1}$	6
$i^{ref}_{0,a}$	1.28	$A\ m^{-2}$	
$i^{ref}_{0,c}$	7.54	$A\ m^{-2}$	
k_B	1.38065e-23	$J\ K^{-1}$	

Greek Param.	Value	Unit	
α_a	1.52	none	
α_c	1.178	none	
$\epsilon_{a,c}$	0.76	none	
ϵ_{PTL}	0.67	none	
ϵ_{ad}	0.576	none	8
θ	0.52	rad	
$\kappa_{a,c,PTL}$	1.0e-08	m^2	
κ_{ad}	7.0e-16	m^2	9
λ_{Ni}	90	$W\ m^{-1}\ K^{-1}$	
λ_{ad}	1	$W\ m^{-1}\ K^{-1}$	
λ_w	0.65	$W\ m^{-1}\ K^{-1}$	
$\mu^{ref}_{H_2}$	8.76e-06	Pa s	10
$\mu^{ref}_{O_2}$	2.018e-05	Pa s	10
ν^{eo}_{ad}	0.7	none	11

[4] (Rodríguez, et al. 2019)
[5] (Marrero 1970)
[6] (Felder and Rousseau 2005)
[7] (Le Bideau, et al. 2019, Chemical Rubber Company (CRC) 1992)
[8] (Lee, Dung, et al. 2020a)
[9] (Schalenbach, Lueke and Stolten 2016)
[10] (Chemical Rubber Company (CRC) 1984, Crane Company 1988)
[11] (Haverkort 2020)

constant parameters are employed. This allows the model to demonstrate the effects of evaporation on cell performance. The evaporation rate is described as a function of the relative undersaturation $1 - h_r$,

$$\mathcal{S}_{wv} = \frac{K}{l}(1 - s)(1 - h_r) \tag{2.58}$$

in which K is a constant mass transfer coefficient with units of kg m^{-2} s^{-1} and includes an implicit factor representing the maximum specific interfacial area. In the PEMWE model, K is divided by a characteristic length l of 10^{-3} m, which is both the PTL thickness and flow field channel depth. In the ADWE model, which is not as sensitive to relative humidity, K/l was set arbitrarily to 1. The void fraction $1 - s$ is assumed to be the dimensionless liquid/gas interfacial area (LGA) in porous media except for the CL, which is treated differently and described under boundary conditions. K should be dependent on the LGAs within their respective regions. Due to the small pores in porous media, a higher K was used to describe evaporation there than in non-porous channels or manifolds. The smaller the pore size, the higher is K.

Of course, liquid water requires energy to vaporize and the energy is drawn from all the materials and species in contact with the water. The evaporative cooling source term is simply the evaporation rate times the heat of vaporization,

$$\mathcal{S}_{\Delta}^{evap} = -h_{vap}\mathcal{S}_{wv} \cong -2{,}468.12\,T + 3.17884 \times 10^{6} \tag{2.59}$$

Within the membrane, the migration of protons generates heat. Ohmic heating is the electrical power:

$$\mathcal{S}_{\Delta}^{\Omega} = \left\|\underline{\boldsymbol{i}}\right\|^2/\sigma \tag{2.60}$$

Lastly, because the reaction was assumed to occur at an infinitesimally thin interface between the PTL and membrane, or between the porous electrode and diaphragm

in ADWE, the transfer current source term $j = 0$. Though ADWE cells typically have thick electrodes that could be modeled as porous electrode regions, the interface assumption was applied with the understanding that the void fraction varied little through-plane in the simulation, and an interfacial resistance would have to be applied to compensate for neglecting a transfer current between the solid and electrolyte phases as well as account for the reduction in ion transport area within the separator.

CHAPTER 3

EFFECTS OF OPERATING CONDITIONS AND POROUS MEDIA BULK PROPERTIES ON PROTON EXCHANGE MEMBRANE WATER ELECTROLYSIS PERFORMANCE

Investigating Kinetic Limitations

Chapter 1 discussed three mechanisms through which catalyst utilization is limited: interfacial charge transport area reduction, the obstruction of ion migration pathways, and blockage of catalyst surfaces. There is already a fair understanding of how the high sheet resistance of unsupported IrO_2 leads to lower catalyst utilization when increasing the pore size of the PTL. It is believed that this is the predominant reason for catalyst underutilization, especially when there is significant strain and fracturing within the CL. However, under CL dehydration, there is an additional loss associated with the reduced conductivity of the solid electrolyte and reduced effective electrochemical surface area. These phenomena are understood, but due to the difficulty in determining the magnitudes of each of their contributions to the overpotential, especially under electrical load, the impacts of these mechanisms are seldom quantified for liquid-fed water electrolyzers. Here, 3D modeling using the approach outlined in Chapter 2 is employed to acquire a close look at the effects of kinetic limitations from bubble coverage. The equations described and explained in this chapter allow for investigation of the effects of mass transport on current distributions through kinetic limitations, neglecting in-plane CL resistance and CL ionomer resistance. Furthermore, it utilizes knowledge obtained from studying mass

transport to propose a PTL design that improves cell performance in the context of thermodynamic and kinetic A-OER favorability (Lopata, Weidner, et al. 2022).

Electrochemical Equations

The reaction stoichiometry, i.e. the coefficients ν_i, comes from Equations 1.2 through 1.4 for PEMWE. At the anode, the respective values for $\nu_{w,wv}$, ν_{O_2}, and $\nu_{H^+,a}$ are -0.5, 0.25, and 1, while at the cathode, $\nu_{H^+,c}$ and ν_{H_2} are -1 and 0.5. The production rates of species at electrodes, assumed to be interfaces between the PTL and membrane, are

$$\boldsymbol{n}_i^{rxn} = \frac{\nu_i \boldsymbol{M}_i \vec{\boldsymbol{\imath}}}{F} \tag{3.1}$$

Note that bold quantities without underbars are boundary-normal components of their parent vectors, and a single-quiver arrow denotes the direction of the normal when applicable, with $\overleftarrow{\boldsymbol{\Phi}}$ pointing toward the anode terminal and $\vec{\boldsymbol{\Phi}}$ in the direction of the cathode terminal. When protons migrate through the solid electrolyte from anode to cathode, they drag water molecules with them due to strong intermolecular attractions. This electroosmotic drag is expressed:

$$\vec{\boldsymbol{n}}_{w,wv}^{eo} = \frac{\nu_{pem}^{eo} \boldsymbol{M}_w \vec{\boldsymbol{\imath}}_{L,G}}{F} \tag{3.2}$$

As described previously, water evaporation occurs as gas is generated. This evaporation can be specified as a function of the LGA and the relative undersaturation:

$$\boldsymbol{n}_{wv,a,c}^{evap} = -\boldsymbol{n}_{w,a,c}^{evap} = K_{CL} A_{int}^{*} (1 - h_r) \tag{3.3}$$

with A_{int}^{*} being the dimensionless LGA. The LGA is directly proportional to the interfacial area of the porous medium. From the results compiled in El Ouni et al. (El Ouni, et al. 2021), it is clear that when the LGA is relatively small, it increases linearly with decreasing liquid saturation; when relatively large, the relationship becomes non-linear. Costanza-

Robinson and Brusseau (Costanza-Robinson and Brusseau 2002) proposed a relationship in which A_{int}^{*} varies non-linearly with liquid saturation, increasing with decreasing liquid saturation until reaching a turning point at $s \cong 0.05$ and plummeting when liquid water is depleted further.

The interfacial area A_{int}^{*} was expressed as a beta distribution normalized to have a peak height of 1, which was tuned to fit the model to experimental results:

$$A_{int}^{*} = 2.053256\ s^{0.1538}(1-s)^{6} \tag{3.4}$$

K_{CL} was tuned empirically in conjunction with Equation 3.4. The pre-factor and exponents of Equation 3.4, when modified, produce many variations of this beta distribution function as shown in Figure 3.1. In Figure 3.1, the bold line represents Equation 3.4. Important to note is that at the cathode, h_r approached 1 and heavy underrelaxation was needed to prevent unphysically high h_r. A URF of 0.05-0.1 was applied depending on overshoot severity.

The current density at the anode is expressed as a sum of two volume-weighted Tafel approximations of the Butler-Volmer equation, a simplification arising from interest in high overpotentials in particular:

$$\vec{\imath} = \vec{\imath}_L + \vec{\imath}_G = i_0 \left(s \exp\left\{ \frac{\alpha F \eta_{s,L}}{RT} \right\} + (1-s) h_r^{2.07-\frac{\alpha}{2}} \exp\left\{ \frac{\alpha F \eta_{s,G}}{RT} \right\} \right) \tag{3.5}$$

where i_0 is the exchange current density. While the exchange current density should increase with increasing temperature, the apparent value calculated from operando experimental data may not vary much with temperature, which was the case in experimental validation. Therefore, a constant value was assigned, and the changes in kinetic performance with temperature were resolved using a linear function of temperature for the transfer coefficient,

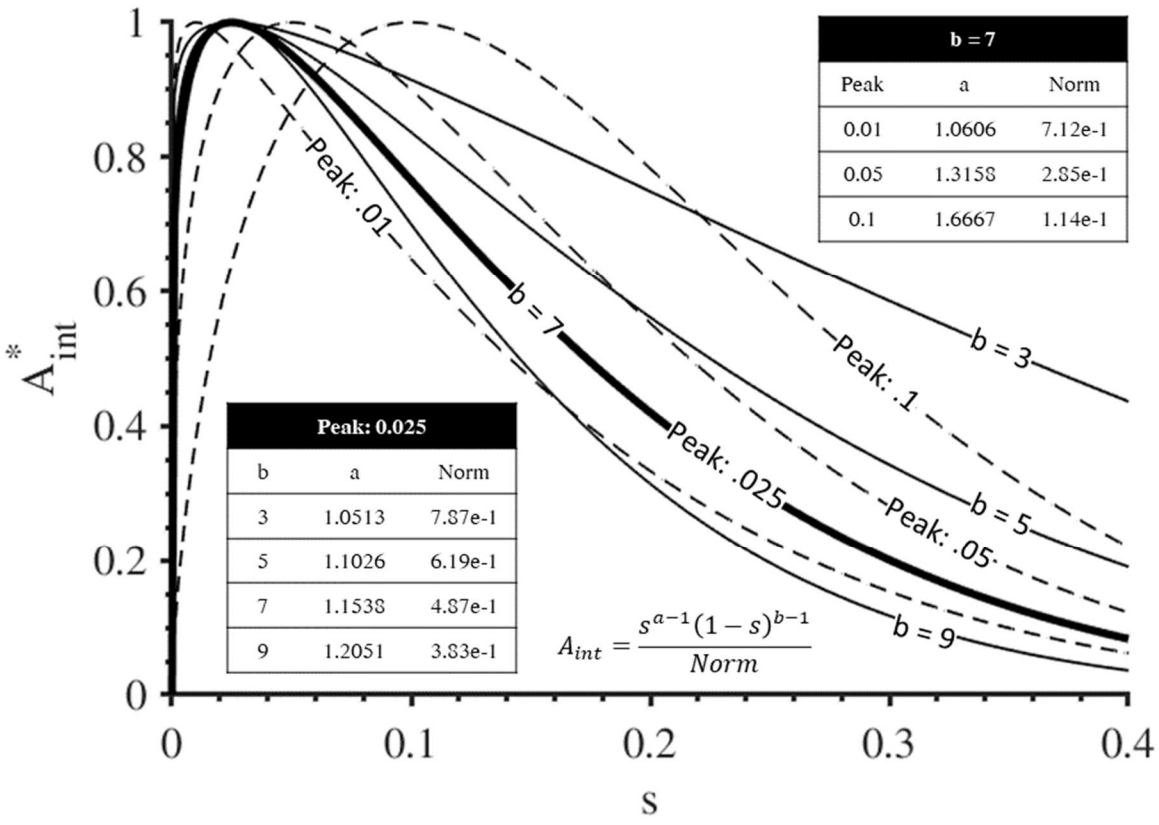

b = 7		
Peak	a	Norm
0.01	1.0606	7.12e-1
0.05	1.3158	2.85e-1
0.1	1.6667	1.14e-1

Peak: 0.025		
b	a	Norm
3	1.0513	7.87e-1
5	1.1026	6.19e-1
7	1.1538	4.87e-1
9	1.2051	3.83e-1

Figure 3.1: Beta distributions for the approximation of dimensionless specific interfacial area. Functions are normalized with peak heights of 1. The bold curve was selected to describe the dimensionless interfacial area within the catalyst layer (Lopata, Weidner, et al. 2022).

$$\alpha = 0.00601043\,T - 0.970938 \tag{3.6}$$

The second term in Equation 3.5 associated with the gas phase is dependent on the relative humidity h_r. The rate exponent is the reaction order at constant overpotential, adopted from Schuler et al. (Schuler, Kimura, et al. 2020) The liquid- and gas-phase overpotentials $\eta_{act,L}$ and $\eta_{act,G}$ are calculated from the potential drop at the anode interface and the equilibrium reduction potential of the corresponding phase:

$$\eta_{s,L} = -\Delta\phi_a - \phi^{\circ}_{eq,a,L} - \frac{\Delta S^{\circ}_{a,L}}{F}(T - T^{\circ}) + \frac{\mathscr{R}T}{F}\ln\left\{\left(1 - P^{sat}_{wv}\right)^{-1/4}\right\} \tag{3.7}$$

$$\eta_{s,G} = -\Delta\phi_a - \phi^{\circ}_{eq,a,G} - \frac{\Delta S^{\circ}_{a,G}}{F}(T - T^{\circ}) + \frac{\mathscr{R}T}{F}\ln\left\{\frac{\sqrt{P_{wv}}}{P^{1/4}_{O_2}}\right\} \tag{3.8}$$

Current density was computed using the constant potential boundary conditions at the terminals and specifying the conductivities of regions and boundaries. The use of an interfacial resistance controlled by electrochemical kinetics enforced the potential drop at the anode. A resistance value must be selected with care for each control volume face in contact with the boundary, anticipating an inevitable change in potential drop at some current density. This was achieved using a modified Newton-Raphson iterative procedure beginning with the definition of a constant resistance attributed to the entire cell, excluding the electrode interface:

$$R' = \frac{\phi_{cell} + \Delta\phi_{tk,init}}{\vec{\imath}_{init}} \tag{3.9}$$

$$\Delta\phi_{tk,init} = \Delta\phi_{total} + \vec{\imath}_{init}R_{\Omega} \tag{3.10}$$

The apparent resistance R' is directly proportional to the potential drop associated with the entire cell excluding the thermodynamic and kinetic potential drop $\Delta\phi_{tk,init}$ at the electrode of interest, the anode in this case. $\Delta\phi_{tk,init}$ and $\Delta\phi_{total}$ usually have negative values. In the

PEMWE model, the ohmic resistance of the interface R_{Ω} was neglected. The surface overpotential is defined as

$$\eta_{s,a} = -\Delta\phi_{tk,a} - \phi_{eq,a} \tag{3.11}$$

$$\eta_{s,c} = \Delta\phi_{tk,c} + \phi_{eq,c} \tag{3.12}$$

The residual, which the iterative method aims to minimize, is the difference between the current density calculated using Equation 3.5 and the average current density in the remainder of the cell,

$$\boldsymbol{i}_{res} = \vec{\boldsymbol{i}} - \frac{\phi_{cell} - \phi_{ref} + \Delta\phi_{tk}}{\boldsymbol{R'}} \tag{3.13}$$

If $|\boldsymbol{i}_{res}|$ is less than the specified tolerance, in this case 10^{-5} A m^{-2}, the thermodynamic and kinetic resistance is defined as

$$\boldsymbol{R}_{tk} = \frac{-\Delta\phi_{tk}}{\vec{\boldsymbol{i}}} \tag{3.14}$$

Otherwise, a new potential drop is calculated:

$$\Delta\phi_{tk,new} = \Delta\phi_{tk} - \boldsymbol{i}_{res}\frac{\partial\Delta\phi_{tk}}{\partial\boldsymbol{i}_{res}} \tag{3.15}$$

Note that the PEMWE model aims to study the effects of liquid saturation and relative humidity on overall kinetics and does not consider CL ionomer resistance, which is a valid assumption for thin CLs.

Heat generation at the anode and cathode boundaries is determined using Equation 1.10. The reaction entropies are calculated from the component entropies given in Equations 3.16-19, fitted to thermochemical data from NIST (Lemmon, McLinden and Friend 2017):

$$S_w = -\boldsymbol{R}\ln\{a_w\} + 0.226978\,\boldsymbol{T} + 2.53858 \tag{3.16}$$

$$S_{wv} \cong -7.15995 \ln\left\{\frac{P_{wv}}{P_0}\right\} + 195.766 \tag{3.17}$$

$$S_{H_2} = -8.31551 \ln\left\{\frac{P_{H_2}}{P_0}\right\} + 0.086722\, T + 104.7552 \tag{3.18}$$

$$S_{O_2} = -8.32569 \ln\left\{\frac{P_{O_2}}{P_0}\right\} + 0.088538\, T + 178.7332 \tag{3.19}$$

Geometry

Figure 3.2 shows the details of the cell geometry for the PEMWE model. This was a replica of a 2 cm × 2 cm benchmarking cell developed by Fraunhofer ISE. The flow fields consisted of 10 1 mm × 1 mm parallel channels on each side of the membrane. Liquid water was delivered to the flow fields from 5 injection points at the inlets and gas was expelled through 5 ejection channels near the outlets. This can be seen in Figure 3.2a, which displays the PEMWE device internals, flow fields, and manifolds without the plates and other structural components. Figure 3.2b shows the finite volume mesh at the boundaries of the internal regions. Finer meshes, thus smaller control volumes, provide more accurate solutions at the cost of computational resources. In this mesh, a face size of about 0.0667 mm was applied to the catalyst-coated membrane (CCM) in the thin middle region. Farther from the electrodes, the mesh was expanded to a target size of 0.167 mm in the flow field channels. Curvature refinement was applied to increase the mesh density near curved surfaces, which enhances the resolution. In Figure 3.2c, the anode plate and non-conductive structural components are added to illustrate the manner in which they fit around the internal parts. The complete geometry with the mesh of the external components is provided in Figure 3.2d. Note the significant size increase in control volumes from the internal components to the external components. The target mesh size at external surfaces was on the order of 1 mm. The total number of cells in the complete geometry amounted

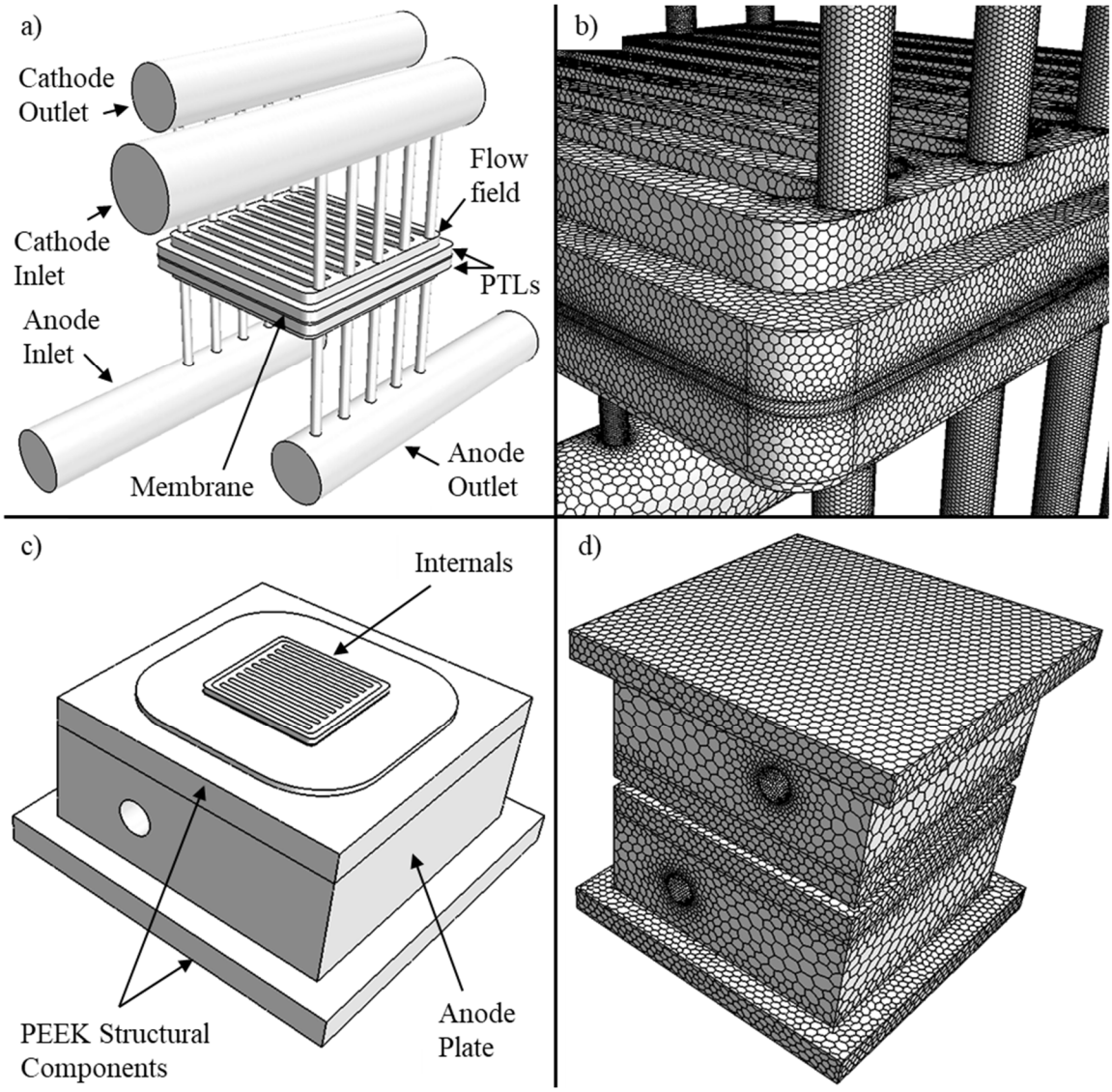

Figure 3.2: Proton exchange membrane electrolysis geometry and mesh. a) Geometry of the manifolds, flow field channels, porous transport layers, and membrane of a PEMWE cell. b) Magnified image of the volume mesh at the boundaries of the internal components of the cell. c) Illustration of the anodic CC and PEEK structural components with the anodic internals positioned inside. d) The finite volume mesh at the outer boundaries of the entire geometry.

to 3,643,729. A mesh independence study was performed on a simulation in wet anode/wet cathode mode with 80 mL min^{-1} water feed to each inlet at 2.0 V. The difference in current density between meshes with target surface sizes of half and double those of the original mesh was approximately 1.0% (J. Lopata, Z. Kang, et al. 2021b).

Boundary Conditions

The boundary conditions and their locations within the geometry are provided in Figure 3.3, which displays an along-channel cross-section of the entire PEMWE cell. Constant potentials were enforced at the terminals, with the cell potential specified at the anode and 0.0 V specified at the cathode. Constant velocities were set at the inlets while constant pressures were set at outlets. Liquid water only was said to enter the cell from the inlet, and this condition was specified at the outlets in the event of reverse flow at some of the faces of those boundaries. Newton's law of cooling was applied to every external boundary. Within the channels and PTLs, all wall boundaries were assumed to have no-slip (zero velocity) conditions. The species fluxes, boundary resistances, and heat generation at the anode and cathode boundaries are detailed in Equation 1.10 and Equations 3.1-19.

Numerical Methodology

Optimal solutions for this system were obtained using Siemens Simcenter Star-CCM + 15.02.009-R8, which utilizes the finite volume method. An overview of the general computational sequence is provided in Table 3.1. The initial condition for $\boldsymbol{R}_{tk}$ was set using Equations 3.1-19. Anodic components were initially set equal to the cell potential while other components, including the membrane, were initially set to 0 V. The convergence scheme began with obtaining a solution for the potential, then activating the other solvers. First, current was calculated using the initial condition for potential, then the potential

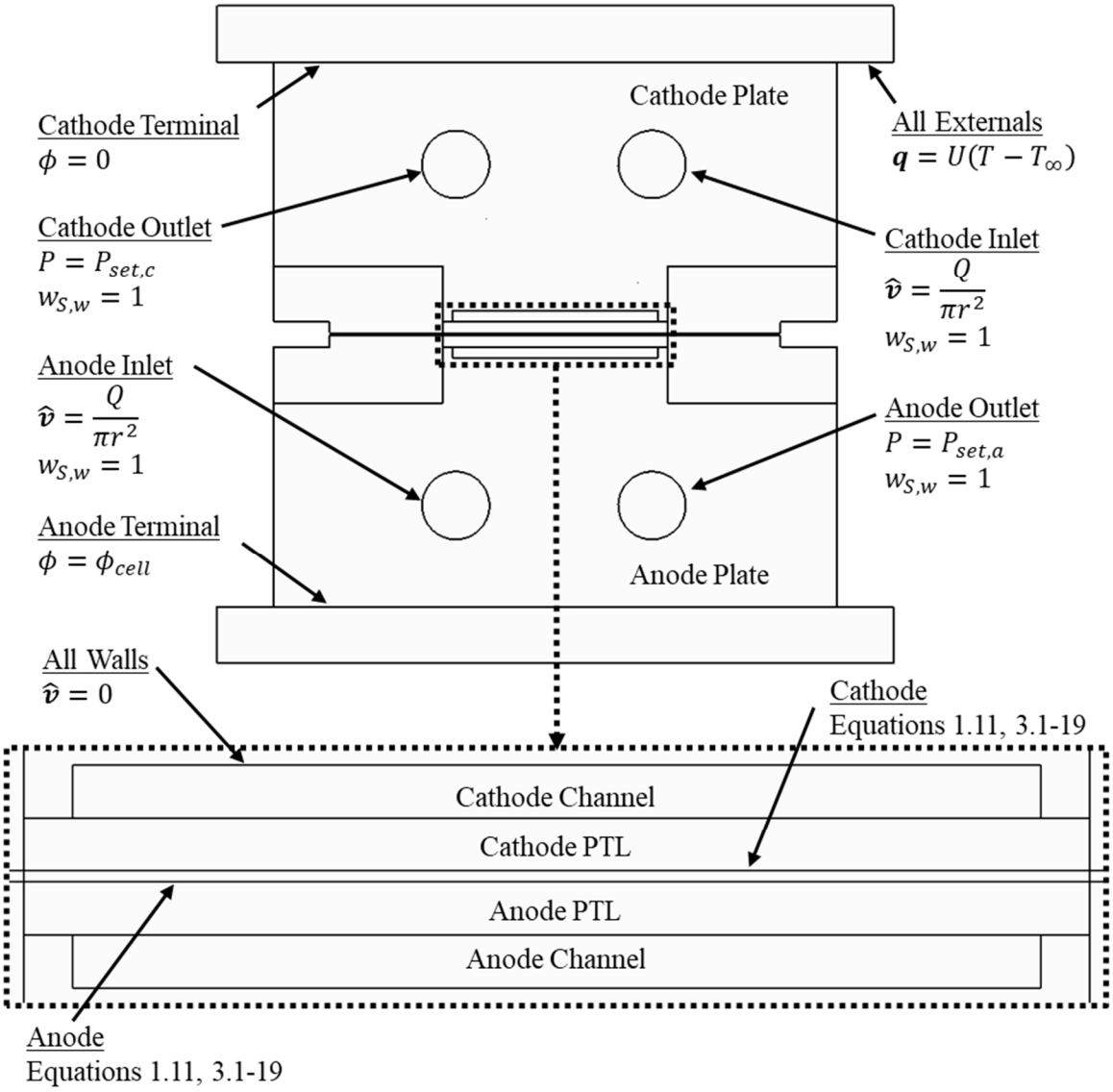

Figure 3.3: Plane section of the PEMWE cell geometry with boundary conditions.

Table 3.1: PEMWE Model Solver Sequence

Iteration	Event
0	Potential solver activated with a constant $R_{tk,a}$
5	$R_{tk,a}$ determined iteratively
20	Flow solver activated
300	Species solver ramp started
400	Species solver ramp finished
500	Gas diffusivities multiplied by $(1 - s)^b$, volumetric phase change started
600	Compressible flow activated, densities of species become functions of temperature and/or pressure
750	Energy solver ramp started
850	Energy solver ramp finished

solver was allowed to converge on its own. The final URFs for the potential, velocity, pressure, species, fluid energy, and solid energy solvers were set to 1.0, 0.5, 0.1, 0.25, 0.9, and 0.99, respectively. Upon activating the flow, species, and energy solvers, flow solver URFs were set to their final values while species and energy URFs were ramped from 0. After the ramp, the gas diffusion limitation due to the presence of liquid, then flow compressibility, were activated sequentially. Convergence was said to be achieved once the rate of change in either the gas-phase or liquid-phase average current density was less than 10 A m^{-2} per 1000 iterations and slowing, which occurred long after the residuals stopped decreasing (Lopata, Weidner, et al. 2022).

Most often, once a satisfactory solution for a prior set of conditions had been reached, the result was used as the initial condition for another simulation. This method performed well in most cases, such as reducing the feed rate to the anode or changing the temperature setpoint, but potential changes occasionally led to divergence, so the full starting sequence was employed when running simulations with new cell potentials (Lopata, Weidner, et al. 2022).

Experimental Validation of the PEMWE Model

This section describes the fabrication methods and measurement techniques used to obtain data with which to compare the model during development. The model, which contained many unknown parameters, was not predictive, per se. Via matching the modeled cell performance and temperature to experimental data, the aim was to explore variables that are extremely difficult to measure and use them to gain an understanding of the process and how it can be tuned to the advantage of engineers that operate and study these devices.

Porous Transport Layer Preparation and Characterization.

Titanium porous sintered plates (Edgetech Industries, LLC) were cleaned using an ultrasonic bath. The plates were immersed for 15 min each in acetone, then 2-propanol, and finally deionized (DI) water. After sonication, they were lightly etched by immersing them in 3 M HCl, which was temperature-controlled by a 94 ºC water bath for 30 min (Ye, et al. 2010). The samples were rinsed thoroughly with DI water before drying them at 80 ºC in an oven at ambient pressure for 16 h. They were subsequently sputtered with iridium metal on both sides to improve electrical contact and mitigate oxidation of the underlying titanium that would otherwise cause slowly increasing resistance during operation (Liu, et al. 2018). Iridium sputter coating was conducted in a custom-built sputtering system described elsewhere (Steiner, et al. 2019). The loading of the iridium was controlled to 44 nm by sputtering each sample side for 20 min. It was assumed that this procedure had a negligible impact on OER kinetics because the surface area of the iridium coating is much smaller than that of the IrO_2 powder in the CL. Past studies have attributed improved performance of iridium-coated PTLs to decreased contact resistance rather than an increase in active sites (Liu, et al. 2018). The average PTL porosity was calculated with the density of commercially pure titanium (4.506 g cm^{-3}) after determining the sample weight and estimated volume from its dimensions. Permeability measurements were conducted on the PTL materials by passing nitrogen gas through a circular cross section of each PTL using Gylon gaskets and flanged tubing to enclose them. Nitrogen was introduced at different flow rates set by a flow controller and the pressure drop from inlet to outlet was measured with an Omega HHP350 differential pressure gauge. The temperature in K at the outlet was measured for calculating the viscosity of the nitrogen using Sutherland’s formula for

nitrogen viscosity (Chemical Rubber Company (CRC) 1984, Crane Company 1988):

$$\mu_{N_2} = 0.0172 \frac{411.55}{T + 111} \left(\frac{T}{300.55} \right)^{1.5} \tag{3.20}$$

Intrinsic permeabilities (15% error due to variability in gaskets) were calculated by fitting Darcy's Law to experimental pressure drop versus flow rate through a known cross-sectional area and length (J. Lopata, et al. 2020).

Membrane-Electrode Assembly Fabrication.

The ink used to fabricate the cathode CL consisted of a mixture of Pt/C powder (Tanaka Kikinzoku Kogyo TEC10E50E, 46.7 wt% Pt), Nafion® ionomer dispersion (Ion Power, D2020, 1000EW), DI water (18.2 MΩ cm) and HPLC-grade n-propanol (OmniSolv®) using a Nafion®/carbon weight ratio (I/C ratio) of 0.45 and a water:alcohol volume ratio of 1.3. The ink was treated by tip sonication (Branson) for 30 s, followed by bath sonication (Branson) for 30 min immediately before the spray deposition. For the anode catalyst ink, IrO_2 (Premion, 99.99% purity), D2020 ionomer dispersion, DI water and n-propanol were mixed with a Nafion®:catalyst weight ratio of 0.24 and a water:alcohol volume ratio of 1.3. Following the tip sonication for 30 s, the dispersion was bath sonicated for at least 1 hour. All the sonication treatments were performed in an ice bath environment to avoid heating and sintering of the catalyst nanoparticles. The CCMs were fabricated by ultrasonic spray coating anode and cathode catalyst inks each onto one side of Nafion® 117 (Chemours®) membranes using a Sono-tek ExactaCoat System with a 25 kHz accumist nozzle. Before spraying, the membranes were fixated on a heated vacuum plate at 80 °C. The catalyst ink was then sprayed on the membrane at a pump rate of 0.3 mL min^{-1} for high catalyst loading and 0.1 mL min^{-1} for low catalyst loading. 25 cm^2 areas were sprayed so that each area could be cut into four identical pieces to be used in a cell

with a 4 cm^2 active area. A new CCM was used whenever the cell was reassembled (J. Lopata, et al. 2020).

Catalyst loadings of the anode and cathode were determined by X-ray fluorescence spectroscopy (Fisher XDV-SDD). At least five points were measured for each sample. The anode catalyst loading was approximately 0.595 ± 0.022 mg Ir cm^{-2}. The error reported with these values are two times the standard deviation. The cathode loading amount was 0.382 ± 0.018 mg Pt cm^{-2} (J. Lopata, et al. 2020).

Cell Hardware and Test Station.

A schematic of the experimental setup and images of the hardware are displayed in Figure 3.4. A 4 cm^2 electrolysis cell, provided by Fraunhofer ISE®, was used that featured parallel (anode/cathode) gold-coated titanium flow fields. For operation, the cell hardware was housed inside an oven. The DI water that was fed to the cell during low-feed-rate experiments was heated by running it through a long coil of tubing placed inside the same oven. Three T-type thermocouples (TC) were used to conduct cell temperature measurements. One TC was placed in the outlet tubing to record the anode outlet temperature, which was used for calculations of equilibrium potentials and Tafel slopes. Another TC was inserted into the anode plate at the end of the channels and used as the outlet temperature when the flow rate was less than 1.25 mL min^{-1} cm^{-2}. A third TC recorded the temperature of the water feed at the cell inlet so that the temperature change across the cell could be recorded and compared between experiments. All electrochemical experiments were conducted with a Gamry Reference 3000 and 30K booster. For cell conditioning and polarization experiments at 20 mL min^{-1} cm^{-2} , the cell was operated in a wet/wet configuration with 80 mL min^{-1} of DI water fed to each the anode and cathode.

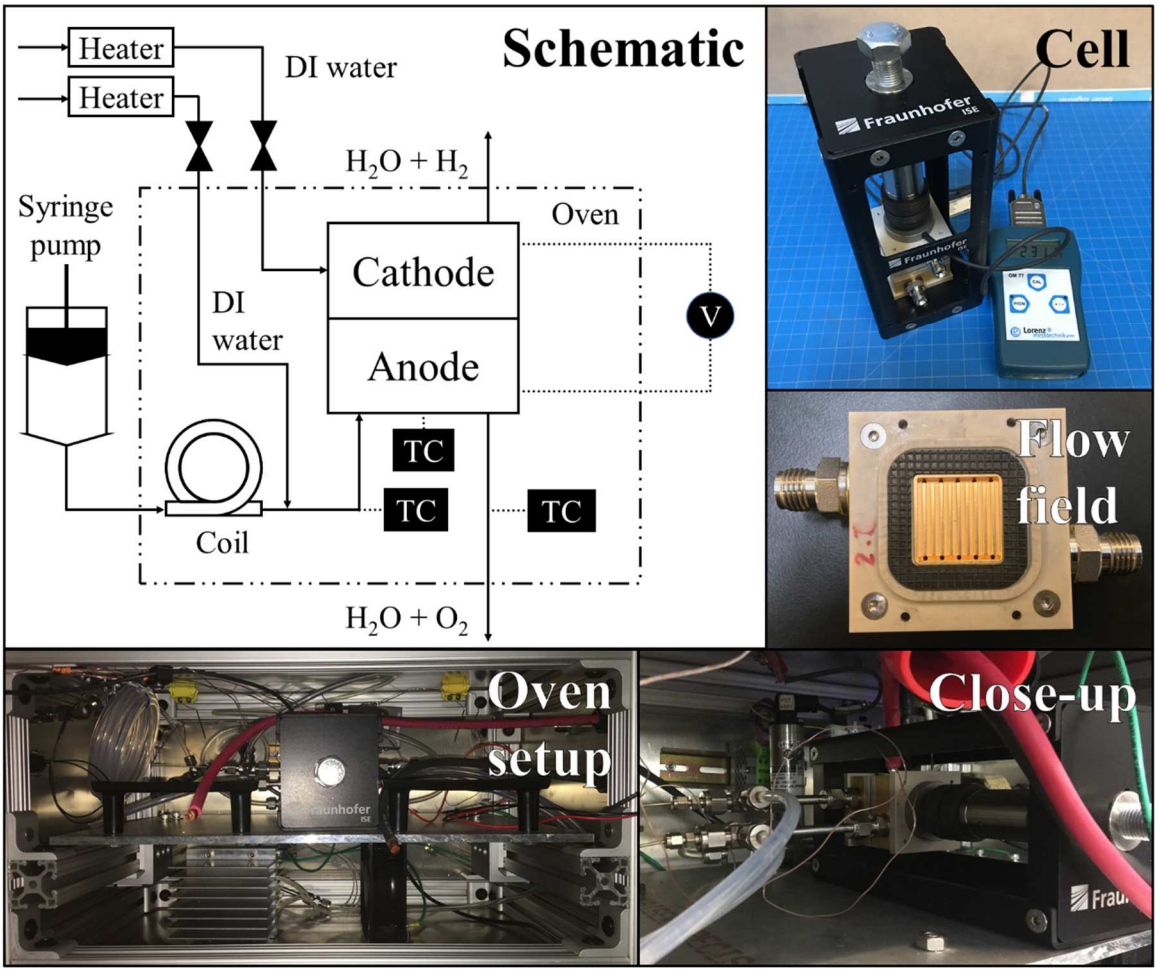

Figure 3.4: Schematic and photographs of the PEMWE experimental setup (J. Lopata, et al. 2020).

For flow sensitivity experiments, the cell was operated in a wet/dry configuration controlling the feed rate to the anode using a dual-syringe infusion syringe pump (KDS 200, KDScientific, Inc.) with two 60 mL syringes. In this case, no water was fed to the cathode. The backpressure was controlled to 1 atm absolute at both outlets, which represents sea-level ambient pressure and was necessary due to NREL's high elevation. The cell temperature was controlled by heating the inlet water and the oven to the same temperature (J. Lopata, et al. 2020).

Cell Assembly and Conditioning.

For cell assembly, the CCMs were placed between the PTL and the sandwich was sealed using two Freudenberg® IceCube 60 FC-FKM 200 gaskets. The cell was initially clamped with a force of 3.5 kN using a force sensor for precise control. After the cell was connected and the water flow initiated, the cell was heated to 40 °C and the compression increased to 4.0 kN.

For conditioning, the water temperature at the inlet was set to 80 °C and the oven temperature was set to 65 °C. The cell was held at 1.4 V for 30 min, 1.5 V for 30 min, then 1.7 V for 2 h. During these 3 hours, the cell current plateaued and remained stable, which indicated completion of the conditioning process (J. Lopata, et al. 2020).

Electrochemical Characterization.

High-flow-rate experiments were conducted in wet/wet mode with 20 mL min^{-1} cm^{-2} DI water fed to each the anode and cathode, i.e. total anode/cathode flows of 80/80 mL min^{-1}. The cell was held at 2.0 V for 30 min prior to stepping the voltage down from 2.0 to 1.4 V in 18 steps of varying size: first 2.0 to 1.9 V, then 1.9 to 1.7 V in 0.05 V increments, 1.7 to 1.5 V in 0.025 V increments, and finally 1.5 to 1.4 V in 0.02 V increments. Each

potentiostatic segment was held for 5 min and the final 15 s from each step were averaged to construct the polarization curves. The sampling rate was 1 point s^{-1}. Potentiostatic EIS was taken every 0.1 V at the end of the corresponding polarization segment. No rest time was allotted between steps to maintain the temperature, CL gas phase composition, and the extent of catalyst surface oxidation at steady state.

Prior to operation with low water feed rates, the water lines inside the oven were flushed with heated DI water until the temperature of the water in the cell and the oven temperature were within 0.5 °C of the target cell temperature. A dual syringe pump with two 60 mL syringes, located outside the oven (see Figure 3.4), was used to supply the DI water at low flow rates. Both syringes were filled by closing the anode outlet line and redirecting the heated water into the syringes. Care was taken to prevent bubble development in the line. After filling, the flow was reversed and redirected from the syringe pump into the anode compartment of the cell. The syringe pump was set to the desired flow rate and the applied voltage was set to 1.9 or 2.0 V until the current reached a steady state. At 2.5 mL min^{-1} cm^{-2}, this equilibration time was 500 s, and at 1.875 mL min^{-1} cm^{-2} and 1.25 mL min^{-1} cm^{-2}, it was 750 and 1000 s, respectively. A period of 1800 s was necessary for the current to reach steady state at all other flow rates. At flow rates less than 0.05 mL min^{-1} cm^{-2}, the cell exhibited sporadic, oscillatory behavior. To compensate for this, the current was averaged over 30 min periods. After each potentiostatic hold period, an EIS experiment was conducted at the same potential as the potentiostatic hold.

Potentiostatic EIS experiments were conducted concurrently with polarization experiments, with measurements taken at the end of each respective potentiostatic hold

period. A frequency range of 10 kHz to 10 mHz and a perturbation amplitude of 10 mV were chosen, recording ten points per decade (J. Lopata, et al. 2020).

Discussion

Mass Transport Overpotential and Bubble Coverage.

The operating conditions summarized in Table 3.2 were used to compare simulation results with experimental data. In Figure 3.5, the simulation results are compared to experimental data at 35 °C (w/w-35) and 55 °C (w/w-55). The total potential from simulations is subdivided into different portions: the equilibrium potential, resistance overpotential, activation overpotential, and the mass transport overpotential. The reasonable agreement between computational and experimental results among temperatures indicated that the study could proceed with the selected parameters. Interestingly, the mass transport overpotential appeared to be nearly constant, increasing very slightly with increasing cell potential. At high potential, mass transport was responsible for a loss of about 500 A m^{-2} of current or more, which was roughly 4% of the total current. Figure 3.6 records dimensionless variables of interest and their relationships with current density and temperature under w/w-35 and w/w-55 operating conditions. First to note is that the performance loss due to mass transport is not as severe as one might expect based on the value of the bubble coverage in Figure 3.6. For example, a bubble coverage of 0.2 would lead to a 20% reduction in current, were it not for the low equilibrium potential of the A-OER(G) compared to the A-OER(L). Kinetically, the A-OER(G) is not very favorable, but higher thermodynamic favorability compensates for this somewhat. The bubble coverage in Figure 3.6 increases with increasing current density and the relative humidity decreases, both due to greater gas evolution rates. However, the gas-

Table 3.2: PEMWE Model Operating Conditions

Temperature (°C)	Feed configuration	Feed rate per ½ cell (mL min^{-1})	Notation
35	wet/wet	80	w/w-35
55	wet/wet	80	w/w-55
	wet/dry	80	w/d-55A
		10	w/d-55B
		5.0	w/d-55C
		2.4	w/d-55D
		0.82	w/d-55E

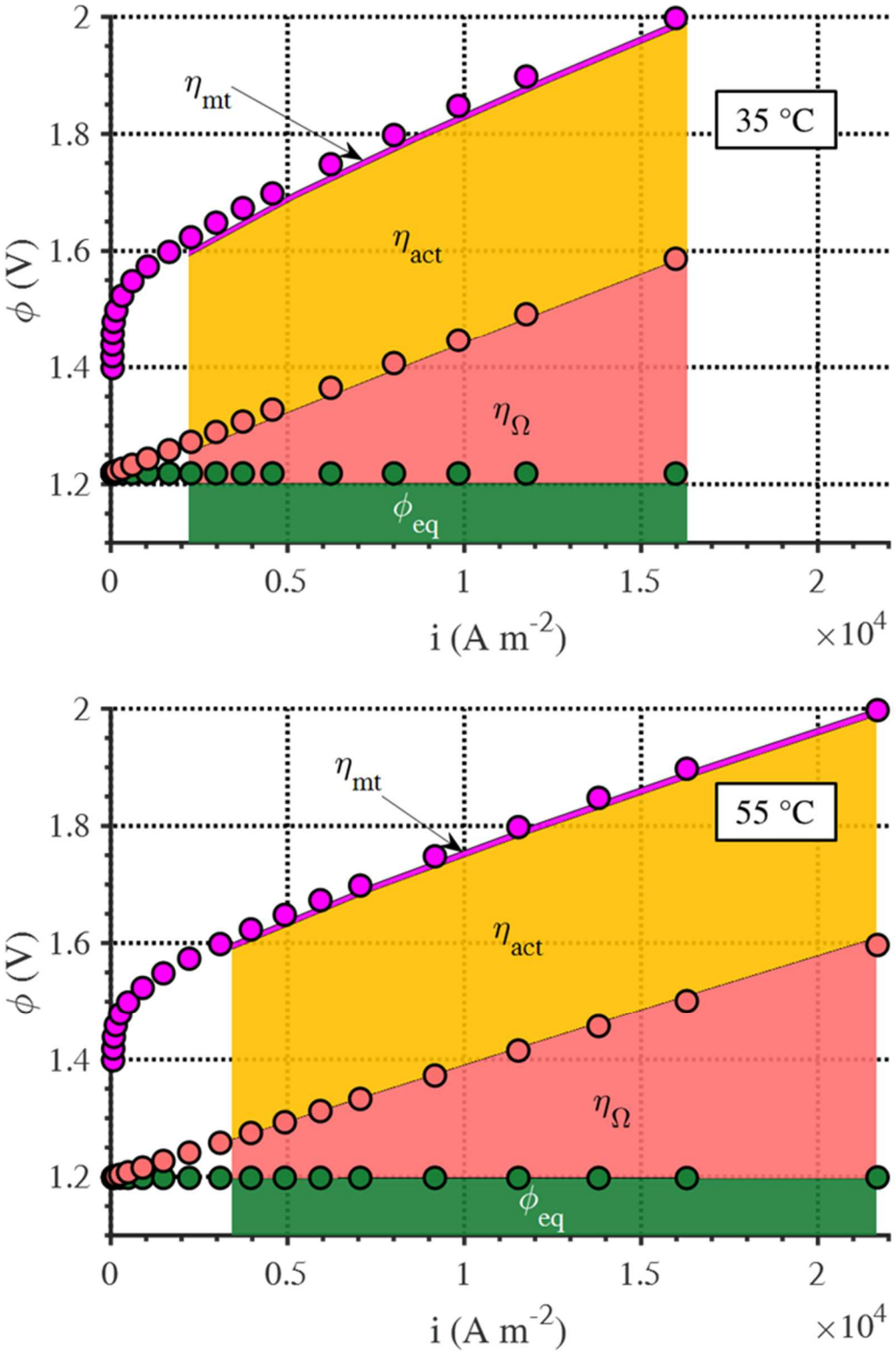

Figure 3.5: Decomposed polarization curves from simulations and experiments at 35 and 55 °C with 80 mL min^{-1} liquid water feed to each electrode in wet/wet operation (Lopata, Weidner, et al. 2022).

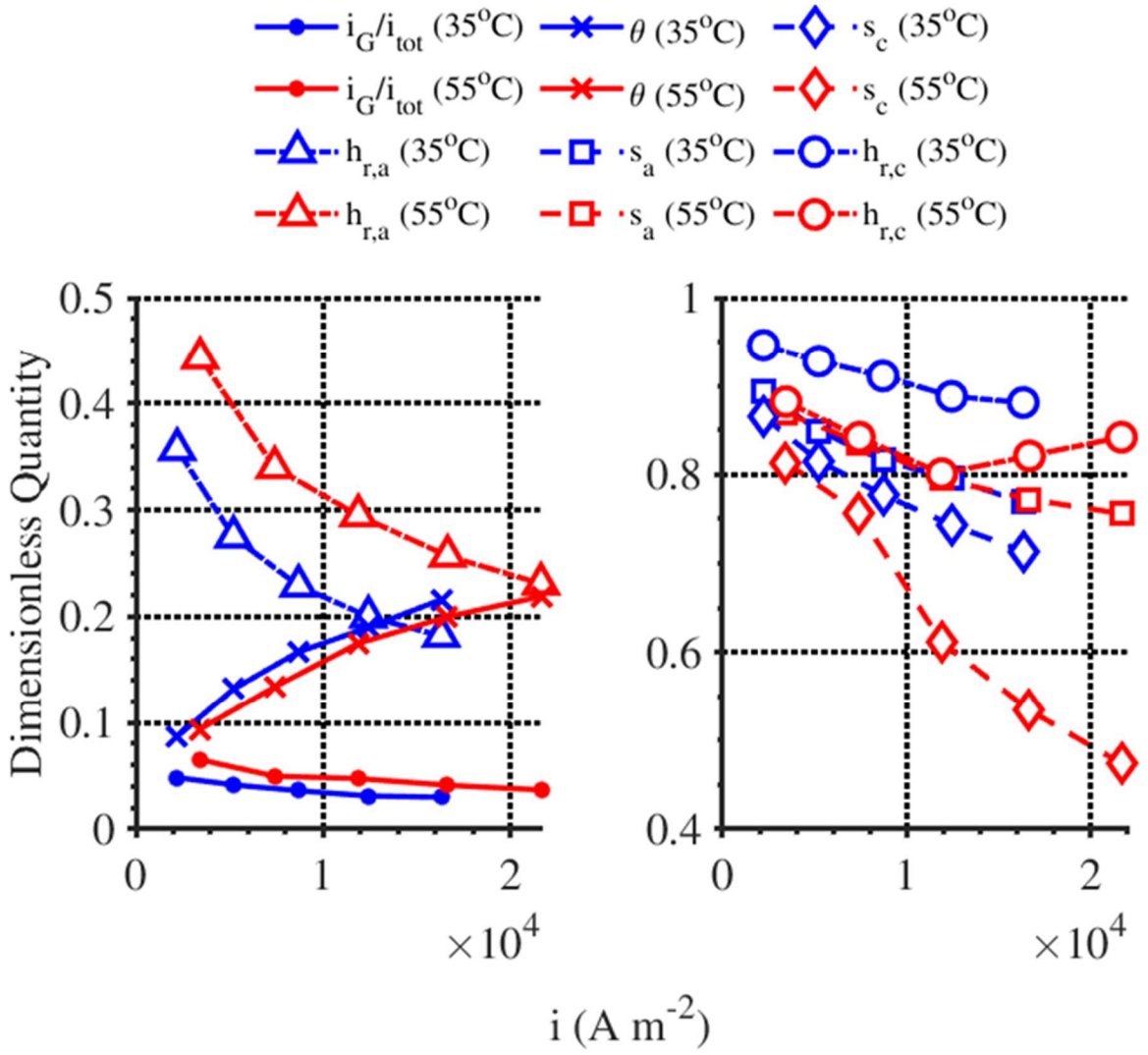

Figure 3.6: Dimensionless variables of interest versus current density at 35 and 55 °C with 80 mL min^{-1} liquid water feed to each electrode in wet/wet operation. Gas-phase current contribution (i_G/i_{tot}), anodic and cathodic relative humidity ($h_{r,a}$ and $h_{r,c}$), anodic and cathodic liquid saturation (s_a and s_c), and bubble coverage (θ) are plotted (Lopata, Weidner, et al. 2022).

phase contribution is still significant because the surface overpotential remains higher than that of the liquid phase. Note that the overall mass transport overpotential is quite small because it is a current-weighted average of the liquid and gas phases. For w/w-55, the liquid mass transport overpotential is 0.0073 V while the gas mass transport overpotential is more than 100 times greater at 0.1021 V. One can infer from inspection of Figure 1.3c that cell performance could improve if the anodic relative humidity were higher, which would be the result of somehow facilitating higher evaporation rates (Lopata, Weidner, et al. 2022).

Effects of Polarization on Current, Temperature, and Composition.

Current density distributions were highly uniform at 80 mL min^{-1}. In Figure 3.7, the current distributions are shown with similar scale ranges, but with changing values, so that the effect of polarization on land and channel effects are observable. Given the likely reason behind higher current density in the land areas – shorter distances between the CC and membrane – this increase in land-channel non-uniformity with increasing potential is most likely due to the magnitude of the current density itself. Anode temperature distributions become less uniform along the channel with increasing potential, because higher potential and current density results in more heat generation, which increases the temperature along the channel as the fluid flows and absorbs this heat.

There exist areas in the current distributions, not confined to land or channel areas, where the current is relatively high compared to elsewhere. Figure 3.8 shows that this is due to the availability of liquid water in those locations. While the relative humidity is somewhat high at low potentials because there is less water vapor consumption, it decreases significantly with increasing potential as the rate of water vapor consumption increases. Therefore, at high cell potentials under these operating conditions, the A-

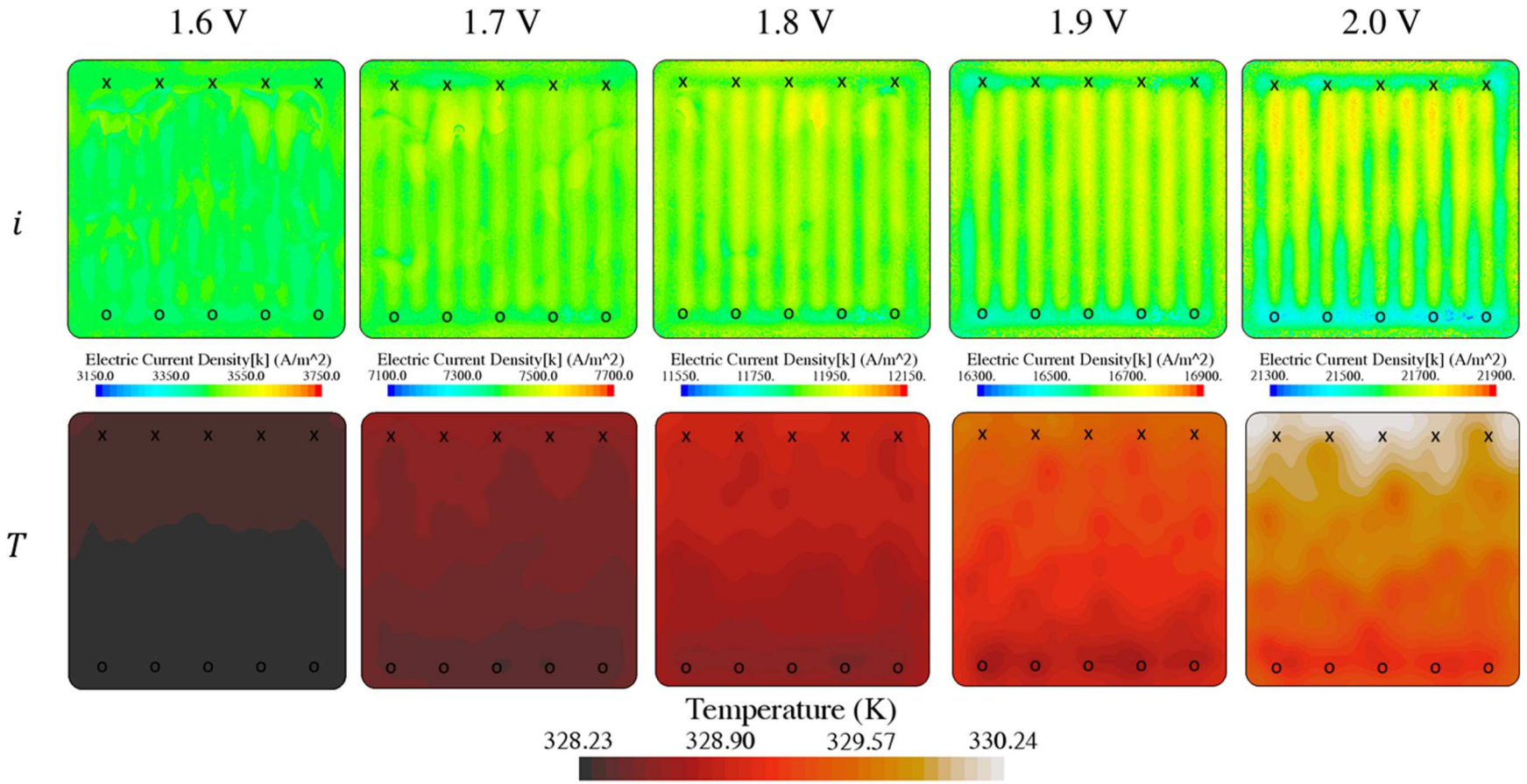

Figure 3.7: Anodic current density and temperature distributions versus cell potential at 55 °C with 80 mL min^{-1} liquid water feed to each electrode in wet/wet operation. “o” denotes an inlet and “x” denotes an outlet (Lopata, Weidner, et al. 2022).

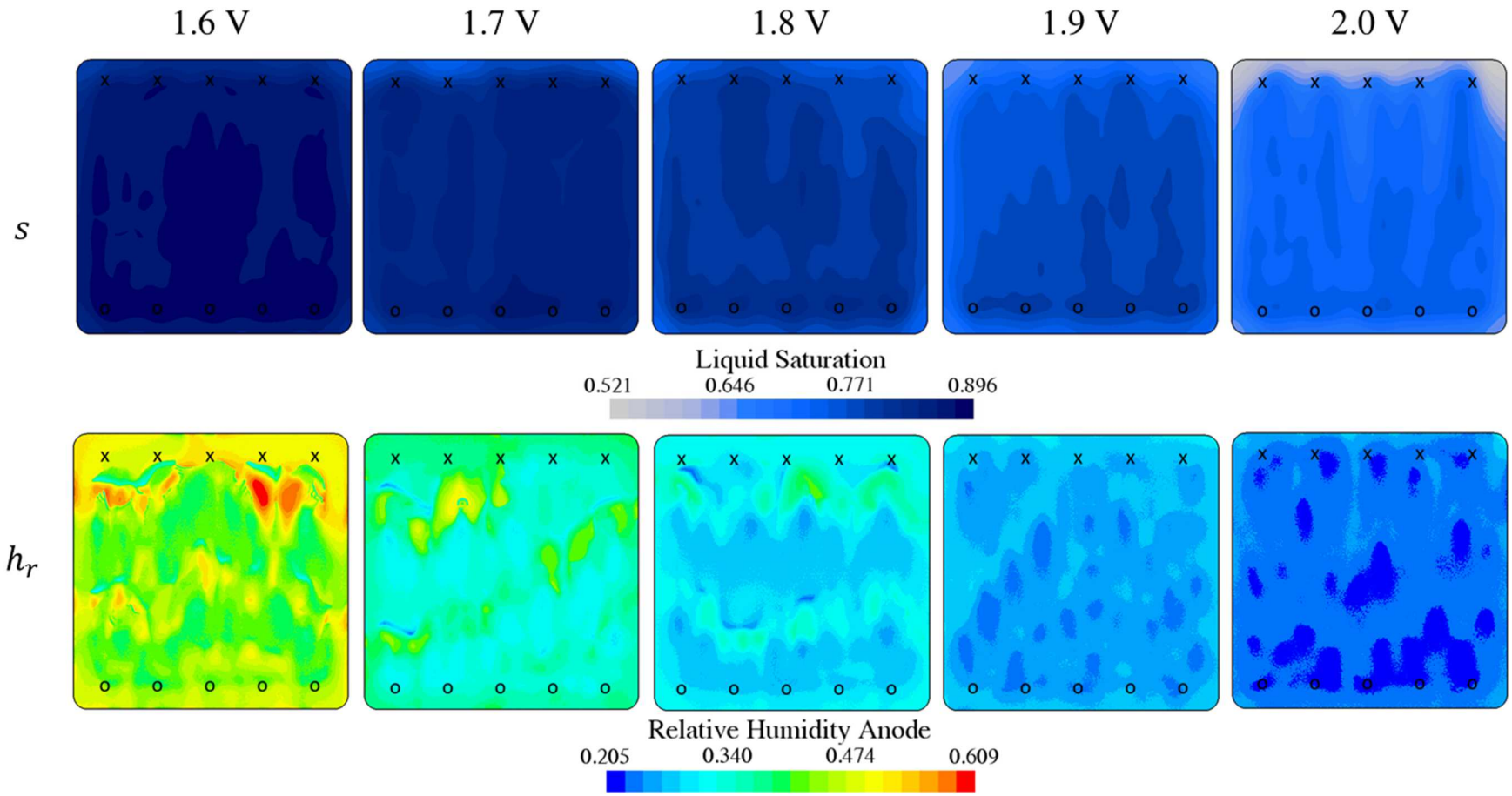

Figure 3.8: Anodic liquid saturation and relative humidity distributions versus cell potential at 55 °C with 80 mL min^{-1} liquid water feed to each electrode in wet/wet operation. “o” denotes an inlet and “x” denotes an outlet (Lopata, Weidner, et al. 2022).

OER(G) is not very favorable. Because the A-OER(L) dominates in this case, reduced liquid saturation leads to reduced current. Note that liquid saturation distributions contain some level of uncertainty, as evidenced by differences in liquid saturation distributions between 1.8 and 2.0 V. Even when seeking a steady-state solution, there is some instability, especially at high feed rates. Liquid water locally penetrates the PTL whenever the channel pressure is sufficiently high or capillary forces are strong, and the gas phase resists the movement of liquid toward the anode, creating a liquid/gas front within the PTL that travels along the channel. This does not result in very large changes in liquid saturation or current density. However, the relative humidity is quite sensitive to the liquid saturation. Relative humidity at the anode is low when the liquid saturation increases, usually in locations where water is forced into the PTL, possibly due to displacement from the presence of gas in the channels downstream. When a liquid/gas front forms, the evaporation rate increases and the downstream relative humidity is high. The temperature distribution at 2.0 V in Figure 3.7 shows more evidence of increased evaporation rate. Just downstream of the locations where liquid saturation is relatively high, relative humidity decreases. Liquid saturation is sharply reduced, and just downstream of this, relative humidity increases while the temperature decreases, indicating evaporative cooling. The behavior of relative humidity is more obvious at low potentials. Near the inlet, water moves into the PTL, increasing the liquid saturation and reducing relative humidity. Farther downstream, relative humidity increases again (Lopata, Weidner, et al. 2022).

Effect of Feed Rate on Cell Performance.

The change in cell performance and gas-phase current contribution with respect to the anode inlet feed rate is provided in Figure 3.9 under w/d-55 operating conditions.

Overall cell performance increases with decreasing stoichiometric feed rate, which is primarily due to reduced convection leading to an increase in temperature. However, evaporation itself explains some of the increase in current even in the absence of a temperature rise, according to the isothermal simulation data. At stoichiometric feed rates below 120, the current density is higher than at 2100, even in a hypothetical isothermal case. This implies that it may be economical to operate cells at lower feed rates due to the contribution of the A-OER(G) to the overall current density. This would allow the use of smaller pumps, reservoirs, and purification systems, which reduces the initial cost of a system, the amount of floor space required for operation, and the variable costs of keeping the water lines at the desired temperature. With sufficient cell insulation, the feed temperatures can be significantly lower, 6-8 °C lower according to the model, which reduces the amount of heat loss in the peripheral components. According to the results thus far, it is plausible that at certain feed rates, a reduction in PTL permeability can benefit performance by limiting the liquid saturation at the anode and facilitating higher evaporation rates. A reduced liquid water feed rate may be beneficial as long as there is enough supplied to sustain the reaction, electroosmotic drag, and evaporation.

It is important to mention the contribution of electroosmotic drag to heating. Despite the evaporation of water that occurred at the anode, evaporative cooling was not detrimentally severe. The model assumed that the water within the membrane was in a condensed phase with a formation enthalpy equal to that of liquid water. Therefore, when water vapor entered the membrane, heat was generated, compensating for the heat lost due to evaporation. Note that the electroosmotic drag coefficient in this model was assumed not to vary with temperature or water activity.

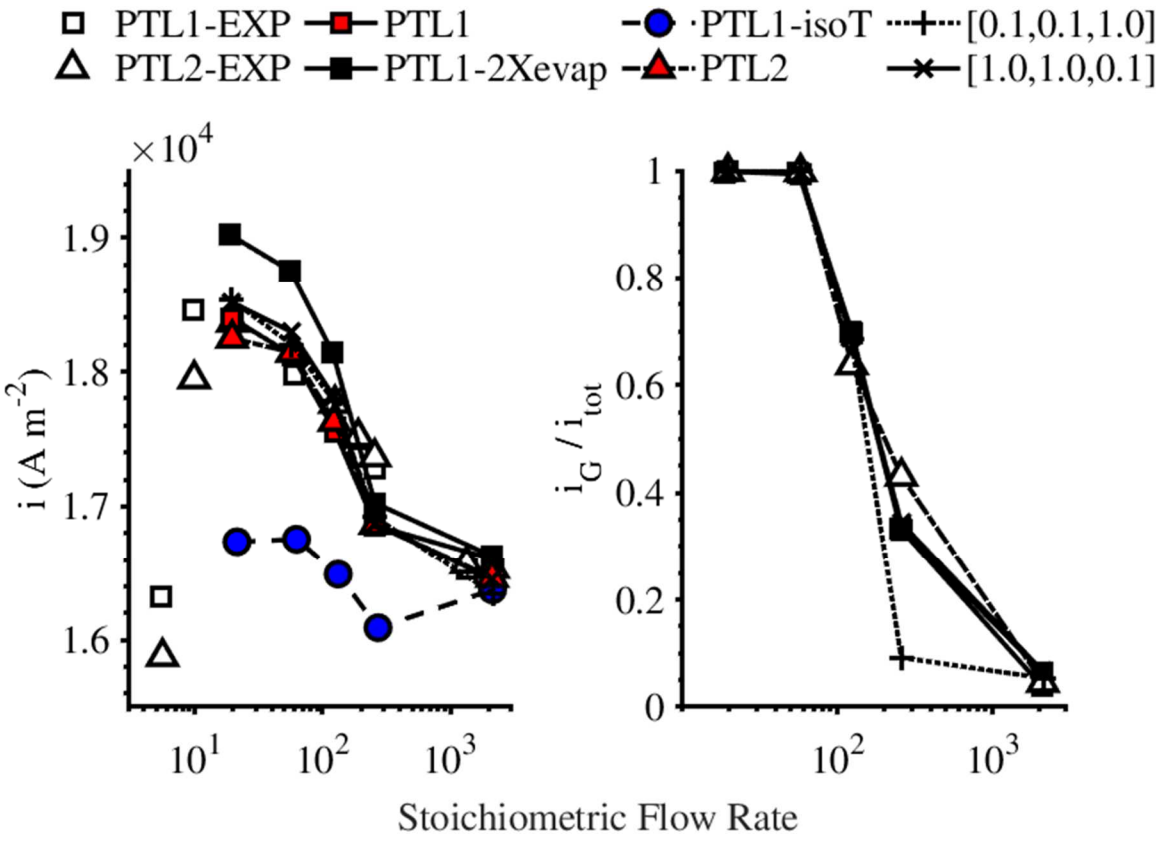

Figure 3.9: The variation in overall current density and dimensionless gas-phase current contribution with changes in the anode feed rate. Feed rate is expressed on the basis of the theoretical feed rate required to sustain the reaction. PTL properties were tuned in order to determine their effects. The PTL1-2Xevap data series explores the effect of doubling the interfacial area between the liquid and gas phases in PTL1. [0.1,0.1,1.0] and [1.0,1.0,0.1] are orthotropic permeability factors with the first and second values representing the x- and y-, or in-plane, direction and the third value representing the z- or through-plane direction (Lopata, Weidner, et al. 2022).

The current distributions for w/d-55 cell operation at high anode feed rates are shown at the top of Figure 3.10. The color bar scale is 1,700 A m^{-2} for every distribution to illustrate the degree of uniformity. At 80 mL min^{-1}, the current density is relatively low and uniform from inlet to outlet. There is once again a mild flow field effect that raises the current density in the land areas due to the shorter electron pathway that exists in those areas. The slight increase in current density from inlet to outlet was due to both a pressure drop and temperature rise from inlet to outlet, the latter of which was induced by reactive and ohmic heating. The high 80 mL min^{-1} feed rate (w/d-55A) led to uniform liquid saturation and current density. Some cool spots are visible in the temperature distributions where liquid water penetrated through the porous medium toward the electrode. This appeared to occur mostly upstream of a gas plume, which displaces water in the channels and forces it to enter the PTL. Liquid saturation was especially high in the locations of the injection manifolds, which were oriented perpendicularly to the anode. Because the liquid saturation was relatively high, the relative humidity was low because the liquid/gas interfacial area is low at high liquid saturation. In multiple locations, the relative humidity was low where liquid water entered the PTL moving toward the anode, and it increased sharply downstream where more gas was present. Upon reducing the flow rate to 10 mL min^{-1} (w/d-55B), current density increased, mostly along the sides of the flow field near the outlet. This was due to low liquid saturation and thus higher relative humidity in these areas and resulted in higher local temperatures. Moderate current densities existed where the liquid saturation was high, and the lowest current density was between these two regions. A reduction in liquid saturation without a beneficial increase in relative humidity was harmful to performance, even with a mild temperature increase. Liquid water tended

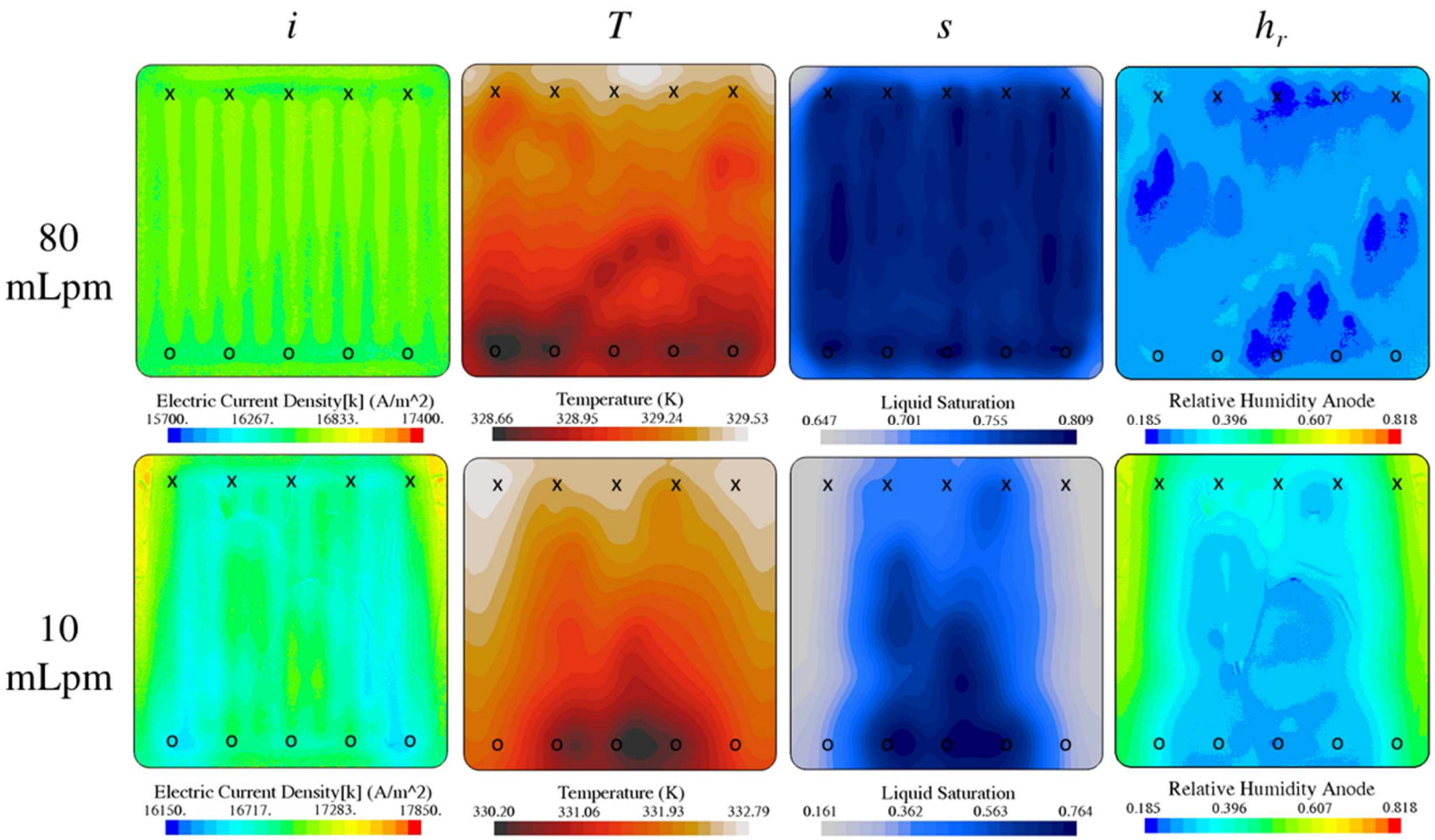

Figure 3.10: Anodic current density, temperature, liquid saturation, and relative humidity distributions for 1.9 V operation at a setpoint of 55 °C with high feed rates to the anode under wet/dry operation. These simulations used the properties of PTL1. “o” denotes an inlet and “x” denotes an outlet. Current distributions have color scales of similar size while relative humidity distributions have equal color scales (Lopata, Weidner, et al. 2022).

to travel through the middle of the flow field rather than along the edges. This will be revisited in a later section. In Figure 3.11, at a further reduced feed rate of 5 mL min^{-1}, a transition occurs as the gas phase becomes more prominent near the end of the channel. At this point, the gas phase becomes more prominent near the end of the channel, resulting in higher evaporation rates, relative humidity, temperature, and thereby current density. The resulting gas plume seems to force liquid water to move from the flow field to the PTL at the beginning and middle of the channel, forming a sharp front between the two regimes. The relative humidity is highest just downstream of this front because of the low liquid saturation, while further downstream the relative humidity decreases due to water vapor consumption, electroosmotic drag, and extremely low liquid saturations. One notable effect of the front is the low local temperature. At the front, significant evaporation occurs but without a great increase in current because much of the water vapor formed reacts downstream. The current density is highest at the outlet, where the temperature is also high. Due to improved thermodynamic and kinetic favorability at higher temperature, which is caused by high current, the temperature rise compounds to some degree, hence the sharp temperature rise from the middle to the end of the channel. At lower feed rates, there is much less liquid water penetration, so it is very localized near the second injection point at the inlet to the flow field. Essentially, the gas-phase region described previously expands to cover most of the anode area and the front shrinks. At 0.82 mL min^{-1}, the current increases and becomes more uniform because the liquid saturation is very low at every location. At extremely low liquid saturations, the interfacial area decreases, so further reducing the flow rate may no longer be beneficial to performance. Note that the highest current density at this feed rate occurs in the middle of the cell rather than at the outlet.

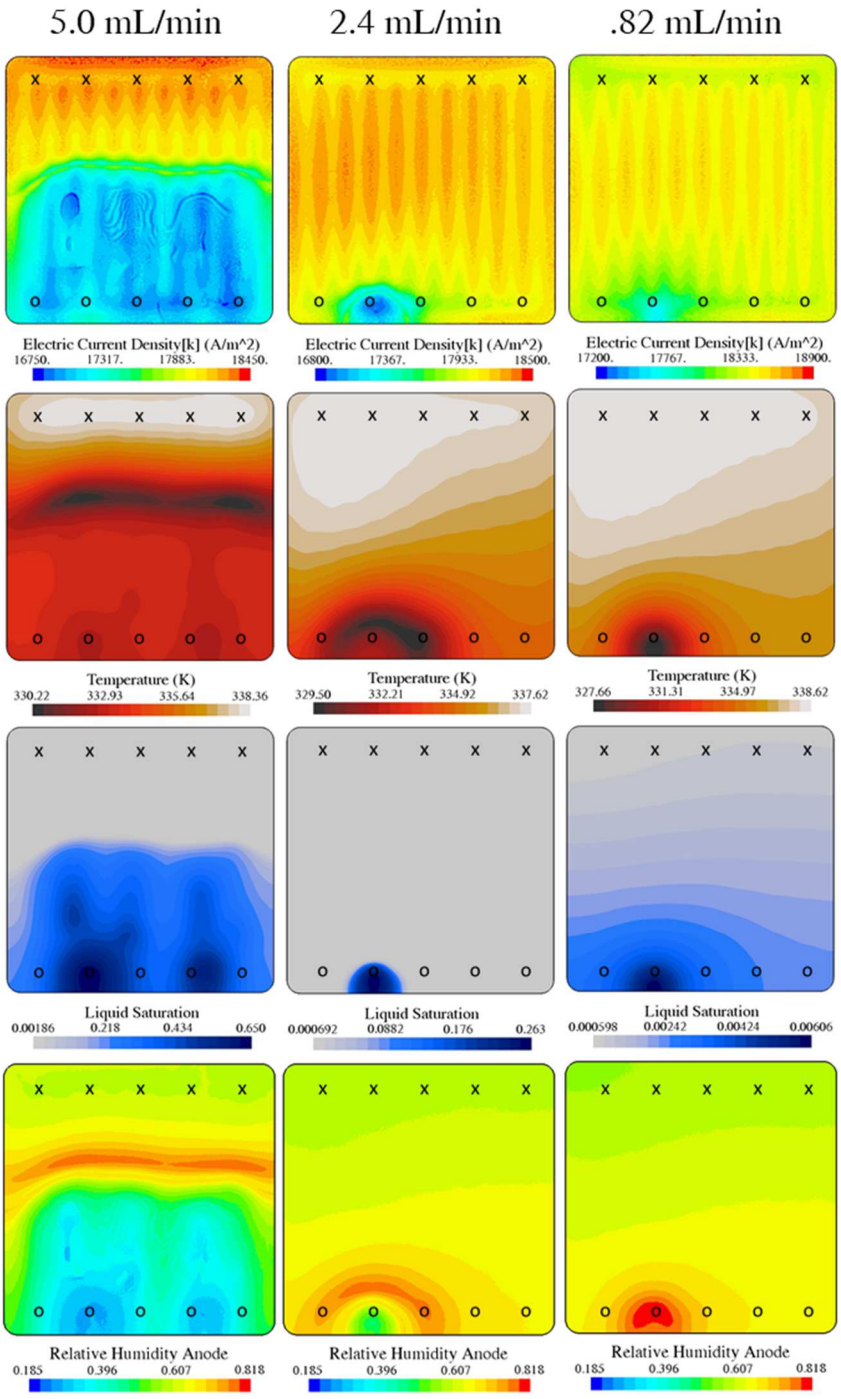

Figure 3.11: Anodic current density, temperature, liquid saturation, and relative humidity distributions for 1.9 V operation at a setpoint of 55 °C with low feed rates to the anode under wet/dry operation. These simulations used the properties of PTL1. “o” denotes an inlet and “x” denotes an outlet. Current distributions have color scales of similar size while relative humidity distributions have equal color scales (Lopata, Weidner, et al. 2022).

Figure 3.12 clarifies what happens at 5 mL min^{-1} (w/d-55C) at the beginning and end of the flow field channels using the dimensionless gas-phase contribution and the A-OER(G) favorability. Near the inlet, the A-OER(L) dominates as indicated by the low gas-phase contribution and low favorability, but it soon diminishes as fluid flows along the channels. As more oxygen gas forms, higher evaporation rates lead to the A-OER(G) dominating near the outlet. The favorability distribution shows more detail near the outlet, where the A-OER(G) is significantly more favorable than the A-OER(L) immediately downstream of the liquid/gas front, but becomes less favorable along the channel as both liquid water and water vapor are somewhat depleted (Lopata, Weidner, et al. 2022).

Considerations for Flow Field and Manifold Geometry.

The distributions in Figure 3.11 indicate some asymmetry in the flow of liquid water through the flow field at low feed rates. This could be an effect of the inlet manifold pressure being slightly higher on the right side, causing liquid to favor the channels on the right. As liquid filled the rightward channels, the current density relative to that on the left side was reduced via decreasing A-OER(G) favorability. In turn, incoming water favored the rightward channels more. Evolved gas would thereby tend to fill the left-side channels, forcing water from those injection channels immediately into the PTL. This is not a problem, but this behavior was rather obvious and merited an explanation. Note that the use of a mixture model in the channels that neglected capillary action may have influenced or led to this observation. Anyhow, the flow distribution in the channels appears to become extremely sensitive at these very low feed rates.

Cross-channel and along-channel void fraction distributions are given for w/d-55 conditions at the injection sites, midsections, and ejection sites in Figure 3.13. Water tended

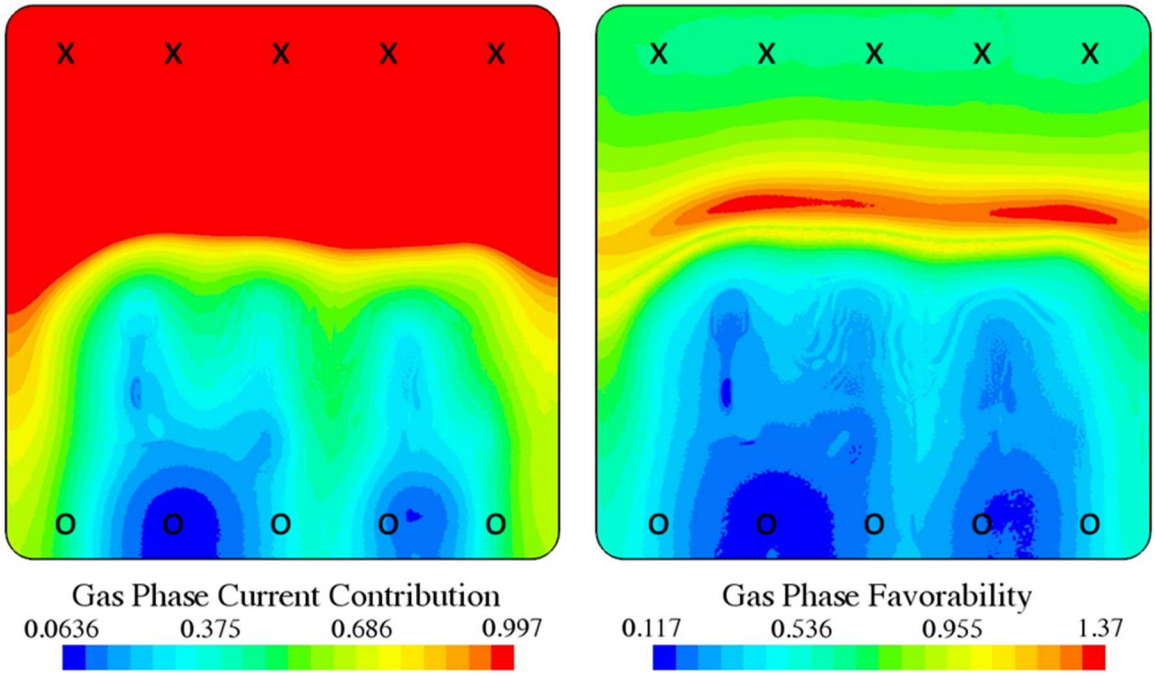

Figure 3.12: The dimensionless gas phase current contribution and A-OER(G) favorability at 1.9 V, 55°C, wet/dry operation with PTL1 and an anode feed rate of 5 mL min-1. A current contribution value of 1 indicates that the A-OER(L) is completely suppressed and a favorability of 1 indicates that the A-OER(G) is just as favorable as the A-OER(L). “o” denotes an inlet and “x” denotes an outlet (Lopata, Weidner, et al. 2022).

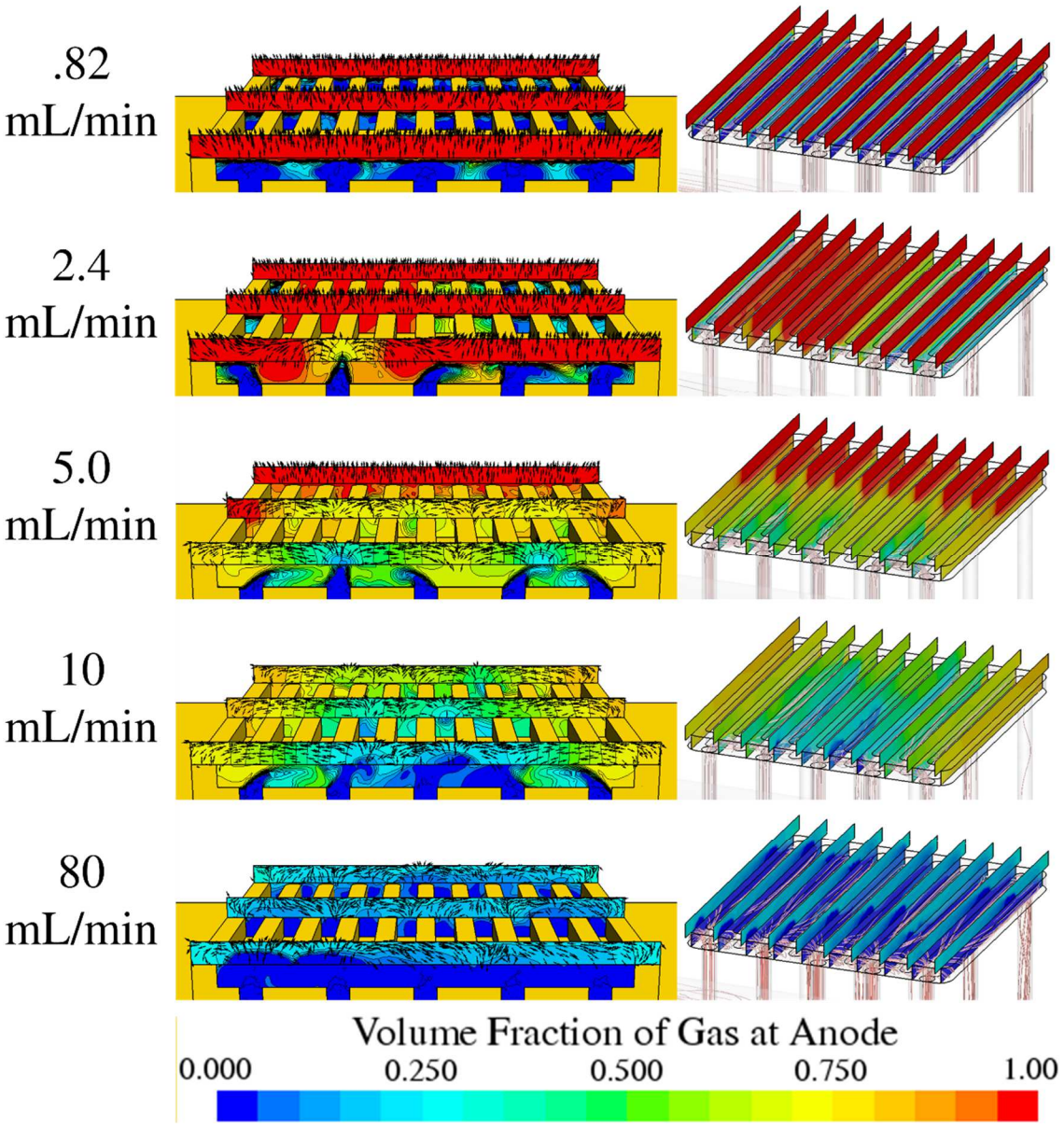

Figure 3.13: Void fraction profiles across and along the anode flow field channels at 1.9 V, 55 °C, wet/dry operation at the 5 feed rates studied. In the cross-channel distributions, vectors indicate the flow direction at the base of the vector within the sample plane, not the fluid velocity. The streamlines in the along-channel images illustrate the path the fluid travels, with darker streamlines indicating higher velocity (Lopata, Weidner, et al. 2022).

to flow along the middle channels, especially at 10 mL min^{-1}, because there was resistance to flow toward the outer channels from the displacement caused by gas formation in the land areas along the edges of the flow field. This effectively directed water from the first and fifth injection channels toward the middle. Ultimately, this enhanced local performance near the edges of the flow field. The most obvious manifold effect is the prominence of the liquid phase adjacent to the injection sites. This is likely due to the orientation of the injection channels. Injection channels are often perpendicular to the electrode in order to efficiently deliver reactants to the electrode. However, when performance depends in part on a gas-phase reaction facilitated by evaporation, the intended benefit may not be realized, and it may actually be better to introduce water to the flow field parallel to the channels, relying on capillary action to draw it into the PTL. This is a suggestion that ultimately requires an experimental investigation to confirm. If true, it is an example of how water electrolyzers behave in ways that are unexpected when using intuition from other types of electrochemical devices. From a practical design and construction perspective, it may not be desirable to alter the geometry of the flow field or manifolds, perhaps because it would make the design less compact and require more materials. Furthermore, the degree of non-uniformity is inherently unpredictable and it may be more efficient to design other components of the cell to limit water content. In the next section, PTL properties are altered to evaluate their effects on cell performance (Lopata, Weidner, et al. 2022).

Improving Cell Performance Through PTL Design.

In light of the results so far, one may reason that any adjustment that allows the PTL to facilitate higher evaporation rates will enhance cell performance by increasing the amount of water vapor available for consumption in the A-OER(G). Returning to Figure

3.9, this model has already suggested that doubling the interfacial area, perhaps by reducing pore size, leads to higher current density. Reducing the permeability in either the in-plane or through-plane direction also increases current density. At 5 mL min^{-1}, increasing the anode PTL porosity to 0.65 slightly increased current density in this model, but in this case, easing liquid water transport within the PTL along the channel prevented severe evaporative cooling mid-channel because the liquid saturation gradient was dulled. Additionally, the average anode and cathode temperatures were higher at higher porosity, improving thermodynamic and kinetic favorability. It is possible that the reduced effective thermal conductivity of the PTL played some role in resisting heat dissipation. Overall, the increase in current density was only about 200 A m^{-2}, but this was under the assumption that the interfacial area was unaffected. An increase in interfacial area would have led to even higher performance. The effect of varying orthotropic permeability on fluid flow in the channels was unexpected. When the permeability was reduced in the in-plane direction, which was intended to induce land-channel effects that would locally reduce liquid saturation, the overall liquid saturation increased and liquid water no longer favored the middle channels as they did with the isotropic PTL1. Figure 3.14 shows the anode liquid saturation and current density of the [0.1, 0.1, 1.0] case. Reducing in-plane permeability led to greater uniformity in the liquid saturation and current density while reducing through-plane permeability caused more non-uniformity. Figure 3.15 explains the anomalous behavior. Restricting in-plane transport within the PTL limits the extent to which liquid water can enter because lateral flow is suppressed. In the isotropic and [1.0, 1.0, 0.1] cases, water that enters the PTL can easily move laterally, continuously being replaced by more liquid water. Once the water finds a low-resistance path, which is through

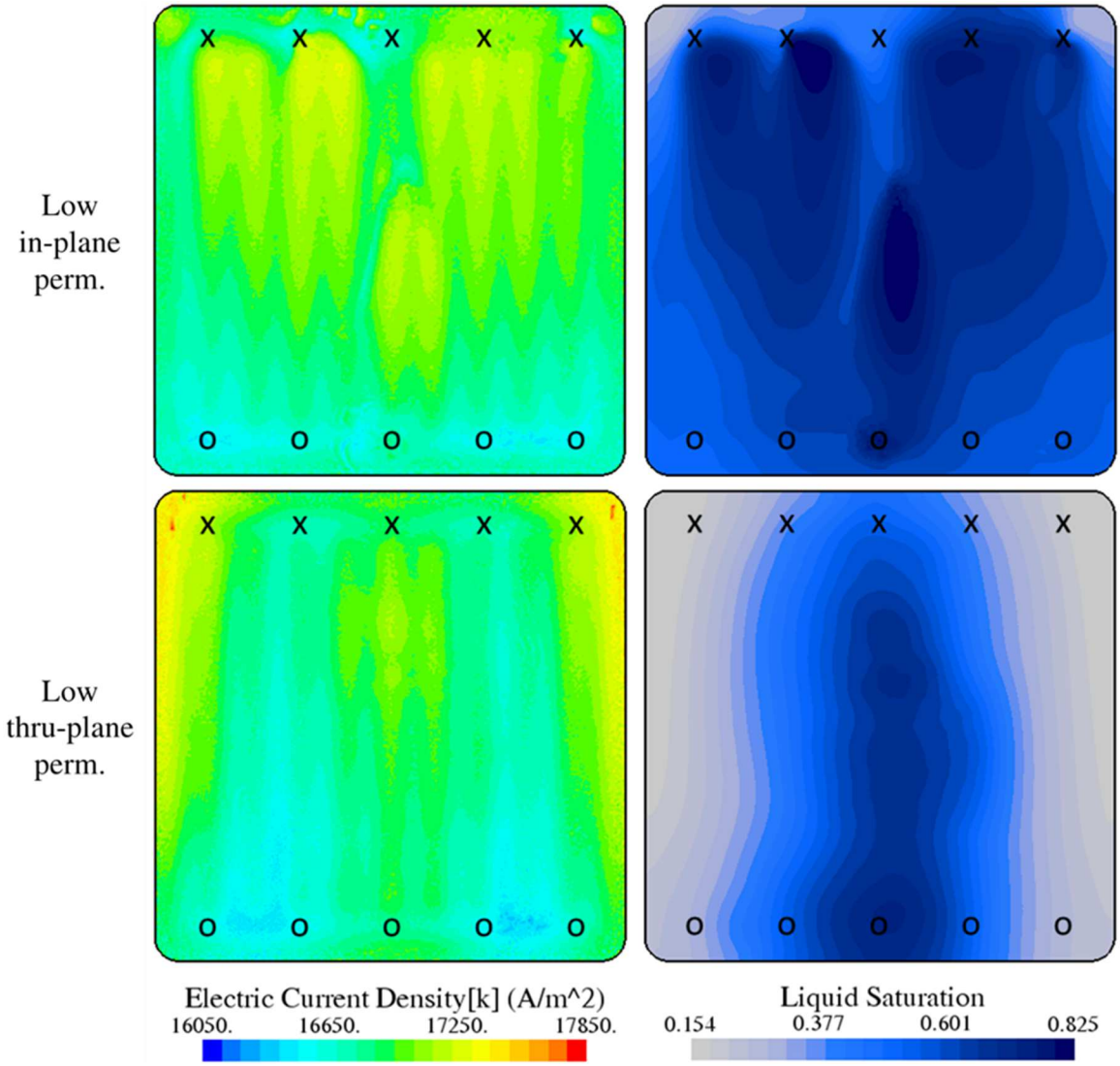

Figure 3.14: Current density and liquid saturation distributions for PTL1 with reduced in-plane permeability at 1.9 V, 55 °C, wet/dry operation with 10 mL min^{-1} of liquid feed to the anode. Compare with the 10 mL min^{-1} result in Figure 3.10. “o” denotes an inlet and “x” denotes an outlet (Lopata, Weidner, et al. 2022).

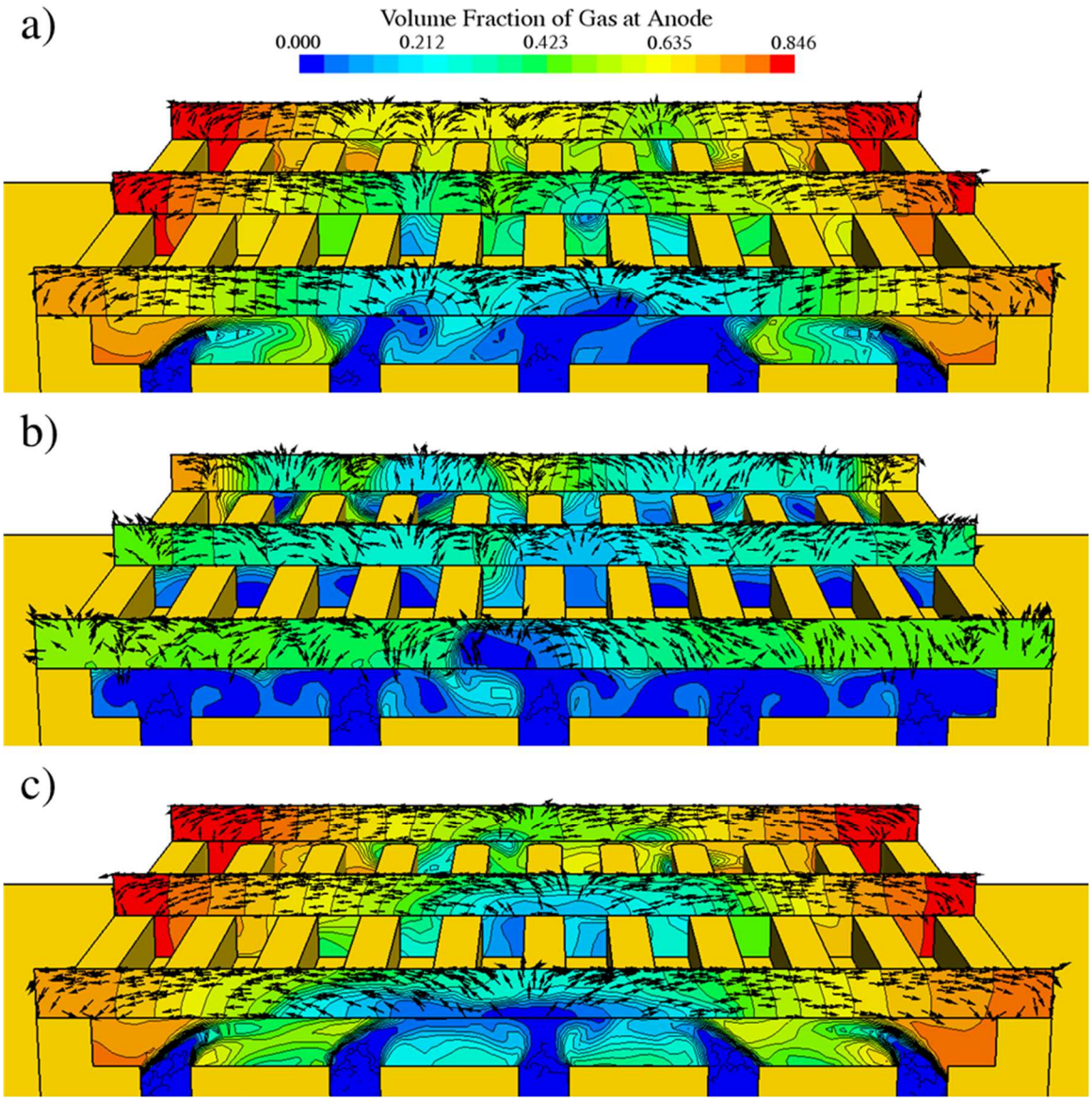

Figure 3.15: Inlet flow behavior at 1.9 V, 55 °C with 10 mL min^{-1} feed. This is a comparison among a) PTL1, b) PTL1-[0.1, 0.1, 1.0], and c) PTL1-[1.0, 1.0, 0.1] (Lopata, Weidner, et al. 2022).

the center, the flow of water from the injection channels is redirected. In the [0.1, 0.1, 1.0] case, more water remains in the flow field channels without being redirected, making the flow more uniform. Neither of the orthotropic PTLs enhanced overall performance much at 10 mL min^{-1}, but both increased average current density by 200-300 A m^{-2} at 5 mL min^{-1}, at which the performance was particularly sensitive. With low in-plane PTL permeability, liquid water has greater propensity to move downstream through the channels, so liquid water presence at the anode remains near the inlet, shifting the liquid/gas front closer to the inlet and increasing the electrode area in which the A-OER(G) dominates, leading to higher performance. When through-plane permeability was low, it further resisted liquid water penetration but not in-plane transport, still allowing flow redirection toward the middle channels. Because the liquid saturation was reduced by the low through-plane permeability, the evaporation rate was high, but the gradients at the liquid/gas front were dulled, preventing localized evaporative cooling that would reduce temperature. While the flow behavior differed among these cases, both in-plane and through-plane reductions in permeability increased cell performance.

One can reason that PTL properties can be tuned in order to improve performance by promoting fairer reaction conditions at the anode. So far, it has been shown both experimentally and computationally that lower flow rates improve cell performance. Simulations suggest that it is both an enhancement in temperature and relative humidity that is responsible for this improvement. Higher temperatures are expected because lower feed rates remove less heat through convection and higher relative humidity is expected because lower feed rate results in lower liquid saturation, which in turn increases the evaporation rate. Furthermore, an increase in current causes additional heat generation,

further increasing the cell temperature and creating a perpetuating feedback loop. This work investigates effects of PTL properties on cell performance and determines the mechanism through which they impact current density. The model suggests that decreasing the PTL permeability improves performance by regulating water transport to allow more favorable conditions for evaporation. Reducing permeability by a factor of 0.1 in only the through-plane direction broadens the region dominated by the gas phase while reducing permeability in the in-plane direction actually increases the uniformity of anode conditions. It is suggested that more than doubling the porosity of the anode PTL to 0.65 increases performance slightly by affecting both mass and heat transport. Doubling the liquid/gas interfacial area leads to the greatest increase in current because it directly increases the evaporation rate. The liquid/gas interfacial area can be influenced by changing water content or by changing PTL properties such as porosity and pore size.

Though low feed rates enhance performance, there are likely to be reasons to avoid cell operation at low feed rates. First, cell behavior and anode conditions are more unpredictable. No model accounts for every existing phenomenon (e.g. this model neglects gravity), so conditions at the anode may be different from the expected. Secondly, the cell may be subject to fluctuations in demand. While the feed rate can be automatically adjusted based on desired current, the anode may experience harsh conditions in transient stages such as when the cell voltage increases or the cell is started. Cycling is known to expedite material degradation in electrochemical cells in general. If anode conditions are highly non-uniform, it is likely that parts of the anode CL experience dry conditions at high potential.

Motivated by the desire to promote uniform conditions at the anode, this investigation finishes with the results of a simulation with the following adjustments made

to the properties of PTL1: The permeability is reduced by a factor of 0.01 in the through-plane and cross-channel dimensions, the porosity is set to 0.65, and the interfacial area is doubled. The simulated cell operates at 1.9 V with a temperature setpoint of 55 °C, outlet pressure of 1 atm, and a liquid feed rate of 10 mL min^{-1} to only the anode. The performance under these conditions with the changes to the PTL material is then compared to that of PTL1.

The permeability was reduced in the through-plane direction to regulate the water content at the anode. Additionally reducing permeability in the cross-channel direction was intended to prevent inlet flow redirection toward the middle channels and increase uniformity. The along-channel permeability was left alone because the model had previously suggested that lower permeability along the channel leads to sharper liquid/gas fronts and temperature non-uniformity. Increasing the PTL porosity to 0.65 was intended to trap more of the heat generated by the OER and increase uniformity. The combined increase in porosity and reduction in permeability was assumed to be done in such a way that the liquid/gas interfacial area was doubled. In essence, it should be possible to increase cell performance considerably at moderate feed rate of 10 mL min^{-1} to rival the performance at lower feed rates.

Figure 3.16 shows the current, temperature, liquid saturation, and relative humidity distributions at the anode, the void fraction distributions across and along the channels, and the relative A-OER(G) contribution and favorability distributions. First to note in Figure 3.16a is that the current density is both higher and more uniform than under the same operating conditions with PTL1 (refer to Figure 3.10). The overall current density is 18,175 A m^{-2} compared to 16,857 A m^{-2} for PTL1. Performance is comparable to that at feed rates

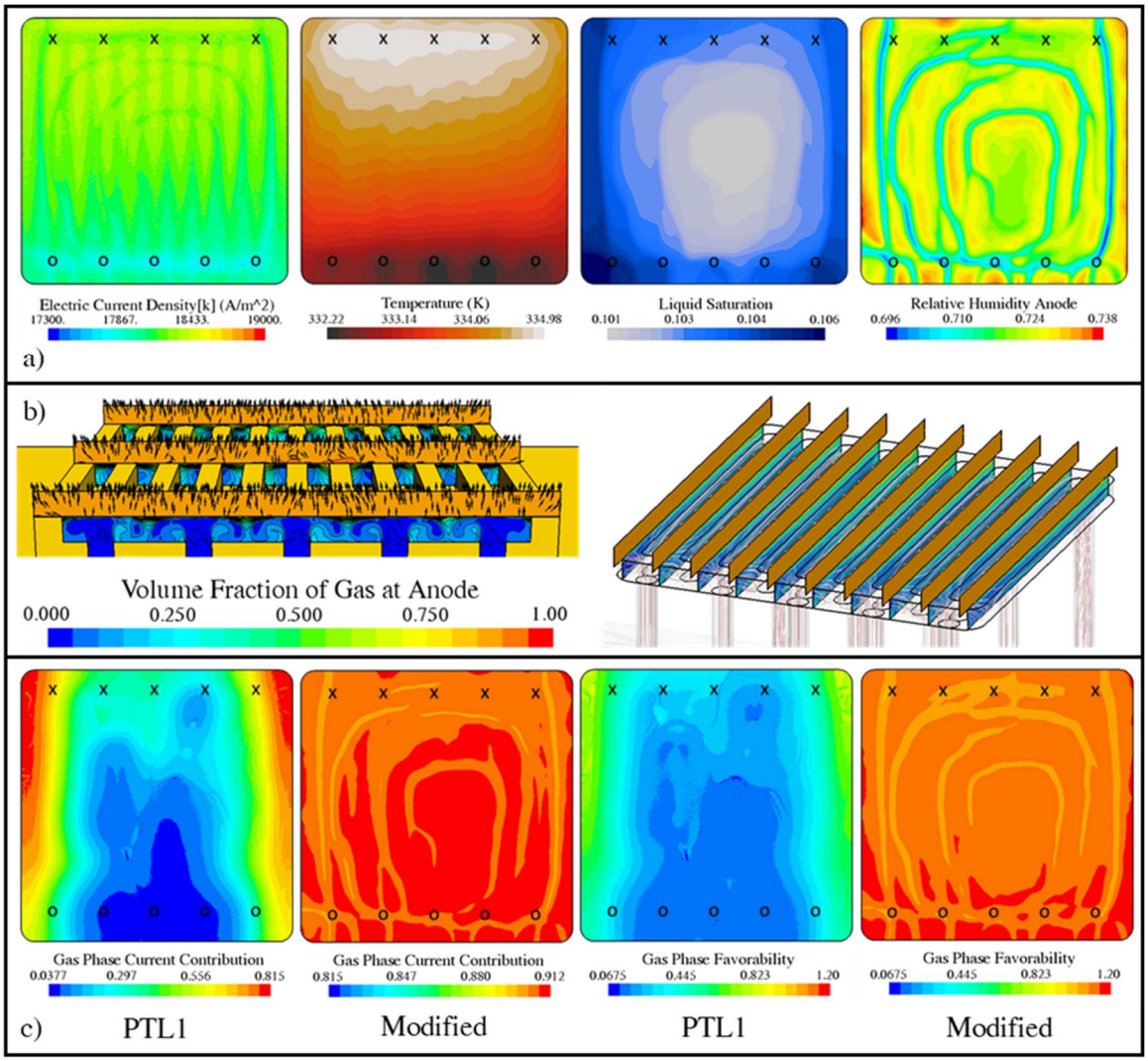

Figure 3.16: Compilation of distributions for 1.9 V, 55 °C, 1 atm operation with 10 mL min^{-1} liquid water feed to the anode in wet/dry configuration, using a modified PTL derived from PTL1 with 100 times lower permeability in the through-plane and cross-channel dimensions, a porosity of 0.65, and 2 times more liquid/gas interfacial area. “o” denotes an inlet and “x” denotes an outlet. a) Current density, temperature, liquid saturation, and relative humidity distributions across the anode interface. b) Void fractions in the anodic flow field channels and PTL. Streamlines show fluid flow paths in the channels while black vectors show the flow direction within the PTL. c) Comparison of relative gas-phase current contribution and A-OER(G) favorability distributions across the anode interface for PTL1 and the modified PTL (Lopata, Weidner, et al. 2022).

of 2.4 mL min^{-1} or less without the modifications despite the lower anode temperature. The PTL modifications avoided causing sharp gradients in liquid saturation and relative humidity, which were highly uniform. Liquid saturation was regulated to just above 0.1, which is slightly above the optimal value of 0.05 from the interfacial area function, but low enough to facilitate the evaporation needed to sustain a rather uniform relative humidity in the whereabouts of 0.72. This can be explained by the void fraction distributions in Figure 3.16b, which illustrate how the lower PTL permeability prevented the redirection of inlet liquid toward the middle channels. In Figure 3.16c, the effect of these variables on the A-OER(G) at the anode is provided. In the modified PTL, the A-OER(G) contribution is both higher and more uniform than in PTL1. This is due to the much higher favorability of the A-OER(G), which is also higher and more uniform than in PTL1. With PTL1, the favorability of the A-OER(G) never exceeded that of the A-OER(L), but after making performance-improving modifications, the A-OER(G) favorability is just as high or higher than that of the A-OER(L). The simulation therefore suggests that through engineering of the PTL, performance can be enhanced by regulating transport to increase the A-OER(G) contribution as opposed to minimizing the presence of the gas phase.

It is important to mind the observations made by Lopata et al. (J. Lopata, et al. 2020), which clearly show that the reaction conditions between the PTL grain and membrane may vary considerably from within the PTL pores, especially when very thin, low-loaded CLs are used. This effect was neglected in the simulations, which assume a homogeneous interface. Reducing PTL permeability and thereby liquid saturation without considering how this would impact the species composition in hard-to-access portions of

the CL is ill-advised. However, this motivates further experimental development of PTL materials and studies of the PTL/CL interface (Lopata, Weidner, et al. 2022).

Conclusion

Evaporation is a very important process in PEMWE of which to take advantage. The rate of evaporation influences the relative humidity and thereby the thermodynamic and kinetic favorability of the A-OER(G). Material design and operating conditions can be tuned to promote evaporation and enhance the A-OER(G) favorability, increasing cell performance. More specifically, the relative humidity can be increased by producing an anode environment with limited liquid water content, but in a controlled manner such that it remains highly uniform across the anode. This desired effect can be achieved by slightly reducing feed rate, decreasing PTL permeability in the through-plane and cross-channel dimensions, and increasing the porosity and specific surface area of the PTL. To reach this conclusion, the manner in which PTL properties impacted fluid flow through the parallel channels required consideration. The simulations in this chapter suggest that this approach reduces the dependence of performance on low-feed-rate operation and high anode temperatures, protecting the lifespan of the device while improving efficiency.

CHAPTER 4

THE LINK BETWEEN MANIFOLD DESIGN AND LOCAL CURRENT DENSITY IN ZERO-GAP ALKALINE DIAPHRAGM WATER ELECTROLYSIS DEVICES

Investigating Impacts of Geometry on Performance

In Chapter 3, it was important to consider fluid flow, which depends on cell geometry. This insight and the same model from Chapter 2 was applied to a zero-gap ADWE design concept to evaluate the effects of operating conditions and geometry on current distributions, gas crossover, and shunt current in stacks. Kinetic limitations were considered under the assumption of no gas-phase B-OER. ADWE devices use concentrated caustic feed solutions, which exhibit water activities less than 1. While this is detrimental to kinetics, it is necessary in order to enhance the cell conductivity. ADWE devices, as explained in Chapter 1, possess higher resistance than PEMWE cells due to phenomena at the ESI. The model in this chapter applies this extra resistance to the ESI boundaries in the computational domain, using a constant, fitted value.

Electrochemical Equations

Species generation and consumption at the electrode interfaces due to the reaction for ADWE was the same as Equation 3.1. Water evaporation was not considered at the interface in the ADWE model as it was in the PEMWE model. However, the crossover of water driven by differential pressure and, consequently, the crossover of dissolved gases was considered:

$$\vec{n}_w^{co} = M_w \left(\frac{\nu_{ad}^{eo} \vec{\imath}}{F} - \frac{\kappa_{ad}}{\mu_L} \frac{\Delta P_L}{L_{ad}} \right) \tag{4.1}$$

The crossover of dissolved hydrogen and oxygen was dependent on the crossover of the solution, the diffusivities, and the solubilities of hydrogen and oxygen per the following two equations derived from empirical models by Schalenbach et al. (Schalenbach, Lueke and Stolten 2016),

$$\vec{n}_{O_2}^{co} = C_{O_2}^{sat} M_{O_2} \max \left\{ \left(\varepsilon_{ad}^{b_{ad}} D_{O_2} \frac{\Delta P_{O_2}}{L_{ad}} + \frac{\kappa_{ad} P_{O_2,a}}{\mu_L} \frac{\Delta P_L}{L_{ad}} \right) + \frac{P_{O_2,a} \vec{n}_w^{co}}{\rho_L}, 0 \right\} \tag{4.2}$$

$$\vec{n}_{H_2}^{co} = C_{H_2}^{sat} M_{H_2} \max \left\{ \left(\varepsilon_{ad}^{b_{ad}} D_{H_2} \frac{\Delta P_{H_2}}{L_{ad}} + \frac{\kappa_{ad} P_{H_2,c}}{\mu_L} \frac{\Delta P_L}{L_{ad}} \right) + \frac{P_{H_2,c} \vec{n}_w^{co}}{\rho_L}, 0 \right\} \tag{4.3}$$

The current densities at the anode and cathode, respectively, are expressed as Tafel approximations, given the high overpotentials of interest, with factors describing the concentration dependence of the reaction:

$$\vec{\imath}_a = si_{0,a}^{ref} \exp \left\{ -\frac{E_{act,a}}{RT} \right\} \frac{C_{OH^-}}{4.5} \exp \left\{ \frac{\alpha_a F \eta_a}{RT} \right\} \tag{4.4}$$

$$\vec{\imath}_c = si_{0,c}^{ref} \exp \left\{ -\frac{E_{act,c}}{RT} \right\} a_w^2 \exp \left\{ \frac{-\alpha_c F \eta_c}{RT} \right\} \tag{4.5}$$

in which E_{act} is the activation energy, determined empirically (Kibria and Mridha 1996, González-Buch, et al. 2013). The transfer coefficients are linear functions of temperature, with that at the anode (Kibria and Mridha 1996) and cathode (González-Buch, et al. 2013), respectively, being

$$\alpha_a = 0.00348432\, T + 0.289512 \tag{4.6}$$

$$\alpha_c = -0.00332443\, T + 2.35202 \tag{4.7}$$

Note that the slopes are fit to data from Kibria and Mridha (Kibria and Mridha 1996) and Gonzalez-Buch et al. (González-Buch, et al. 2013) while the intercepts were determined

using reference points of 1.52 and 1.178 at the anode and cathode, respectively, at a temperature of 80 °C. The anodic and cathodic overpotentials are again defined based on potential drop and equilibrium potential, this time including a term containing the ohmic resistance of the electrode/separator interface R_{esi},

$$\eta_{s,a} = -\Delta\phi_a - \vec{\imath} R_{esi,a} - \phi^{\circ}_{eq,a} - \frac{\Delta S^{\circ}_a}{F}(T - T^{\circ}) + \frac{\mathscr{R}T}{F}\ln\left\{\sqrt{\frac{\Upsilon_{\pm} m_{KOH}}{a_w\sqrt{1 - P_{O_2}}}}\right\} \quad (4.8)$$

$$\eta_{s,c} = -\Delta\phi_c - \vec{\imath} R_{esi,c} - \phi^{\circ}_{eq,c} - \frac{\Delta S^{\circ}_c}{F}(T - T^{\circ}) + \frac{\mathscr{R}T}{F}\ln\left\{\frac{\sqrt{P_{H_2}}}{a_w}\Upsilon_{\pm} m_{KOH}\right\} \quad (4.9)$$

The overpotentials are dependent on the activity of water, which is less than 1 in concentrated solutions, and the KOH activity. $\Upsilon_{\pm}$ can be expressed in terms of the KOH mole fraction x_{KOH} to within 6% of the Gibbs excess model from Li and Pitzer (Li and Pitzer 1996),

$$\begin{aligned}\Upsilon_{\pm} = \exp\{&-0.0151895 - 46.8743\, x_{KOH} + 343.766\, x_{KOH}^2 - 566.491\, x_{KOH}^3 \\ &+ 472.221\, x_{KOH}^4 \\ &+ \left(4.34773\times10^{-5} + 0.258126\, x_{KOH} - 1.38799\, x_{KOH}^2\right. \\ &\left. + 1.89206\, x_{KOH}^3 - 1.39535\, x_{KOH}^4\right) T \\ &+ \left(-1.10721\times10^{-7} - 4.37513\times10^{-4}\, x_{KOH}\right. \\ &+ 0.00228340\, x_{KOH}^2 - 0.00398424\, x_{KOH}^3 \\ &\left. + 0.00344981\, x_{KOH}^4\right) T^2\}/(1 + 0.03603\, m_{KOH})\end{aligned} \quad (4.10)$$

$$x_{KOH} = \frac{2m_{KOH}}{55.5093 + 2m_{KOH}} \quad (4.11)$$

$$
\begin{aligned}
m_{KOH} = \big(&1.28756\times10^{-9}\,T^2 + 4.57346\times10^{-7}\,T \\
&+ 8.51811\times10^{-4}\,\big)\,C_{KOH}^3 \\
&+ \big(-1.87305\times10^{-8}\,T^2 + 3.52482\times10^{-6}\,T \\
&+ 0.00764237\,\big)\,C_{KOH}^2 \\
&+ \big(3.09226\times10^{-7}\,T^2 + 3.67376\times10^{-4}\,T \\
&+ 0.869801\big)\,C_{KOH}
\end{aligned}
\tag{4.12}
$$

Entropies are found using Equations 3.16-19, but there is an additional one for the hydroxide ion:

$$S_{OH^-} = -R\ln\{Y_{OH^-}m_{OH^-}\} + Rc_P\ln\left\{\frac{T}{298}\right\} - 10.54 \tag{4.13}$$

where Y_{OH^-} is the single ion activity coefficient, approximated as

$$Y_{OH^-} = 0.3229\exp\{0.3214\,Y_{\pm}\} \tag{4.14}$$

and the hydroxide molality is

$$m_{OH^-} = 0.30314\,m_{KOH} \tag{4.15}$$

With the definitions of overpotential and the anodic and cathodic currents, Equations 3.9-15 can then be used to calculate R_{ik} at both electrodes.

Geometry

The single cell geometry, shown in Figure 4.1, consisted of two plates, manifolds with extrusions at the inlets and outlets (extrusions not shown), two PTLs, two electrodes, and a diaphragm separator. The computational domain was based on a design concept, with the component thicknesses and general assembly configuration based on the experimental cell. The cross-sectional area of the cell was about 729 cm^2 and the electrodes, PTLs, and separator were 0.7, 0.9, and 0.46 mm, respectively. A thin mesher was used to achieve accurate and efficient discretization of this thin domain. The thin meshing technique

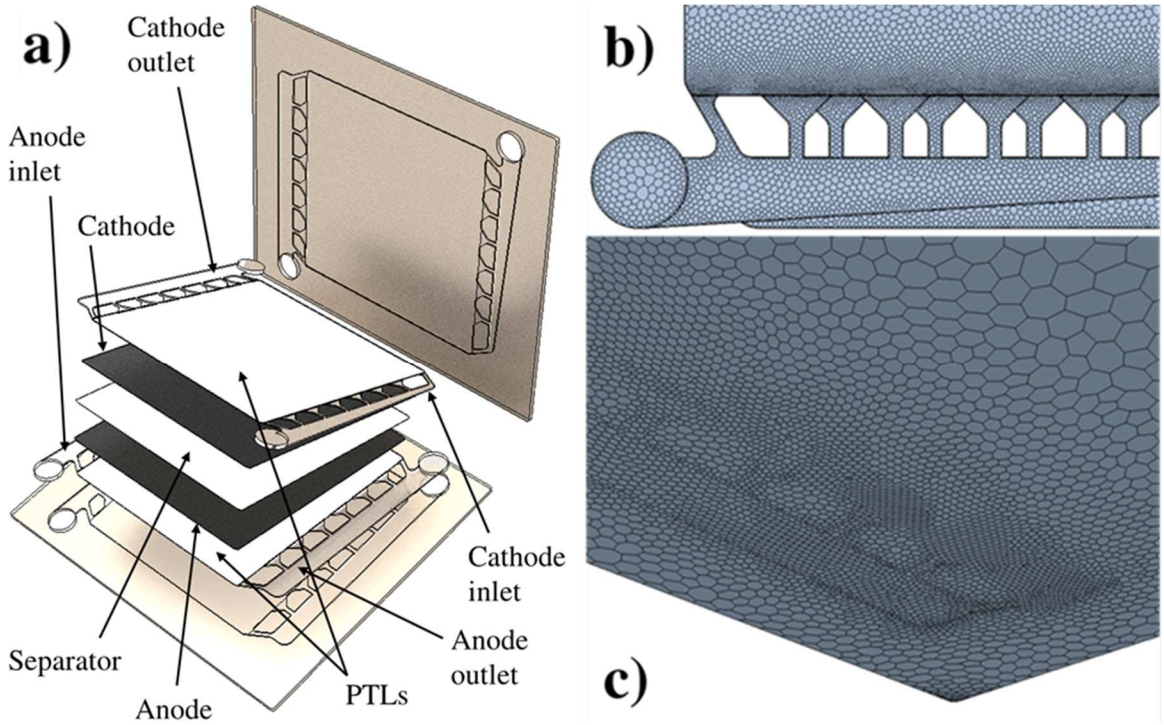

Figure 4.1: a) Components of the single cell model, including CCs, PTLs, electrodes, inlet/outlet manifolds, and the separator. b) A zoomed depiction of the volume mesh of fluid regions near the manifolds. c) The impact of compatibility refinement on the backside of a CC (J. S. Lopata, et al. 2021a).

allowed for a high-quality representation of the geometry, including extrusions of the inlets and outlets, with a total of 509,728 cells. Through early testing with a simple rectangular geometry, it was found that fluid flow velocity through a thin region bound by walls with no-slip conditions was accurately computed when at least 8 thin layers (368 cells) were generated in the mesh. Doubling the number of thin layers to 16 (736 cells) resulted in a 3.3% increase in the maximum velocity while halving the thin layers (184 cells) led to a 12% decrease in maximum velocity. Therefore, the electrodes and PTLs were each given 4 thin layers for a total of 8 layers between the plate and the separator on both sides of the cell. The manifolds were meshed with only 4 layers in thin sections, which provided an acceptable flow computation for these regions, which were not in close proximity to the vast majority of the electrochemically active surface. The 1.6 mm manifolds injected solution directly into the electrodes and PTLs by design, as opposed to having non-porous flow channels between the PTL and plate, similarly to the experimental cell.

The mesh size at the injection/ejection areas in the electrodes and PTLs was set to a small value of 0.6 mm near the manifolds and allowed to expand to a maximum of 6.7 mm toward the middle of the flow field. This was in expectation of the gradients that would form in proximity of the injection/ejection areas. A large target mesh size was applied to the plates, in which only potential and energy are modeled. However, due to the thinness of the plates in some sections, compatibility refinement was enabled to ensure high cell quality in sections of the plate near the internal porous media. Figure 4.1c exhibits the outcome of this refinement.

By changing the number of thin layers in each region, coarse and fine meshes were produced. At 2.4 V, the simulated average current density varied by about 2% among meshes (J. S. Lopata, et al. 2021a).

Boundary Conditions

Figure 4.2 contains an abstract diagram of the ADWE cell with its boundary conditions. The boundary conditions are similar to those of the PEMWE model, but note the change in equation numbers at the electrode boundaries to Equations 4.1-15 and Equations 3.9-15 along with the addition of a KOH mass fraction condition of 0.3 at the inlets. Because the solver does not distinguish between solid and electrolyte current in this model, a resistance of 10^{20} Ω m^2 was applied to the manifold walls bounded by the CC plates. Additionally, a gasket surrounds the diaphragm, which transports heat.

Numerical Methodology

Siemens Simcenter Star-CCM+ 2020.1.1 Build 15.02.009 was used to solve the governing equations using the finite volume method. The SIMPLE algorithm was applied with Gauss-Seidel relaxation. Conjugate gradient acceleration was applied to the pressure solver. The following solver sequence is summarized in Table 4.1. Final under-relaxation factors of 1.0, 0.5, 0.1, 0.995, 0.9995, 0.9, and 0.99 were set for the potential, velocity, pressure, neutral species, charged species, fluid energy, and solid energy solvers, respectively. A flow solution with no reaction was obtained prior to initiating the other solvers. The potential solver was activated second, with the solution occurring in four stages: 1) A 0-dimensional model was used to determine constant values of interfacial resistance, including $\boldsymbol{R}_{esi}$ and $\boldsymbol{R}_{tk}$, at the anode and cathode, which were used for tens of iterations. 2) The Newton-Raphson-stabilized electrochemical reaction model described in

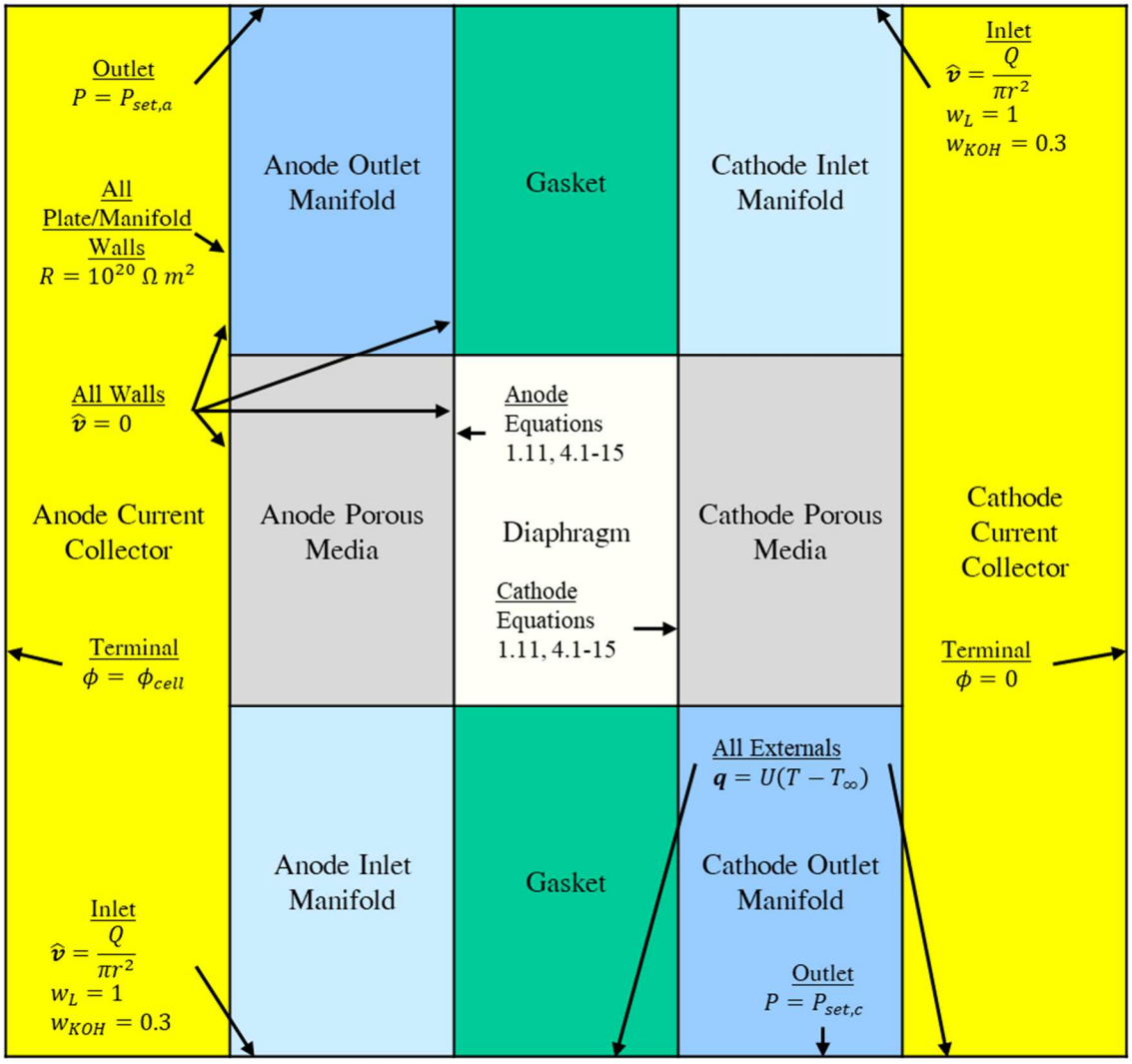

Figure 4.2: Abstract diagram of boundary conditions in the ADWE cell. A cutaway of the geometry is not given for clarity because it is too thin.

Table 4.1: ADWE Model Solver Sequence

Iteration	Event
$\geq$ -1,000	Flow solver activated
0	Potential solver activated with a constant $R_{tk,a}$
60	$R_{tk,a}$ determined iteratively
200	Species and energy solver ramps started
500	Species and energy solver ramps finished
$\geq$ 600	Gas diffusivities multiplied by $(1 - s)^b$, volumetric phase change started
$\geq$ 600	Compressible flow activated, densities of species become functions of temperature and/or pressure

Equations 3.9-15 was allowed to compute new local values for interfacial resistance. 3) The charged species solver was ramped from 0 over 100 iterations to solve for the concentration of KOH in the channels, PTLs, and electrodes. 4) At the end of the charged species solver ramp, the neutral species and energy solvers were ramped from 0 over 300 iterations. Compressibility, gas and solution crossover, and gas diffusion limitations due to the presence of the liquid phase were considered 100 iterations after the end of the species solver ramp. Thereafter, convergence was said to be achieved after the residuals stabilized, the current density varied by less than 10 A m^{-2} in 1000 iterations, and the percent flammability limit (%LFL) of hydrogen in the anode reached a stable value (J. S. Lopata, et al. 2021a).

Experimental Validation of the ADWE Model

As shown in Figure 4.3a, a single cell with an active area of approximately 36 cm^2 was constructed in a zero-gap configuration with nickel PTLs, nickel CCs, and a Zirfon PERL UTP-500 separator. Raney nickel and nickel-iron LDH were used as the cathodic and anodic catalysts, respectively, both on nickel foam supports. Nickel foams were also used as PTLs. The CCs contained no flow fields, instead directing the feed solution into the porous media. Cell performance was evaluated at a temperature of 80°C and a total feed rate of 30 wt% KOH solution equal to 400 mL min^{-1}, i.e. ~11.1 mL min^{-1} cm^{-2}. The anolyte and catholyte were fed in a countercurrent configuration. Galvanostatic polarization experiments were conducted by incrementing current density in the range from 0 to 2 A cm^{-2} using a Biologic HCP-803 potentiostat/galvanostat. Each current was applied for at least 10 min to obtain a steady- state result. The electrolyzer was operated in a partially separated cycle, which allowed partial mixing of the catholyte and anolyte by opening a

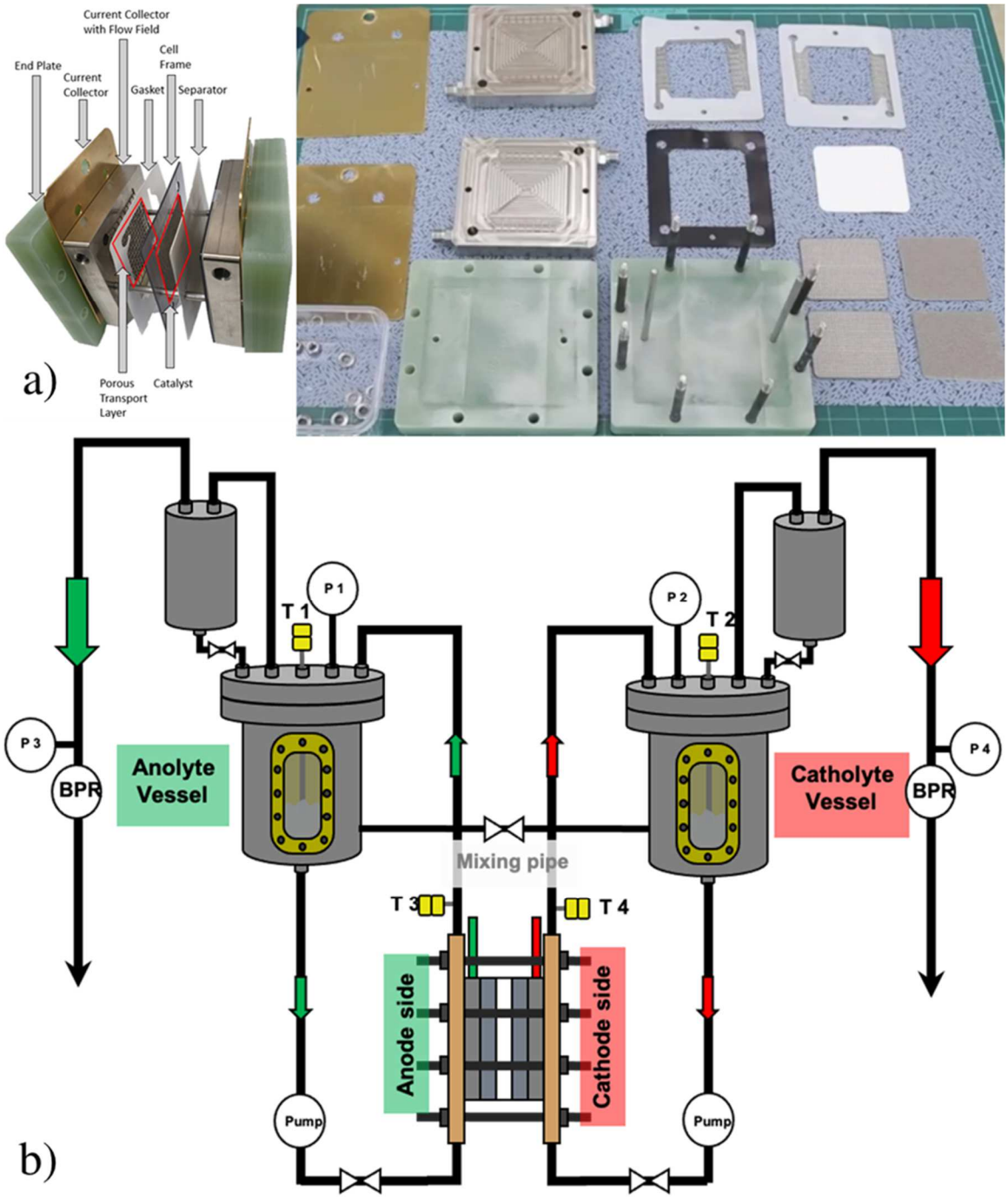

Figure 4.3: Experimental hardware and setup for ADWE. a) Schematic of the experimental test station. b) Cell assembly and components (J. S. Lopata, et al. 2021a).

mixing pipe valve between the KOH chambers to control the OH^- concentration. A schematic of the overall process is illustrated in Figure 4.3b (J. S. Lopata, et al. 2021a).

Discussion

Effect of the Gas Phase on Cell Performance.

ADWE model operating conditions are provided in Table 4.2. The polarization curves in Figure 4.4 show the effect of flow rate on the average current density at solution feed rates of 8.10 (A), 4.05 (B), and 2.03 L min^{-1} (C) per half-cell. For each of the three cases, the total cell potential is decomposed into smaller components of potential, namely equilibrium potential, resistance, anodic and cathodic activation, and mass transport overpotentials. The change in flow rate did nothing significant to impact any potential component except the mass transport overpotential. Experimental data is overlayed for comparison purposes. The 4.05 L min^{-1} simulation data series best fits the experimental data, as it should for being the equivalent of the experimental flow rate, corrected based on electrode area. As the flow rate was reduced, the total mass transport overpotential increased, reducing the average current density by more than 1,000 A m^{-2} at 2.4 V. This highlights the importance of using very high feed rates in ADWE, as there is no appreciable gas-phase reaction according to our current understanding.

The mass transport overpotentials attributed to the void fraction and solution concentration at the anode and cathode are shown in Table 4.3 because they are too small to show clearly in Figure 4.4. The feed rate sensitivity of the mass transport overpotential is rooted in the volume fraction overpotentials $\eta_{vf,a}$ and $\eta_{vf,c}$. $\eta_{vf,c}$ is higher because a greater volume of hydrogen gas is generated at the cathode than of oxygen gas at the anode. The concentration overpotentials $\eta_{conc,a}$ and $\eta_{conc,c}$ describe the effects of KOH

Table 4.2: ADWE Model Operating Conditions

Number of Cells	Anode Feed Rate (L min^{-1})	Cathode Feed Rate (L min^{-1})	Cell Potential (V)	Notation
1	8.10	8.10	1.6	A1
			1.8	A2
			2.0	A3
			2.2	A4
			2.4	A5
	4.05	4.05	1.6	B1
			1.8	B2
			2.0	B3
			2.2	B4
			2.4	B5
	2.03	2.03	1.6	C1
			1.8	C2
			2.0	C3
			2.2	C4
			2.4	C5
	3.04	5.07	2.4	D1
5	40.5	40.5	2.4	S-A5
	20.3	20.3	2.4	S-B5
	10.1	10.1	2.4	S-C5

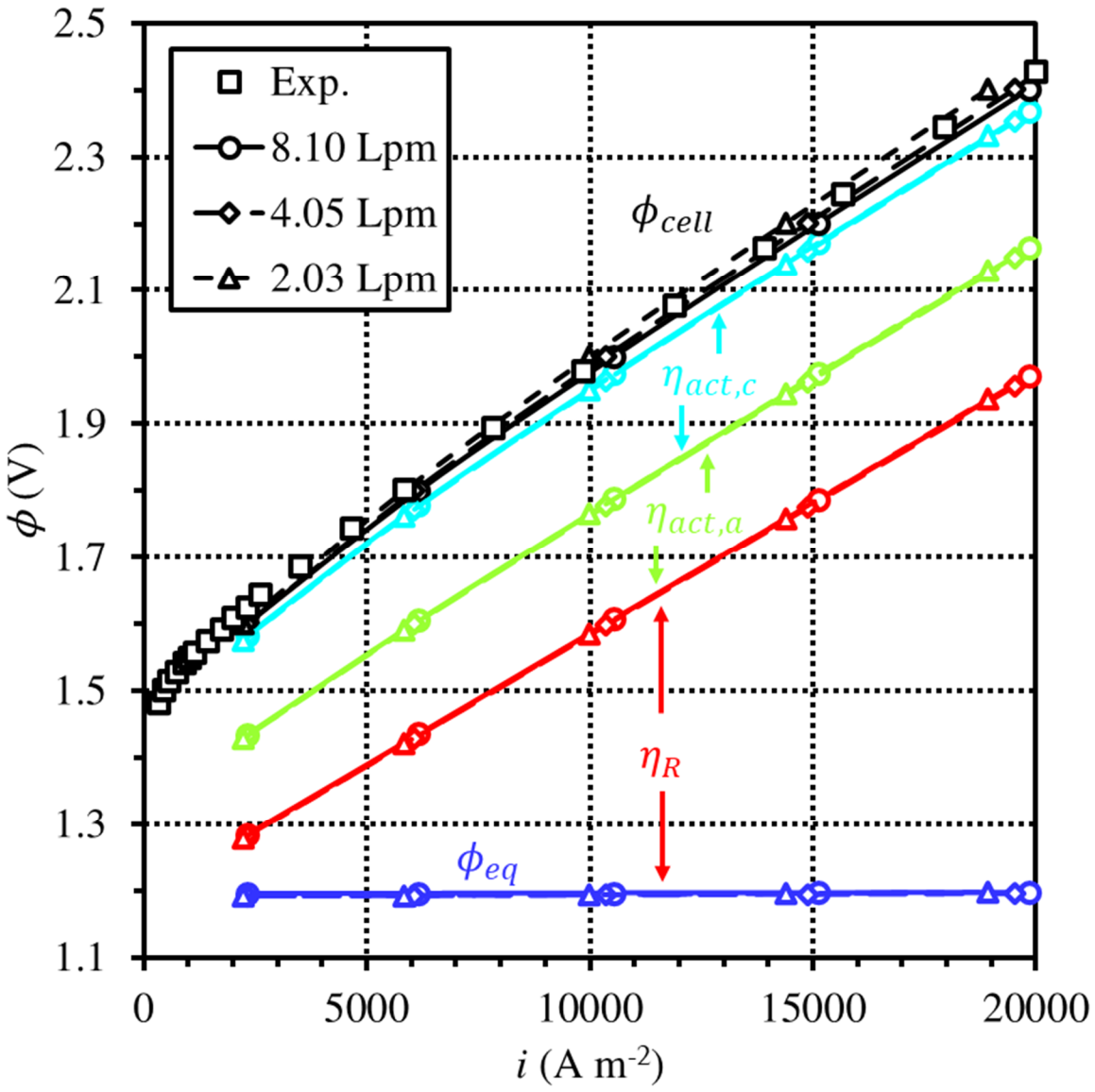

Figure 4.4: Comparison of decomposed polarization curves collected during experiments and simulations. Simulations used different flow rates to show the effect on the overpotential associated with mass transport. The simulated polarization curve is decomposed to show the potential components.

Table 4.3: ADWE Mass Transport Overpotentials

Flow Rate (Lpm)	ϕ_{cell} (V)	$\eta_{mt,tot}$ (mV)	$\eta_{vf,a}$ (mV)	$\eta_{vf,c}$ (mV)	$\eta_{conc,a}$ (mV)	$\eta_{conc,c}$ (mV)
8.10	1.6	17.4	1.0	2.4	-8.0	22.1
	1.8	22.0	2.4	5.5	-8.1	22.2
	2.0	26.2	3.7	8.3	-8.1	22.3
	2.2	29.8	4.9	10.6	-8.1	22.4
	2.4	33.0	6.0	12.6	-8.1	22.6
4.05	1.6	22.2	2.4	5.7	-8.1	22.2
	1.8	31.4	5.3	11.9	-8.1	22.4
	2.0	39.2	8.0	16.8	-8.2	22.6
	2.2	45.8	10.2	20.8	-8.2	22.9
	2.4	51.6	12.2	24.4	-8.2	23.3
2.03	1.6	30.2	5.0	11.2	-8.1	22.2
	1.8	45.2	10.1	20.7	-8.2	22.6
	2.0	57.2	14.3	27.9	-8.3	23.3
	2.2	67.4	17.6	34.0	-8.3	24.1
	2.4	76.4	20.6	39.1	-8.4	25.1

concentration on the overpotential through Equations 4.4 and 4.5 and are not describing overpotential due to diffusion from the bulk to the surface or vice versa. The KOH reference concentration is 4.5 M in Equation 4.4, hence the negative overpotential at the anode. The sum of $\eta_{conc,a}$ and $\eta_{conc,c}$ show the magnitude of the kinetic limitation due to the reduced activity of water, which interacts strongly with K^+ and OH^- ions. Concentrations do not vary much within ADWE cells, which run with high feed rates. At 2.03 L min^{-1} per half-cell, $\eta_{conc,c}$ increased by only 2.9 mV due to increased KOH concentration at the cathode, which will be explained later.

For operation condition series A, B, and C, anodic and cathodic averages of bubble coverage, KOH concentration, %LFL, and the hydrogen purity as a dry-basis volume fraction (H2P) are plotted with current density in Figure 4.5. The bubble coverage plots show how substantial the change in bubble coverage is when the flow rate is cut in half from the experimental equivalent. The results are compared to a power law from Balzer and Vogt (Balzer and Vogt 2003). The cathodic bubble coverage is higher because the molar rate of production of hydrogen is twice that of oxygen. The inlet feed rate affected the KOH concentration as well, which increased by up to 0.2 M with increasing current density and decreasing feed rate. The concentration increase is due to the consumption of water in the B-HER. While water is produced in the B-OER, solution crossover from the cathode causes the concentration to increase slightly despite this. Crossover is caused by the differential pressure across the cell. Cathode pressures are relatively high because more gas is produced, creating more resistance to flow. This will be explained in more detail in the next section.

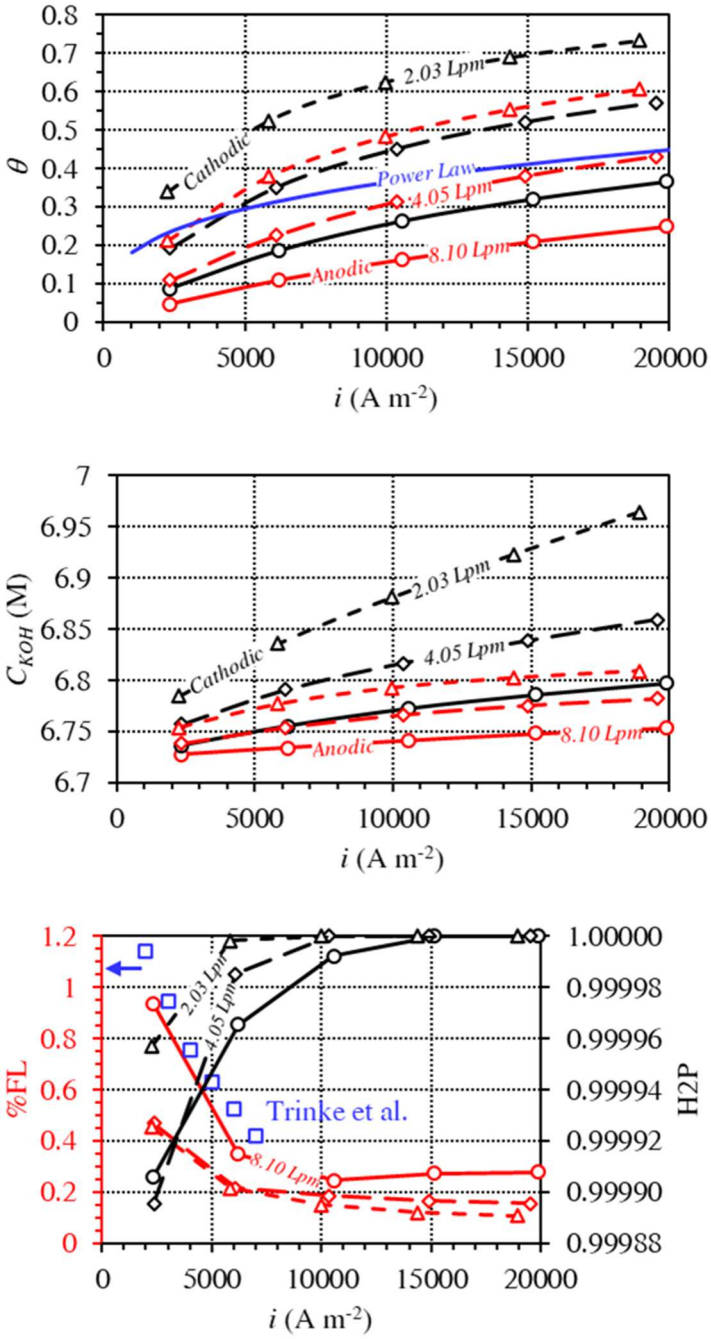

Figure 4.5: The bubble coverage (θ), KOH concentration (C_{KOH}), the percentage of the lower hydrogen flammability limit at the anode (%LFL), and the hydrogen purity at the cathode (H2P) versus the average current density at various solution feed rates. The power law relationship for bubble coverage is from Balzer and Vogt (Balzer and Vogt 2003). The data from Trinke et al. (Trinke, et al. 2018) are used to confirm the plausibility of the model prediction.

Gas crossover in the simulation resembles that of an experimental cell, as evidenced by the comparison of simulation data to the data of Trinke et al. (Trinke, et al. 2018). Their experimental data were consistent with these simulations, which assumed that the feed was a fixed concentration and contained no mixtures of dissolved gases. The exponential decrease in %LFL with increasing current density is due to the increase in gas production, which dilutes crossover products. The H2P increases with increasing current density for the same reason. The %LFL was calculated from the dry gas composition using a lower flammability limit of 4% H_2 in O_2. The H2P was also calculated on a dry basis.

High feed rates led to more hydrogen crossover from cathode to anode because the differential liquid pressure (DLP) across the separator is higher than at low feed rates. The %LFL decreases with increasing current density as expected because faster gas generation further dilutes the small quantity of gas that crosses over with the solution. Hydrogen purity increases from about 99.99% to 100% with increasing current density. Oxygen crossover was heavily suppressed in the simulation due to the large differential pressure. While this can increase the %LFL, this differential pressure is a strategy for enhancing the H2P, provided that it does not produce dangerous mixtures of hydrogen and oxygen at the anode and that the proper safeguards are in place in case it does occur (J. S. Lopata, et al. 2021a).

Effects of Polarization on Current and Void Fraction.

Figure 4.6 shows the distributions of current density and Figure 4.7 shows anodic and cathodic bubble coverage across the active area of the cell from 1.6 to 2.4 V with a feed rate of 8.10 L min^{-1} per half-cell. As current density increases, it becomes less uniform. The highest current density occurs near the cathode inlet while the lowest occurs near the

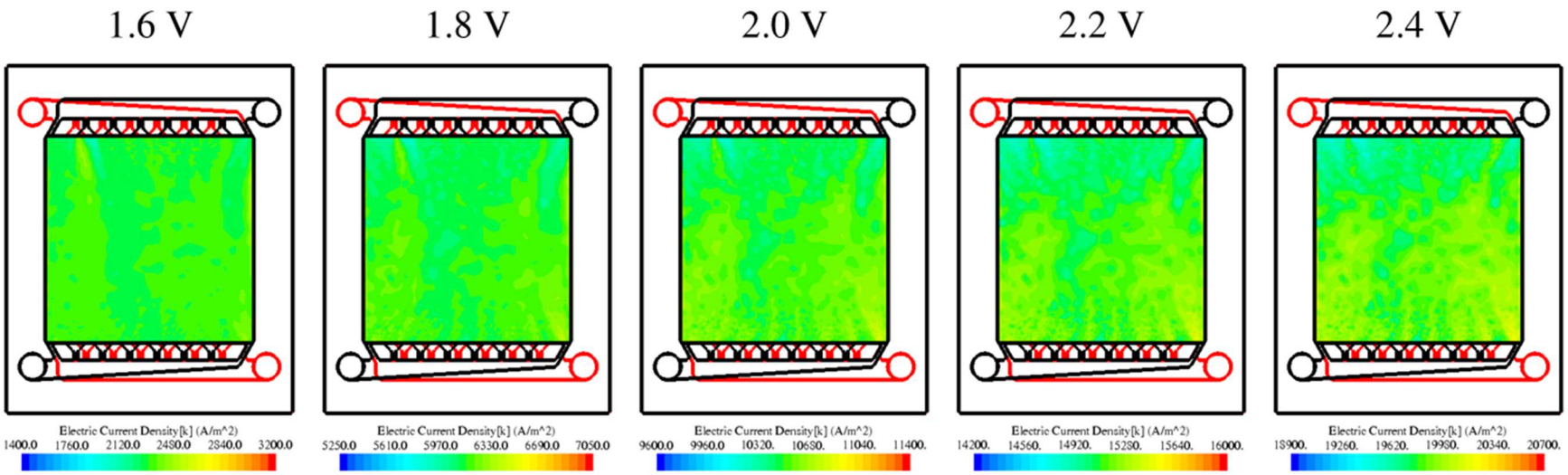

Figure 4.6: Current density distributions for different cell voltages with 8.1 Lpm electrolyte feed per half-cell.

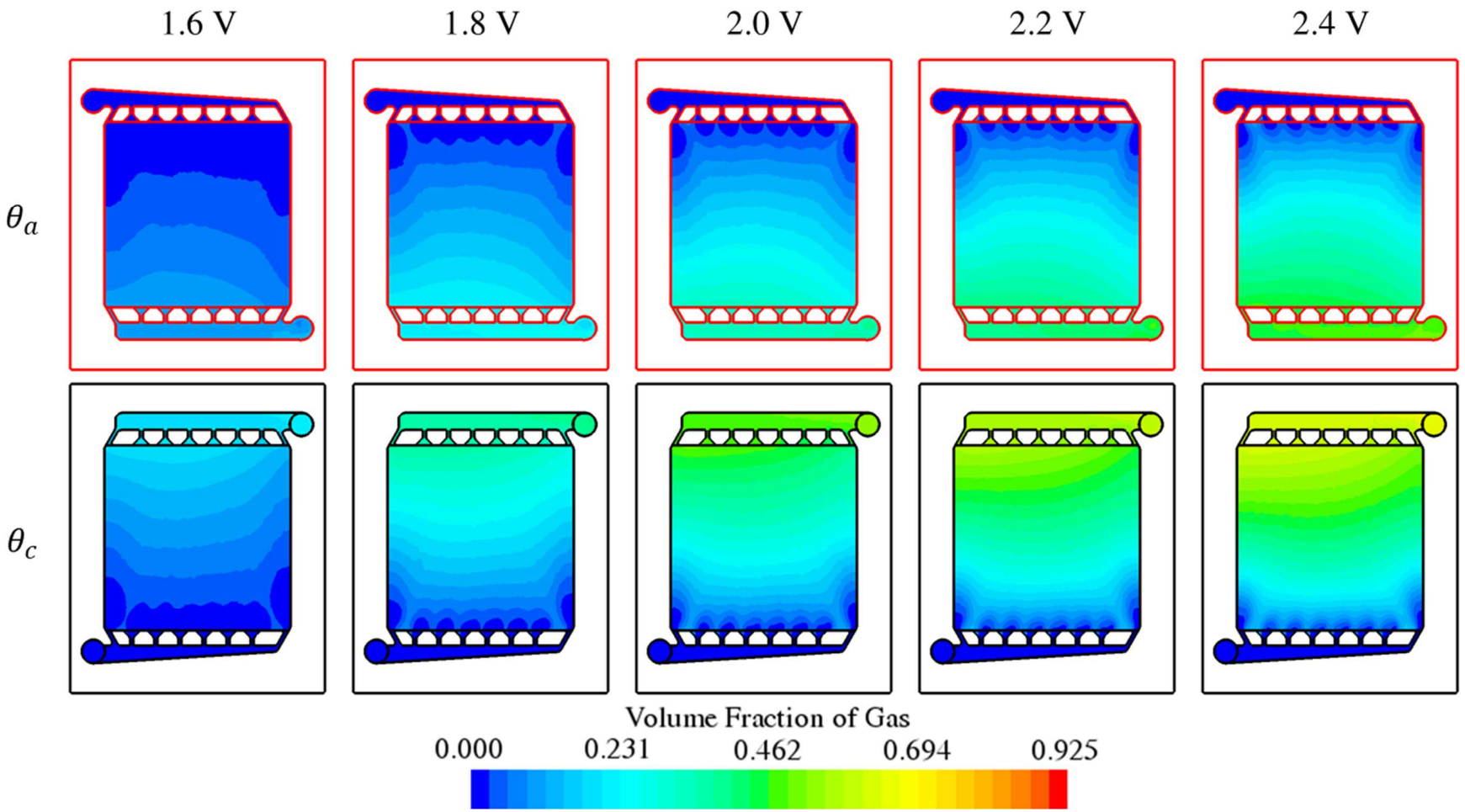

Figure 4.7: Anodic and cathodic void fraction distributions for different cell voltages with 8.1 Lpm electrolyte feed per half-cell.

cathode outlet, especially on the left-hand side far away from the manifold exit. The cathodic void fraction exceeds the anodic due to reaction stoichiometry, so it has a more profound effect on local current density. Void fractions at the anode and cathode reach about 0.4 and 0.6 at 2.4 V, respectively. It is obvious that there exists some nonuniformity in the void fraction distributions at both electrodes, which is attributed to the shape of the manifold channels. This will be analyzed in a later section.

The effect of polarization on the concentration at this high flow rate was minimal, leading to the concentration being nearly constant from inlet to outlet. For this reason, the concentration distributions are not shown.

Effects of Solution Feed Rate on Distributions.

Upon changing the solution feed rate, nonuniformities become more pronounced, as shown in Figures 4.8 and 4.9, the latter of which displays distributions occurring at the lowest feed rate. The local current density at 2.4 V between the inlets and outlets differs by up to 1,800 A m^{-2} at a low feed rate of 2.03 L min^{-1} (C5). This is due to the increase in void fraction at the cathode, once again mostly to the left side. Under C5 operating conditions, the anodic and cathodic void fractions reached approximately 0.8 and 0.9, respectively. The KOH concentration at the cathode reached 8.22 M in the top left corner near the outlet, while the anodic KOH concentration still remained fairly constant. This is attributed to solution crossover. Streaks may be noticed in the concentrations, but these are likely artifacts of needing to correct the ion diffusivity to account for the increase in void fraction, which would otherwise cause the actual concentration to increase up to 10-fold while the superficial concentration remains constant. This is a useful tool for predicting at which feed rates issues would arise in concentration. Higher concentrations hurt cell performance by

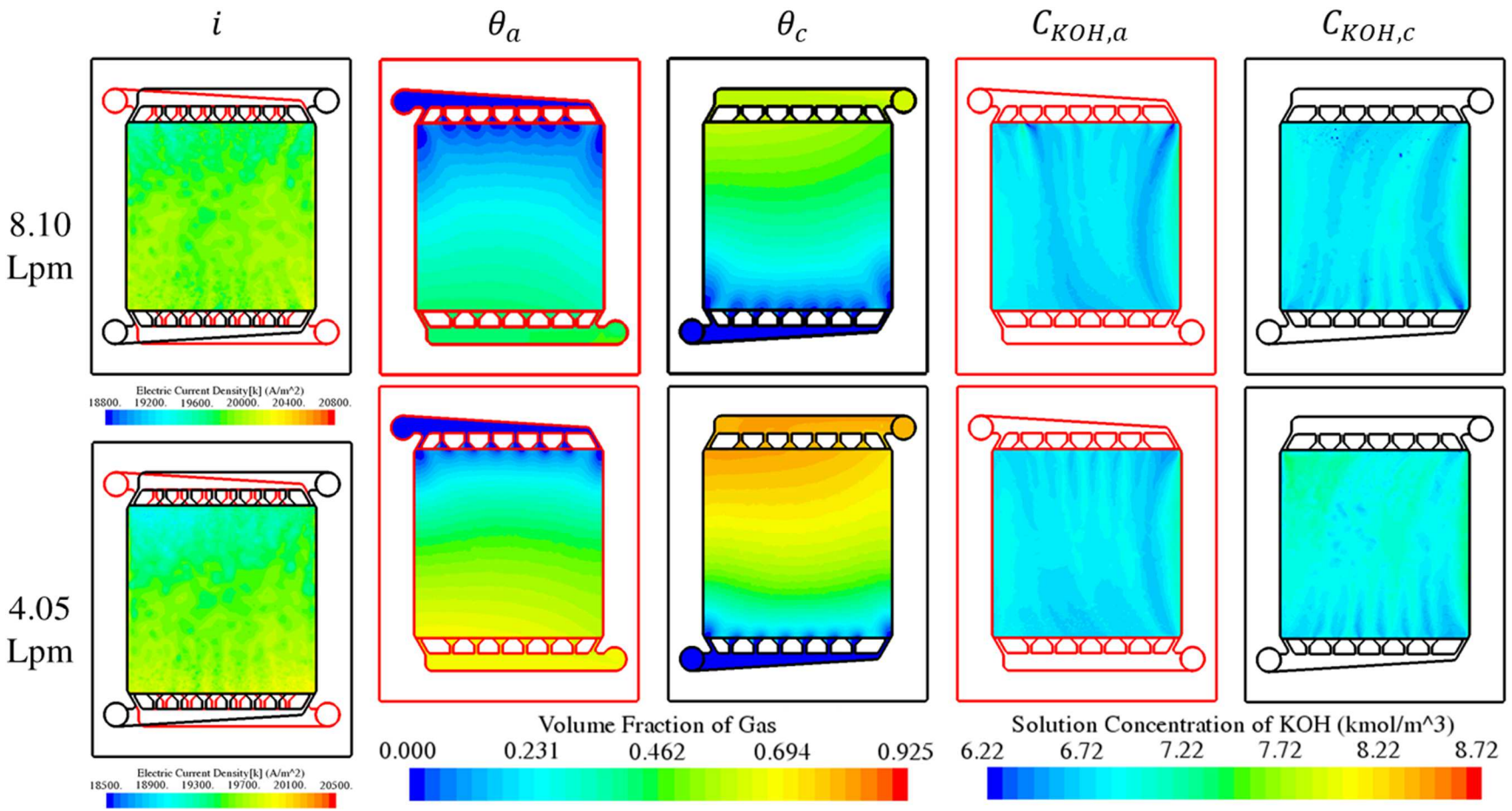

Figure 4.8: Current density, anodic and cathodic void fractions, and anodic and cathodic KOH concentrations for 2.4 V operation at high feed rates. Feed rate are specified in L min-1 per half-cell.

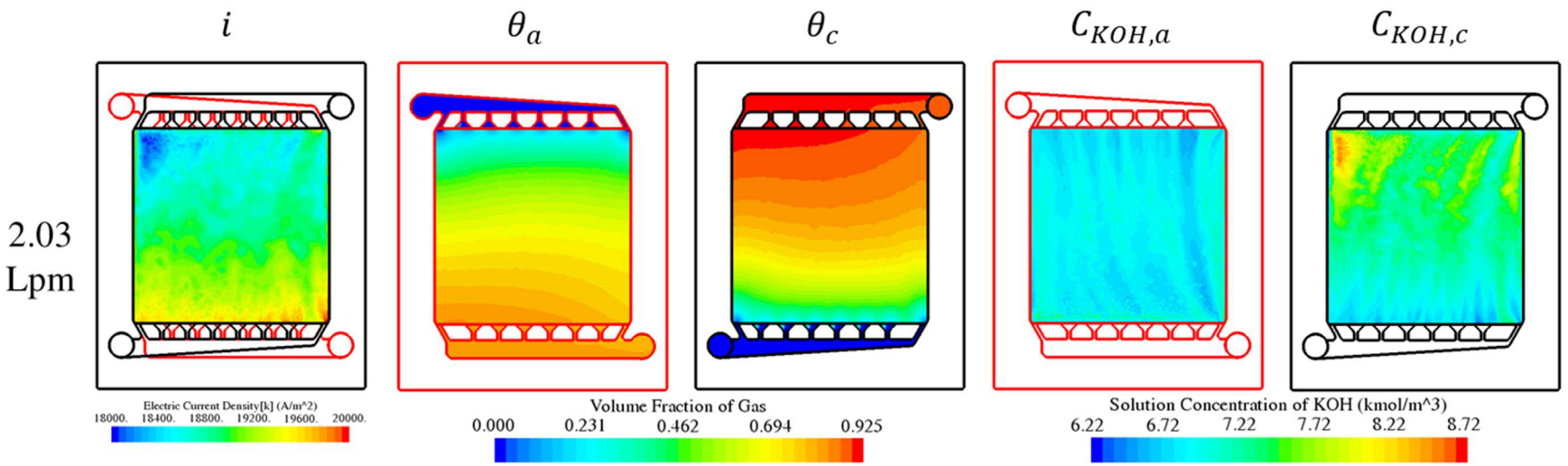

Figure 4.9: Current density, anodic and cathodic void fractions, and anodic and cathodic KOH concentrations at 2.03 L min^{-1} per half-cell.

increasing the effective electrolyte resistance (which was not considered due to the assumption that reactions occurred at the ESI) and decreasing the water activity at the cathode. For that reason, it is best to avoid changes in cathode concentration.

It should be noted that the capillary diffusivity was limited to its minimum value when void fractions exceeded about 0.8. It was kept as is for this study because making the appropriate corrections, i.e. reducing the minimum value and using Equation 2.42 with the modified Leverett function derivative in Equation 2.44, resulted in insignificant changes to the void fraction distribution.

Changes in Crossover Behavior with Operating Conditions.

Three sets of operating conditions were selected to demonstrate the dependence of solution and gas crossover on operating conditions. In this work, hydrogen and oxygen gases were assumed to travel through the separator via two mechanisms: diffusion and convection of dissolved species. Bubbling was not considered due to total pressures being below the bubble point of the Zirfon® separator. Therefore, the local flux of gases depended strongly on the direction of solution flow. Solution transport was governed by liquid pressure drop and electroosmotic drag, which could either be cooperating or competing factors. The liquid pressure was dependent on two factors – the liquid saturation and the feed rate – while electroosmotic drag depended only on current density.

Figure 4.10 shows how the direction of solution flow across the separator is affected by operating conditions. Consider Case A1 operating conditions. The pressure drop from inlet to outlet was high and the current density was very low. Consequently, capillary action and electroosmotic drag contributed minimally to transport. The DLP was influenced primarily by the pressure drops from inlet to outlet as a result of the high solution feed rate.

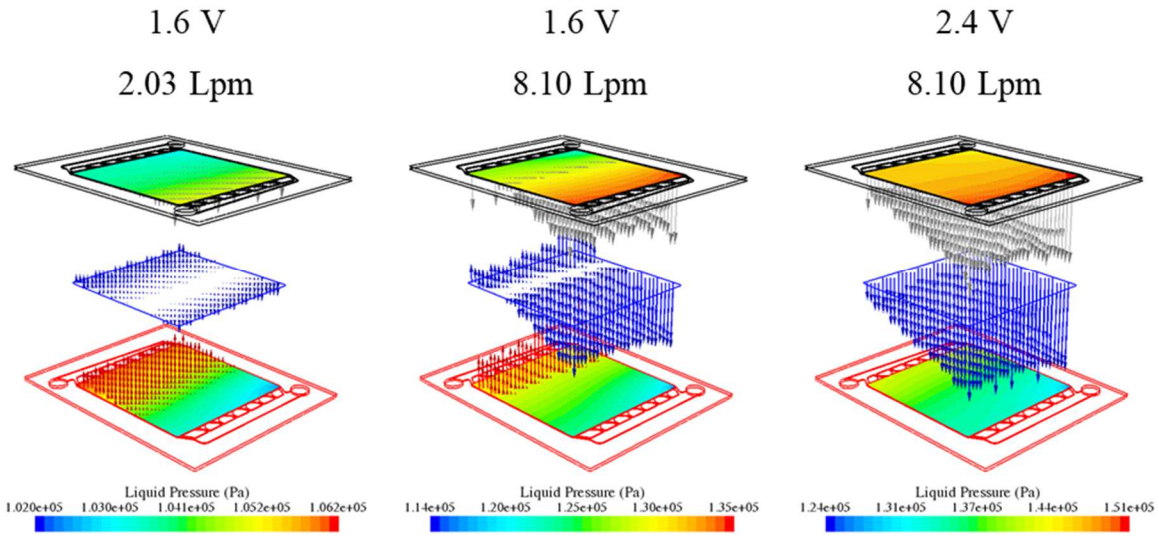

Figure 4.10: Vector diagrams showing the direction and extent of crossover. Included are the KOH solution (blue vectors), hydrogen (gray vectors), and oxygen (red vectors) under three sets of operating conditions. The lengths of vectors representing solution crossover are proportional to the superficial velocity while the lengths of other vectors are proportional to the molar flux of their respective species.

The solution travelled in the +z direction near the anode inlet and the -z direction near the cathode inlet. For Case A5, the high gas evolution rate resulted in higher pressure drops. Again, capillary action was a miniscule factor of DLP compared to pressure drops. Liquid pressure was always higher in the cathode than in the anode despite higher liquid saturations existing in the anode. This was due to the higher volume of gas production in the cathode, the effects of which are more prominent at high current densities. Additionally, electroosmotic drag of water from cathode to anode was a greater factor than in Case A1. Ultimately, solution travelled only in the -z direction. For Case B1, the pressure drops decreased in both sides of the cell due to the lower feed rate, so the magnitude of the DLP decreased significantly. So, while pressure drop was still the dominating factor, DLP became more sensitive to liquid saturation than in Case A1. Unlike Case A1, there is no obvious bias in solution flow from cathode to anode in Case B1.

Figure 4.10 also shows the effect of solution transport on gas crossover. Gas generally travelled in the same direction as the solution unless the solution velocity was very low. In Case A5, oxygen crossover was completely suppressed due to the strong convection of solution from cathode to anode at all locations. At low solution velocity, diffusion flux could dominate over opposing convection flux. Note that oxygen crossover in Case B1 occurs over a larger area, with diffusion being the more prominent transport mechanism in relatively stagnant solution in the middle of the cell. At all cell potentials and flow rates, oxygen crossover was more prominent if the solution moved in the +z direction, while hydrogen crossover was more prominent if the solution moved in the -z direction. In light of this, gas crossover was moderated by limiting convective transport through the separator, as seen when comparing Cases A1 and B1.

Influence of Geometry on Void Fraction, Concentration, and Current.

The major advantage of 3D modeling is that local variations in variables, some of which may be undesired, can be linked to an aspect of the design. In Figure 4.11a, the current density reduction near the cathode outlet is diagnosed. Earlier, this was attributed to the high volume fraction of hydrogen gas in that region. This is referred to as the "direct cause" in Figure 4.11a. The pressure distribution and in-plane velocity vectors allow us to examine the "root cause" of the high void fraction. There is clearly a path of least resistance within which fluid flows toward the outlet, causing an asymmetric velocity profile. The low fluid velocity in the problem region is allowing higher void fractions. This can be resolved by changing the geometry of the outlet manifolds, possibly by restricting channels closer to the outlet and expanding channels far from the outlet. Bear in mind that adding a turbulence model may affect the computed flow distribution by increasing the local effective viscosity in regions of the manifolds with high fluid velocities. Geometry effects on local crossover can also be seen. Figure 4.11b illustrates a diagnostics procedure similar to that in Figure 4.11a. Problem areas, i.e., areas with high liquid velocity magnitudes leading to high gas crossover, are identified. Then, the local liquid pressure distributions are plotted to show that the DLP across the separator was at extremes in these problem areas. The problem areas arise when inlet and outlet manifold channels overlap, leading to large differences in liquid saturation across the separator. This can be resolved by ensuring that there are no overlaps if possible. Of course, if gas crossover were insignificant, there would be no need to make corrective actions.

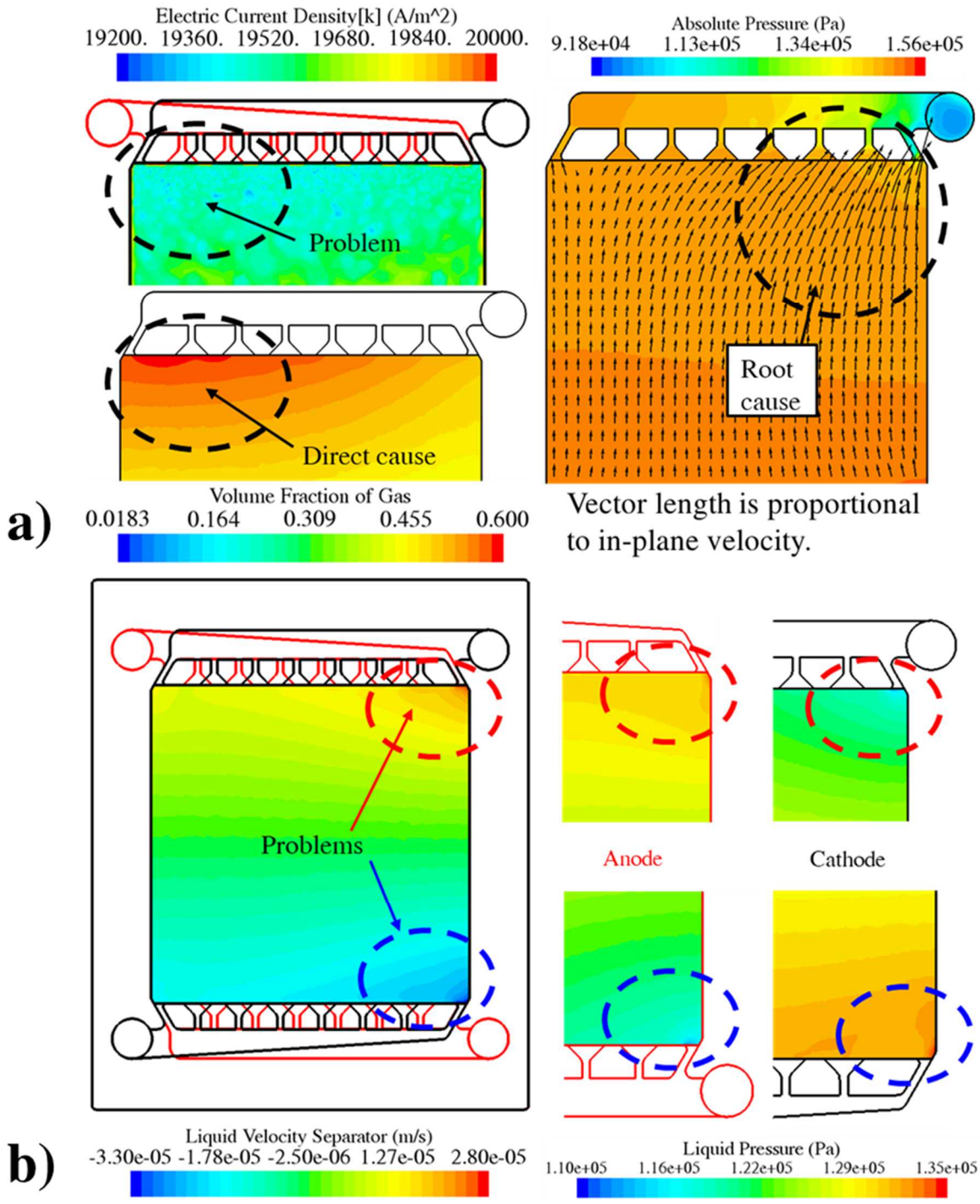

Figure 4.11: Diagnostic analysis of low local current density and extent of crossover. a) There was a problem area with low current density due to high void fraction. The root cause was determined to be associated with the flow distribution, which led to stagnation of flow within the problem area. b) Some geometric features led to increased electrolyte velocity, i.e., local crossover, in the designated problem areas. The problem areas are color-coded for ease of correlation. Liquid pressure differentials, shown on the right, were found to exist at extrema in the problem areas. (J. S. Lopata, et al. 2021a)

Tuning Feed Rates and Separator Properties to Improve Cell Performance.

It is obvious that the void fraction in the cathode porous media is significantly higher than at the anode because a greater volume of hydrogen than oxygen is produced. Because this variable is sensitive to feed rate, the intuitive course of action would be to increase the feed rate to the cathode in order to drive the hydrogen out. The inlet feed rate to the anode was reduced by 25% and the cathode feed rate was increased by the same magnitude to maintain a similar total feed rate. The results of this simulation trial are shown in Figure 4.12. The current distribution for balanced flow rates is compared to the outcome of off-balancing the feed rate to the cathode at 2.4 V. Off-balancing feed rate causes current to increase near the outlet at the cathode, which is demonstrated in Figure 4.12 as being due to the reduction in void fraction. Void fraction increases at the anode, but the current density is more uniform and the overall current density increased from 19,545 to 19,624 A m^{-2}. The concentration also becomes highly uniform. The pocket of high concentration near the cathode outlet is diminished because the electrolyte is flowing more swiftly.

Solution flow through the separator was assumed to be dominated by electroosmotic drag from cathode to anode, with an effective electroosmotic coefficient of 0.7 (Haverkort 2020). A hypothetical case was tested in which electroosmotic flow dominates solution crossover, with an effective electroosmotic coefficient of -0.7, which could perhaps occur if the zeta potential was sufficiently high. This resulted in more solution crossover from anode to cathode, having an effect similar to off-balancing the feed rates, namely an increase in current density at the cathode outlet. Figure 4.13 contains the results for the change in the electroosmotic properties of the separator. Similarly to the

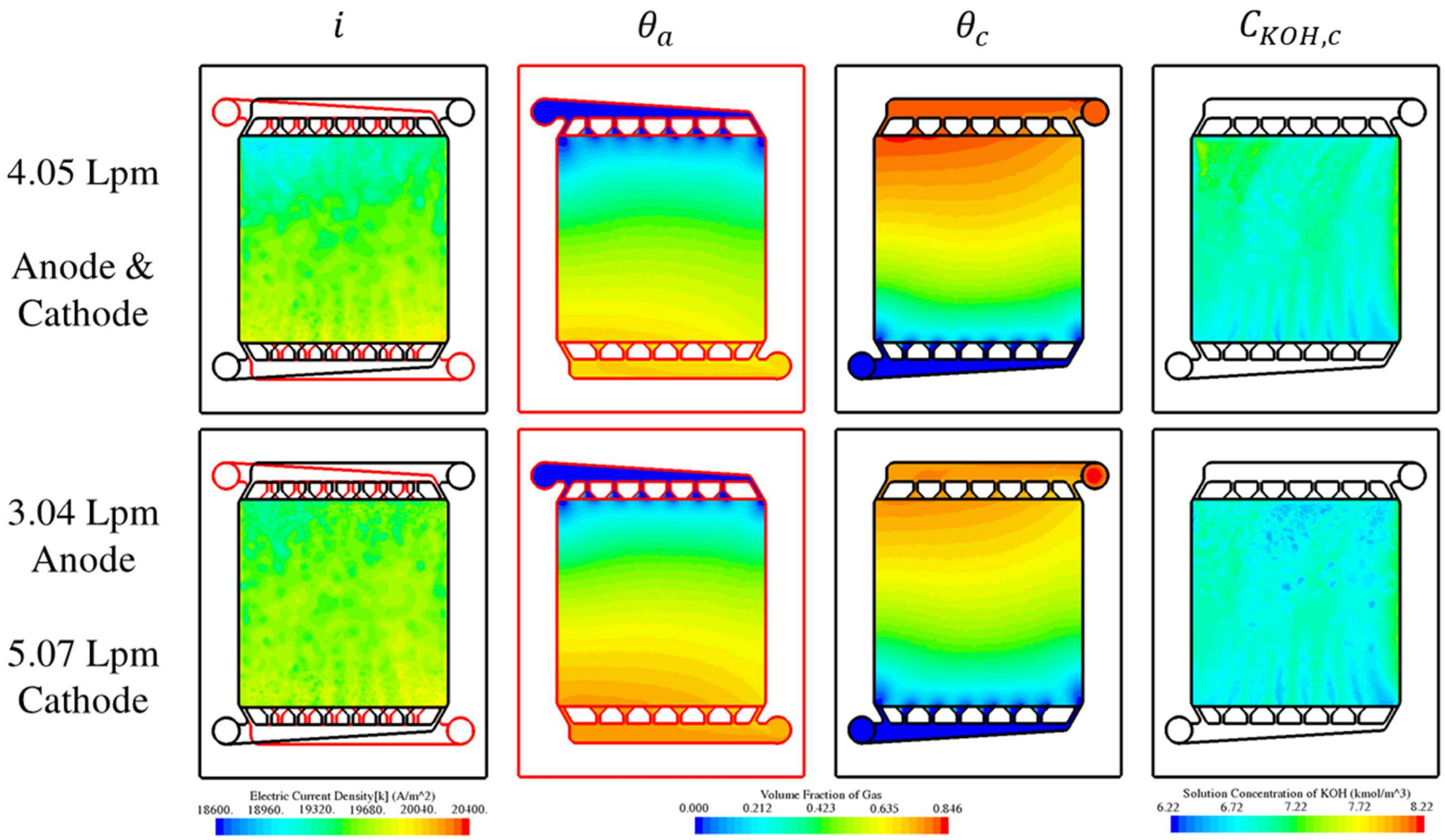

Figure 4.12: Effect of offsetting the feed rates on current, void fraction, and cathodic concentration distributions at 2.4 V.

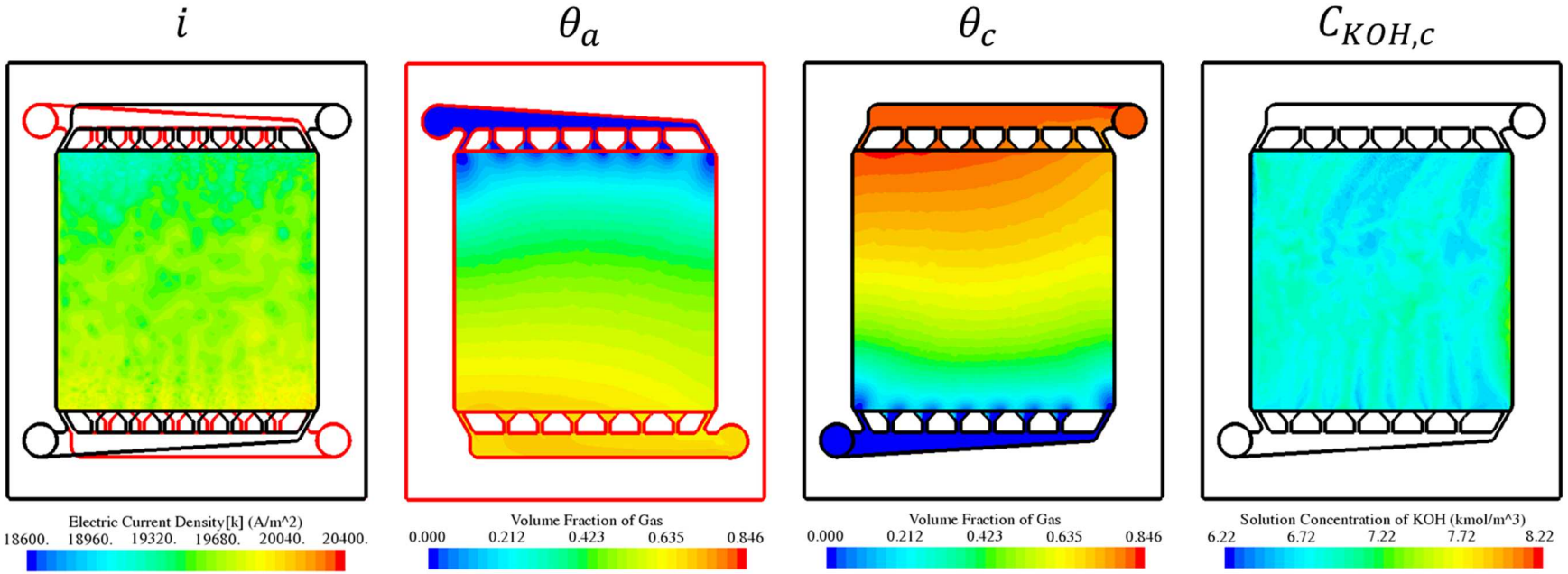

Figure 4.13: Current, anodic and cathodic void fraction, and cathodic concentration distributions at 2.4 V with balanced feed rates of 4.05 L min^{-1} to each electrode, with electroosmotic-flow-dominant behavior in the separator.

previous case, the concentration near the cathode outlet decreased to make the distribution more uniform.

Considerations for Alkaline Electrolysis Stacks.

A stack of five ADWE cells was simulated using the same P2PM model. The finite volume mesh, shown in Figure 4.14, contained 15,054,834 control volumes. A constant temperature of 80 °C was applied to the CCs at the two ends and an adiabatic condition was set for the other external boundaries. The purpose was to investigate whether there were significant non-uniformities through the stack or if they would arise in larger stacks containing more cells. Additionally, the shunt currents through manifolds were resolved to understand where they are most prominent so that this insight could be utilized to design manifolds that better hamper shunt currents.

Through-Stack Current and Temperature Profiles.

Figure 4.15 summarizes the current and temperature profiles through the stack under S-A5, S-B5, and S-C5 operating conditions. Figure 4.15a shows the average current density within each cell of the stack, the lowest of which exists in the center cell due to shunt current, despite higher temperature. The temperature distributions from inlet to outlet through each cell are compared among three different electrolyte feed rates in Figure 4.15b. When the feed rate is reduced, less heat is carried by the fluid to the outlet, so the temperature rises. Heat is generated within each cell primarily by the resistance of the separator and ESIs as well as the cathodic reaction.

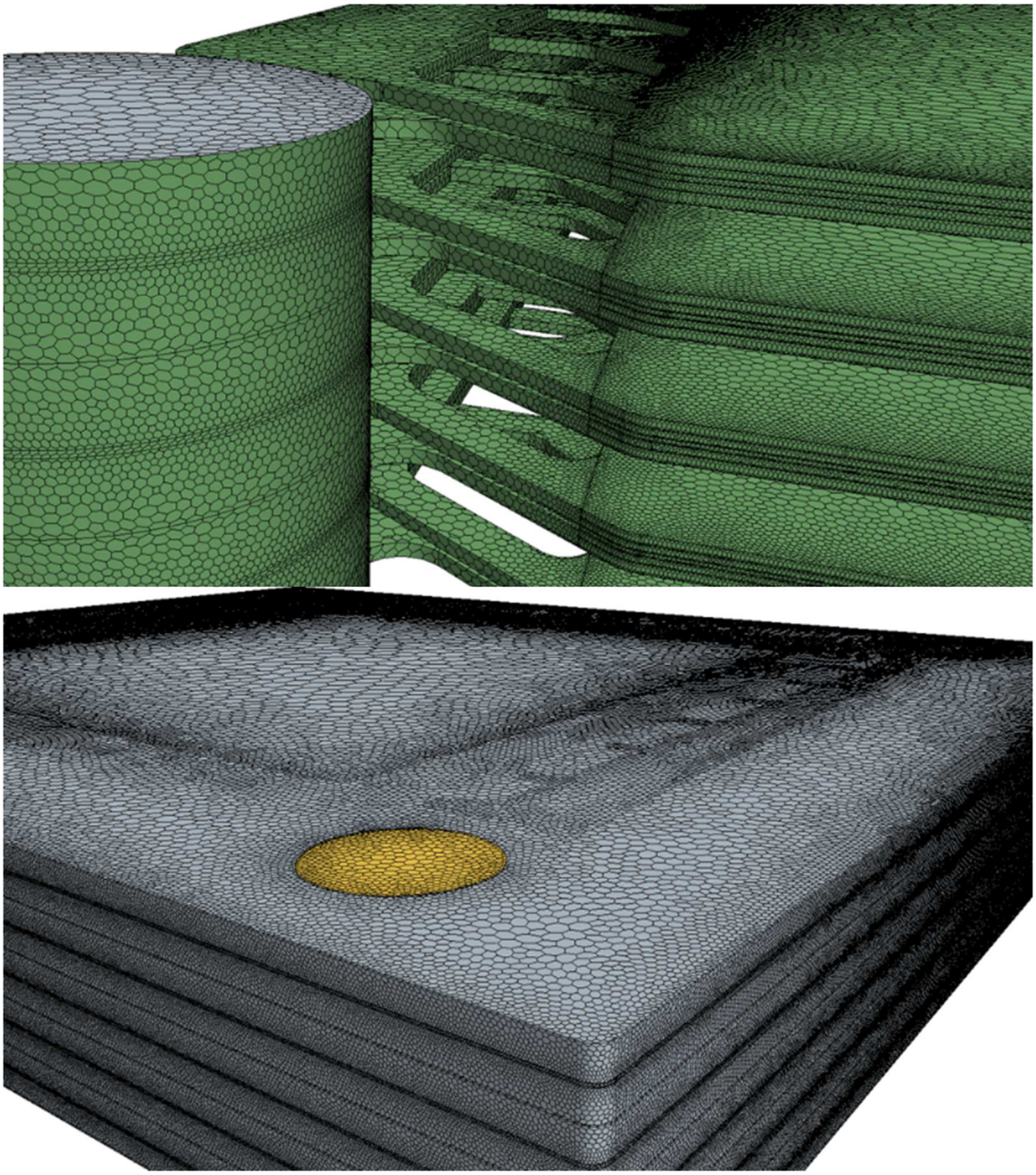

Figure 4.14: Mesh of the manifolds, internals, and plates of the 5-cell ADWE stack.

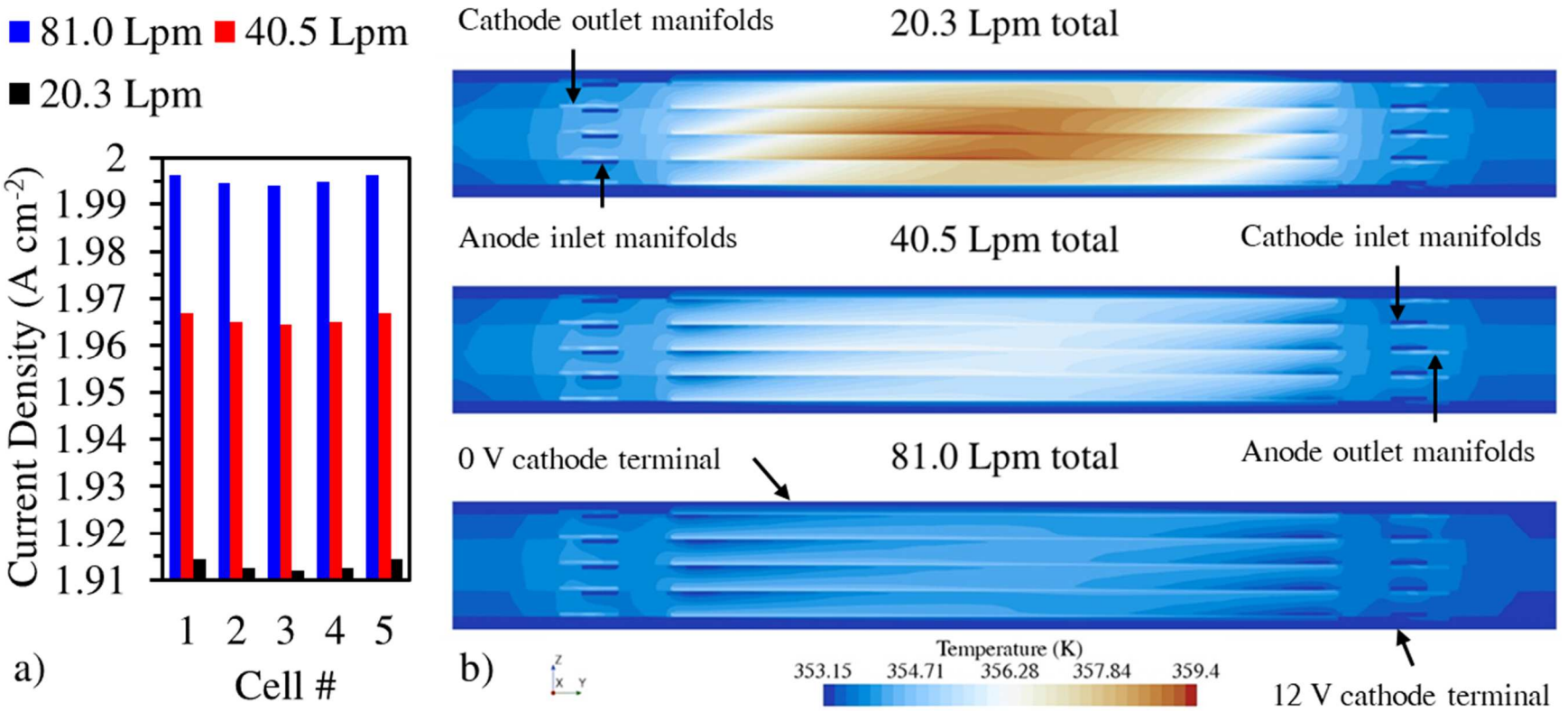

Figure 4.15: Through-stack profiles and along-channel temperature distributions at 12 V operation with a setpoint temperature of 80 °C. a) Average current densities among the 5 cells at the three studied electrolyte feed rates. b) Temperature distribution within a plane section along the channels from inlets to outlets at the three studied feed rates. The locations of inlet and outlet manifolds as well as the locations of the two terminals are labeled.

Current and Void Fraction Distributions Through the Stack.

The current and void fraction distributions are highly uniform throughout the stack, despite the considerable temperature distribution. This is shown in Figure 4.16. The center cell has the lowest current, which at a low total feed rate of 20 mL min^{-1} is still less than 25 A m^{-2} less than that of the outer cells. No clear trend exists in the void fractions through the stack. From this result, the stack can likely be designed under the assumption that the current distributions are similar for every cell. The result for the current density of a single cell can be used to calculate the heat generation distribution at each electrode in a stack geometry. In this way, temperature distributions and local shunt currents can likely be approximated adequately without extreme computational power.

Shunt Current Through the Manifolds.

In Figure 4.17a, shunt current is displayed throughout the manifolds of the ADWE stack. The highest shunt currents form in the tributary manifolds near the mains in the end cells. The shunt current does not significantly impact current distributions, but corrosion can be expected to occur most rapidly in these high-current locations. Figure 4.17b reports shunt current distributions for the manifold mains and tributaries, which qualitatively agree with literature (White, et al. 1986).

Conclusion

The work of this chapter extended the use of the P2PM model to ADWE applications after demonstrating an ability to provide information about fluid flow within manifolds and flow field channels. ADWE cell performance is highly dependent on solution feed rate, with higher feed rates being more beneficial by limiting the void fraction. The geometry of the ADWE manifolds was found to influence the flow

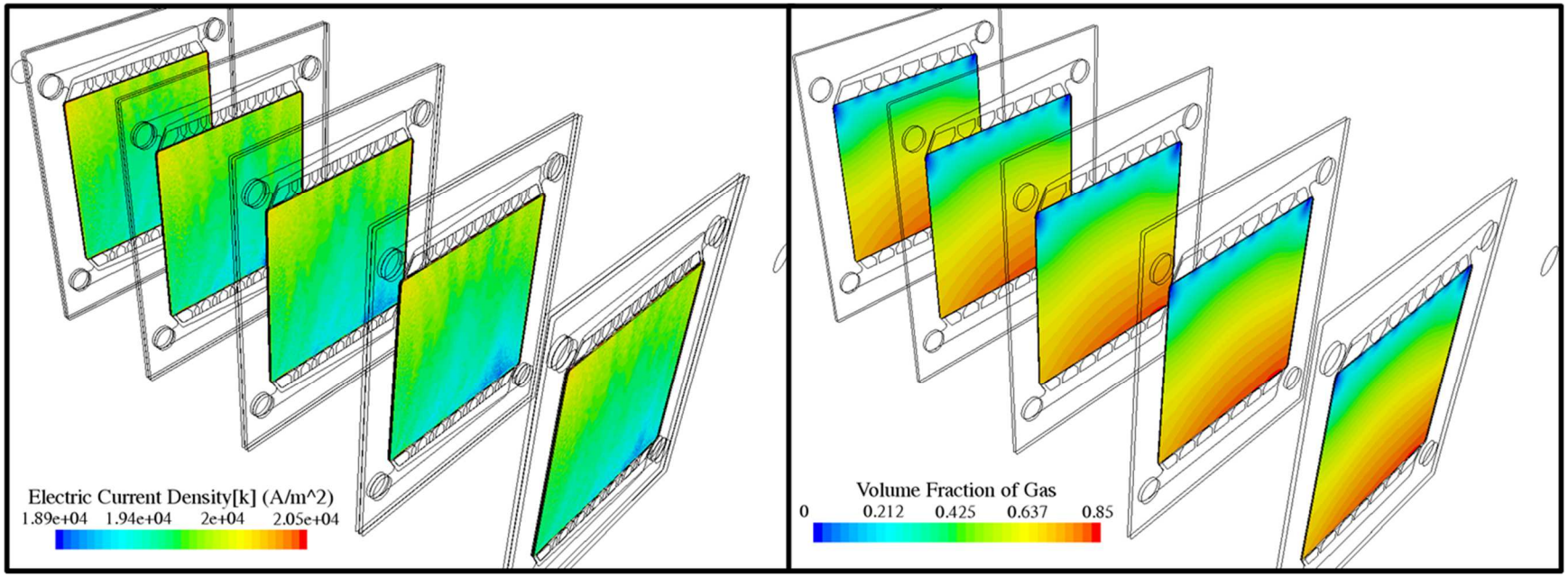

Figure 4.16: Current density and cathodic void fraction distributions throughout the five-cell stack with a total electrolyte feed of 40.5 L min^{-1}.

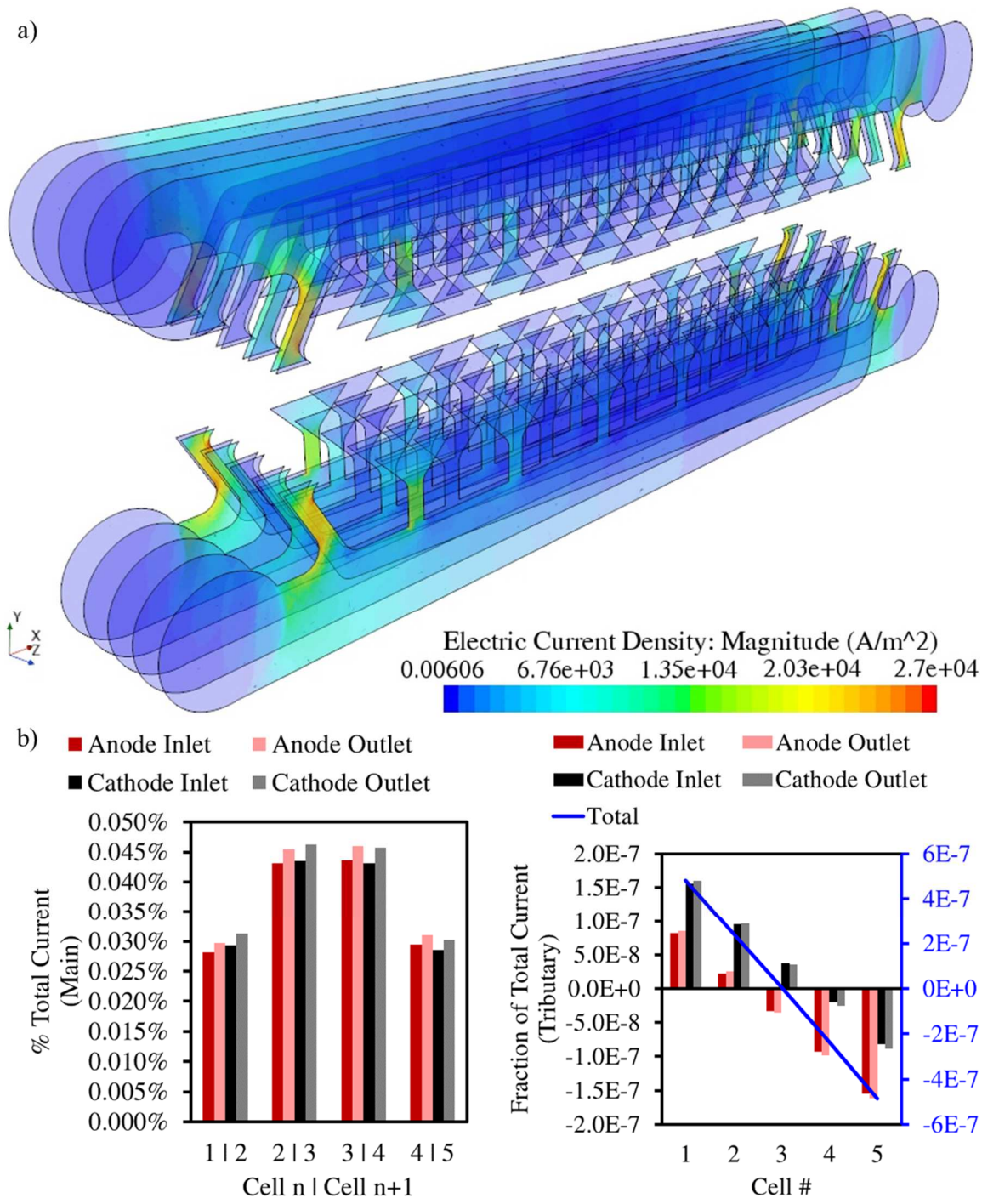

Figure 4.17: Shunt current in the ADWE stack at 2.4 V with a total electrolyte feed of 40.5 L min^{-1}.

distribution of the fluid within the porous media. Non-uniformity in fluid velocity led to locations within the cell, specifically near the cathode outlet, that were more susceptible to higher void fractions and concentrations. Without altering the geometry, diverting some solution feed from the anode to the cathode mitigated this effect while slightly improving overall cell performance. It was demonstrated that solution transport through the separator influenced concentrations at the electrodes by switching crossover from electroosmotic-drag-dominant to electroosmotic-flow-dominant, the latter of which made cathode concentration more uniform at the cathode. Equalizing pressures across the diaphragm prevents high levels of hydrogen crossover, but little to no impact on overall performance. It may be best to run higher cathode pressures to ensure high hydrogen purity while taking care not to permit unsafe hydrogen partial pressure at the anode.

A five-cell stack was simulated in order to determine whether there were significant differences in current density, void fraction, or temperature among cells withing the stack. The highest temperatures were located near the cathode outlet of the center cell while the lowest temperatures were found at the outlet of the leftmost anode. The 3D geometry permitted the computation of shunt current distributions within the manifolds and showed that the highest shunt currents existed in the manifold tributaries of the outermost cells near the manifold mains. Modeling the 3D geometry allows one to predict the highest local shunt currents, which may assist engineers in estimating the lifespan of the CC plates prior to degradation testing.

CHAPTER 5

RESISTANCE AT THE ELECTRODE/SEPARATOR INTERFACE

Introduction

Transport phenomena at the ESI have significant influence on the performance of a PEMWE or ADWE device. Chapter 1 explained the ways in which the presence of the gas phase increases the resistance or surface overpotentials by reducing ion-transport area or electroactive area. This chapter discusses results of experiments and proposes models that provide much information about how to design the ESI by tuning porous media properties. In the discussion, the consequences of high void fractions are generalized in order to apply to both PEMWE and ADWE cells. ESI potential loss mechanisms differ between the two technologies, but they are often analogous and can be categorized.

Insight from PEMWE Experiments

Experiments performed on PEMWE devices demonstrated how properties of the PTL surface in contact with the CL affect both electronic resistance and mass transport limitations. The extent to which the performance of the cell is sensitive to these PTL surface properties depends on the catalyst loading. Figure 5.1 depicts the occurrences that likely arise within the CL in both the pore opening regions and the region between the PTL grain and the membrane. Water is drawn into the CL by capillary forces engendered by oxygen production. If the CL is very thin, there will be high in-plane resistance and catalyst utilization will be low near the PTL pores. Additionally, gas may become trapped between

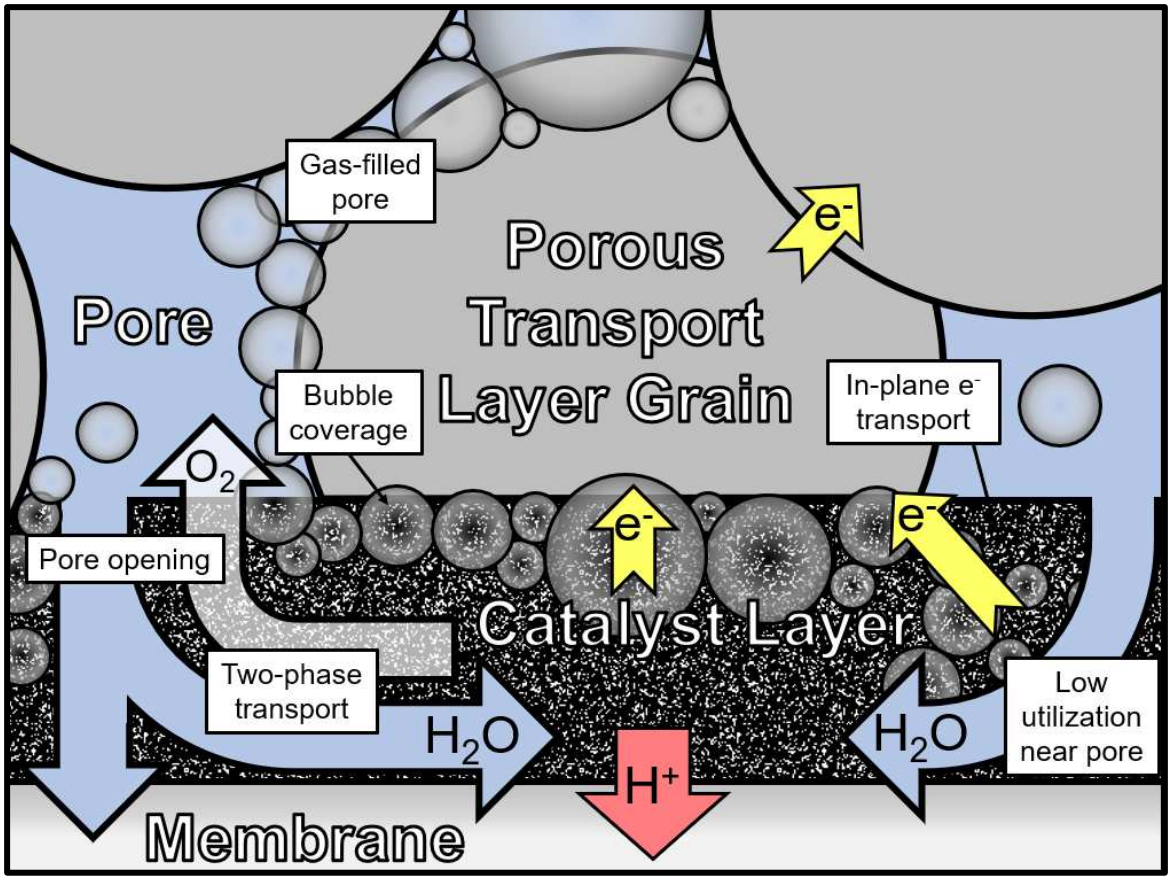

Figure 5.1: Cartoon describing transport phenomena in the CL at the interface between the PTL and the CL at the anode of a PEMWE device (J. Lopata, et al. 2020).

the PTL grain and the membrane. If this happens to a sufficient extent, it may lead to kinetics limitations and/or increased ionomer resistance.

Porous Transport Layer Selection.

Three PTLs (Edgetech Industries, LLC) of varying average pore opening diameter (APOD) and average grain surface diameter (AGSD) were selected for PEMWE experiments at different catalyst loadings and temperatures. Table 5.1 compiles properties of the three materials. Images of the surfaces, captured with a Leica DM-6000M optical microscope, are provided in Figure 5.2. Direct (normal) incident lighting intensity was adjusted to yield the best contrast between the grain surfaces and pore openings. Using the Fiji distribution of the ImageJ image processing software, the APOD and AGSD were extracted from the images. First, the photograph images were modified with a Gaussian blur to reduce the roughness of the exterior surfaces and filter out small, illuminated, intraporous surfaces while maintaining image integrity, i.e. preventing translations of the pore opening edges. Next, a threshold was applied to produce a black and white representation of the PTL surface, with the pore space represented by the white region and the grain surfaces represented by the black region. The ImageJ local thickness operation was applied to the two separate regions of the image to obtain the APOD and AGSD. PTL preparation was carried out in the manner described in Chapter 3 (J. Lopata, et al. 2020).

Reduction of Catalyst Loading at the Anode.

One cost cutting measure that is pursued in the effort to make water electrolysis more economical is the reduction of catalyst loading. Iridium- and platinum-based materials are scarce and expensive, so the ability to reduce the use of such catalysts can reduce the fixed costs associated with the construction of an electrolysis cell. Reducing

Table 5.1: PTL Properties

PTL ID	Porosity	Permeability (m^2)	APOD (μm)	AGSD (μm)
PTL1	0.302	5.35e-13	33	14
PTL2	0.312	1.10e-12	94	31
PTL3	0.218	3.2e-13	160	67

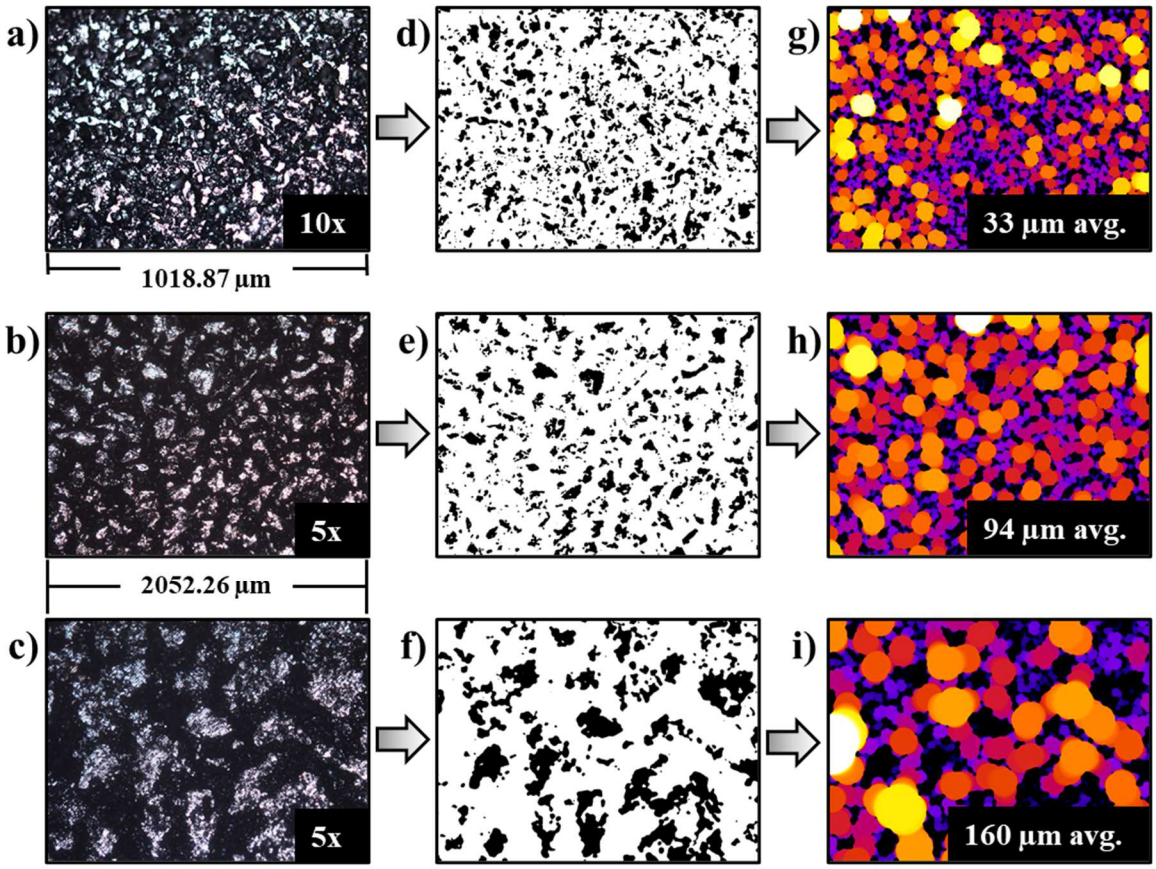

Figure 5.2: Depiction of the image processing used to obtain the average pore opening diameter on the surface of the PTLs in contact with the anode during the experiments. The microscope photographs are shown in a), b), and c), the thresholded images are shown in d), e), and f), and the images depicting the local thickness analysis are shown in g), h), and i). Note that the shading in images g) through i) cannot be compared with each other because the shading scale is relative (J. Lopata, et al. 2020).

catalyst loading without considering other design aspects, however, has the effect in increasing the cell potential required for hydrogen production, which in turn leads to higher variable cost associated with electrical power consumption. Thus, some optimal catalyst loading is required to maximize the profit of operating an electrolysis cell. The following set of experiments were performed in order to understand the mechanisms through which PTL surface properties reduce performance and to demonstrate that optimal catalyst loading is a function of PTL surface properties.

The anode catalyst loading was approximately 0.085 ± 0.012 mg Ir cm^{-2} and 0.595 ± 0.022 mg Ir cm^{-2} for low- and high-loaded samples, respectively. The error reported with these values are two times the standard deviation. The cathode loading amounts were respectively 0.280 ± 0.010 mg Pt cm^{-2} and 0.382 ± 0.018 mg Pt cm^{-2} . While it was desired to use identical cathode loadings, the contribution of the cathodic reaction was assumed to be negligible when determining the kinetics parameters for the CCMs. This assumption was based on the fast kinetics of the hydrogen evolution reaction at the cathode, the lack of mass-transport limitations, and the very high electrical conductivity of the carbon support when compared to that of IrO_2. Minor changes in cathode loading were therefore not expected to have any impact on the achieved results. If it indeed impacted performance, it would not have explained the change in sensitivity of the cell performance with catalyst loading, which was the objective of the study (J. Lopata, et al. 2020).

Effects of Porous Media Properties on Performance.

Imagine a container with two sides separated by a gate, one side containing liquid and the other containing air. When the gate is lifted slightly, liquid flows under the gate to the other side of the container, displacing air. The rate of flow can be altered by raising or

lowering the gate because there is less resistance to flow when the cross-section beneath the gate is wide rather than thin. This is one way to picture the transport of electrons and fluids in-plane within a CL, which can have varying thickness depending on catalyst loading. The A-OER can occur only if the following conditions are met: 1) Liquid water and water vapor are able to flow or diffuse to the catalyst surface, 2) Electrons are able to transfer from the chemical bonds in water to the conductive electrocatalyst, 3) Protons can transfer from the catalyst surface to the ionomer electrolyte matrix, 4) Oxygen gas is able to escape the reaction area. All four conditions are easily met, provided sufficient liquid feed, at the pore opening edges, as it is there that reaction sites are nearest to both incoming water and the conductive PTL grain, meaning that neither electrons nor species must travel through the figurative narrow gate that is the in-plane cross section of the CL. Within the CL, adjacent to the pore opening, electrons must travel in-plane from the reaction site to the PTL grain. Because the conductive CL is a thin sheet, there may be a significant electronic resistance associated with it, especially if the catalyst loading is low.

Overall Performance Evaluation.

Figure 5.3 shows as-measured and HFR-corrected steady state polarization curves as well as the equilibrium and resistance overpotentials. Cell performances using PTLs with APODs of 33, 94, and 160 μm and CCMs with catalyst loadings of 0.085 and 0.595 mg Ir cm^{-2} at temperatures of 35 and 55 °C are juxtaposed. A flow rate of 20 mL min^{-1} cm^{-2} was used in these experiments, which minimized the temperature variation along the channels. At potentials of 1.9 V and below, the inlet to outlet temperature differential typically remained below 0.5 °C. However, a slight decrease in the HFR with increasing current density was consistently observed. It is likely that the membrane temperature

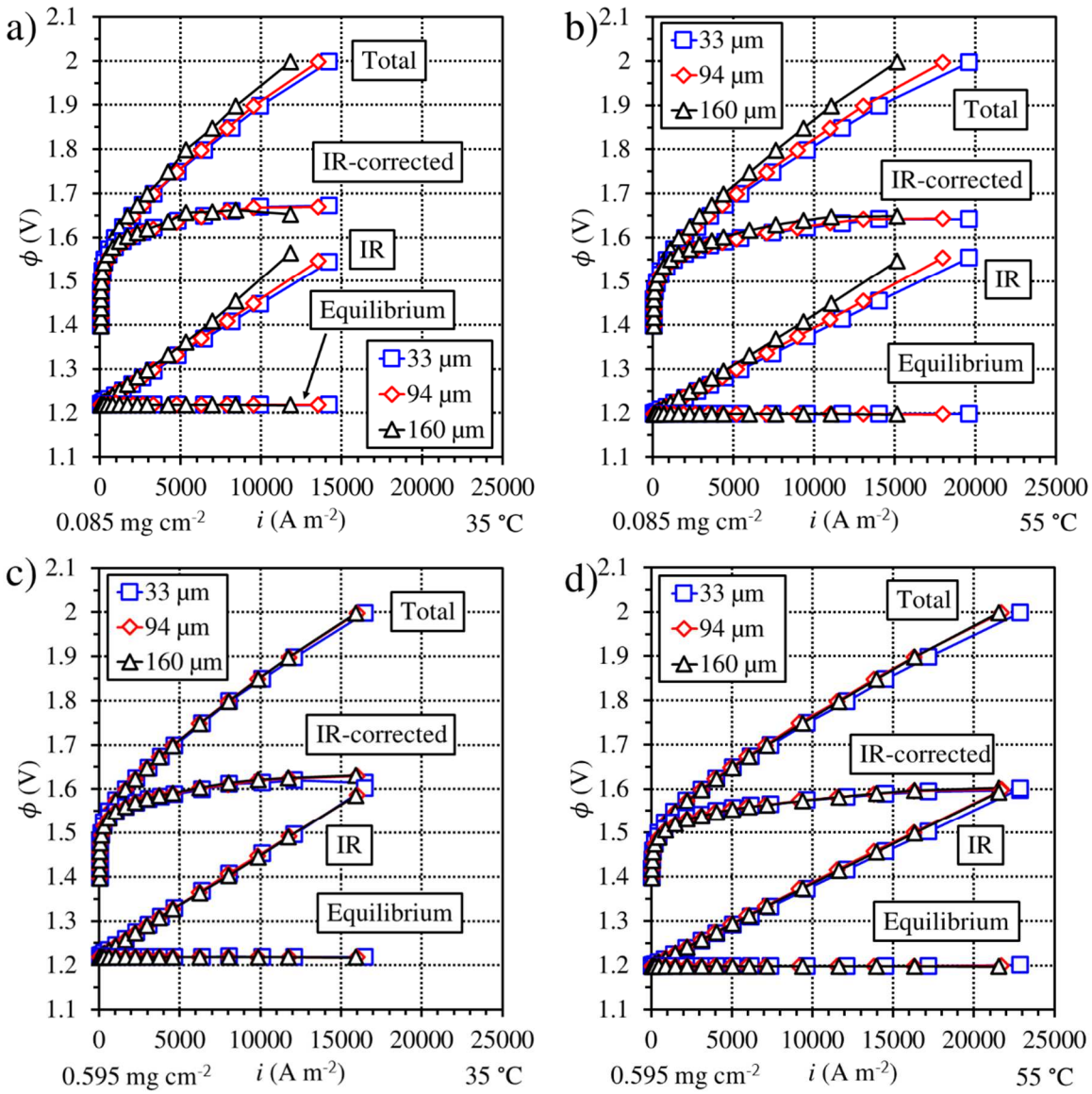

Figure 5.3: Polarization curves and accompanying components of cell potential using PTLs with pore opening diameters of 33, 94, and 160 µm at different IrO_2 loadings and temperatures under wet/wet operation with 80 mL min^{-1} liquid water feed to each electrode.

increased slightly during high-current operation, increasing its conductivity. However, it is possible for a decrease in CL ionomer conductivity to go unnoticed, if localized drying does occur in the CL.

The most notable detail of these results is the performance loss that occurred with an increase in the APOD at a catalyst loading of 0.085 mg Ir cm^{-2}, shown in Figure 5.3a and 5.3b. From Figure 5.3c and 5.3d, it is apparent that the impact of the APOD on cell performance was reduced at a higher loading of 0.595 mg Ir cm^{-2}. The ohmic overpotential was the largest factor leading to performance differences among PTLs. The HFR of the cell as a function of current density at different temperatures and catalyst loadings is provided in Figure 5.4. Generally, the HFR decreased with increasing current density because of higher ohmic heat generation in the membrane, as HFR increases with temperature. Some experiments were marked with an increase in HFR with increased current density. This always occurred when the catalyst loading was low, and the trend was more pronounced when a larger pore opening size was used. It is evidenced by the work of others (Schuler, Schmidt and Büchi 2019) that membranes swell into the pores and larger pores allow more swelling. This not only increases the effective thickness of the membrane but adds stress to the CL, which can fracture. Membrane swelling appeared to have a greater effect on the thinner CL, which has lower in-plane conductance. Low in-plane conductance was the reason that the difference in HFR among APODs was more severe at low loading than at high loading. Resistance overpotential was not the only overpotential impacted by the PTL surfaces. The residual overpotential, which is labeled a mass transport overpotential in Figure 5.4, also increased significantly with increasing current density, larger APOD, and reduced catalyst loading. Temperature had little to no impact on mass transport

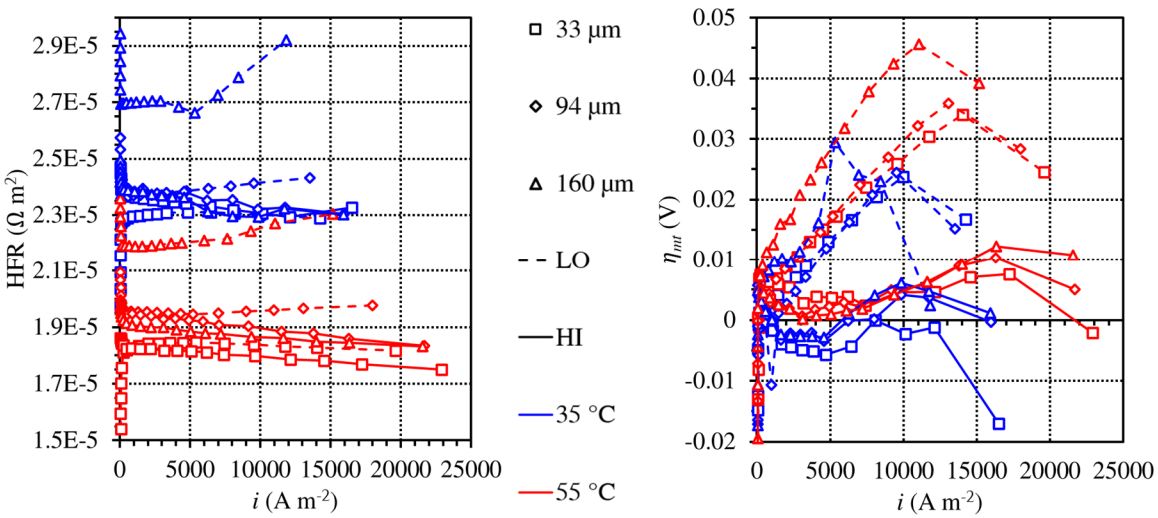

Figure 5.4: Change in high-frequency resistance and mass transport overpotential with current density for the three different average pore opening diameters used in experiments and catalyst loadings of 0.085 mg Ir cm^{-2} (LO) and 0.595 mg Ir cm^{-2} (HI) at 35 °C and 55 °C.

overpotential. The decrease in mass transport overpotential at the highest current density in each dataset was probably due to the cell not reaching steady state at 2.0 V. 2.0 V was treated as a maximum potential setpoint in order to protect the cell components while testing different combinations of membrane-electrode assemblies (MEAs) and PTLs. The cell was held for 30 min at 2.0 V prior to down-stepping the potential, which was the reason that steady-state was reached potentiostatically at lower potentials thereafter. At 55 °C with a loading of 0.085 mg Ir cm^{-2}, the resistance overpotential with an APOD of 160 μm was about 60 mV higher than with an APOD of 33 μm at about 12,000 A m^{-2}. Figure 5.4 shows that an increase in mass transport overpotential among the same materials was approximately equal to about a quarter of this value. Furthermore, at 55 °C with an APOD of 33 μm, the increase in resistance overpotential from high to low catalyst loading was about 10 mV at 15,000 A m^{-2} while the increase in mass transport overpotential was about 25 mV at the same current density. Here, evidence exists that depending on the properties of the PTL surface and CL, mass transport is considerable enough that it should be considered in design, especially in attempts to reduce catalyst loading. In some cases, the effect of mass transport exceeds that of in-plane electron transport in the CL.

Mass transport limitations make themselves obvious in Tafel plots through non-linearity at high current density. In Figure 5.5, Tafel plots are shown at 35 and 55°C with the two catalyst loadings and three PTLs studied. The dashed lines are fits of this data using the sum of a Tafel term for anodic overpotential and an apparent resistance overpotential term associated with mass transport. The values obtained for the three PTLs at 35 and 55 °C with low and high catalyst loading are provided in Table 5.2. Apparent exchange current density generally decreases, while mass transport resistance increases, with increasing pore

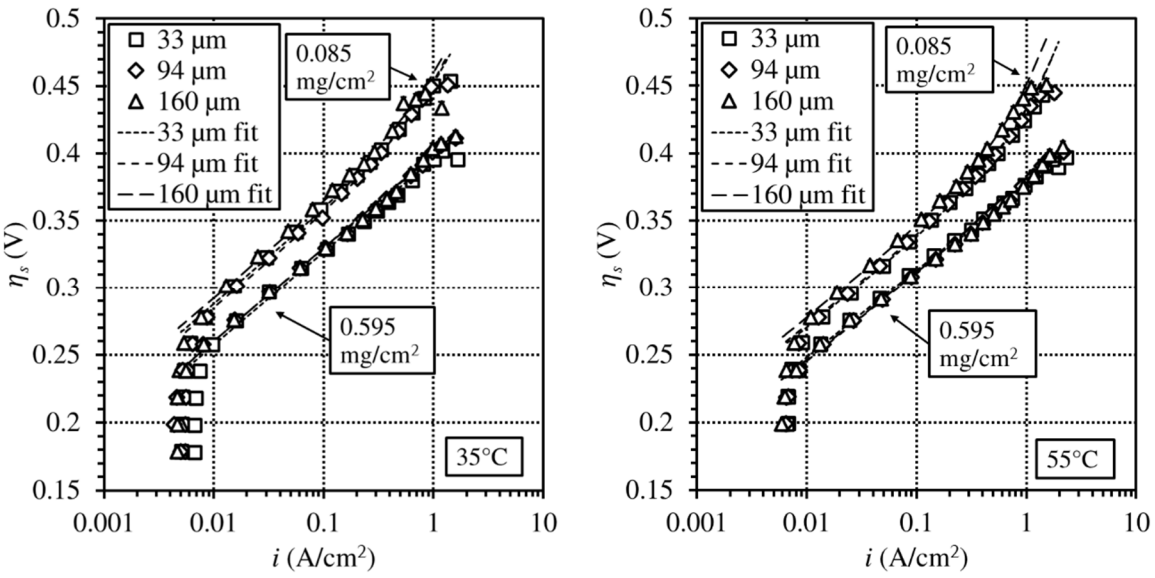

Figure 5.5: Tafel plots of surface overpotentials versus current density on a logarithmic scale for the three average pore opening diameters and catalyst loadings of 0.085 and 0.595 mg Ir cm^{-2}. Dashed lines show the fits used to determine i_0 and α (J. Lopata, et al. 2020).

Table 5.2: Apparent Exchange Current Densities and Mass Transport Resistances

T (°C)	Catalyst Loading (mg Ir cm^{-2})	APOD (μm)	AGSD (μm)	Apparent i_0 (A m^{-2})	R_{mt} (Ω m^{-2})
35	0.085	33	14	0.00722	0.006435
		94	31	0.00785	0.007666
		160	67	0.00625	0.007267
	0.595	33	14	0.0196	1.07e-07
		94	31	0.0181	3.65e-07
		160	67	0.0179	0.000297
55	0.085	33	14	0.00699	0.00819
		94	31	0.00656	0.00795
		160	67	0.00538	0.010907
	0.595	33	14	0.0148	7.41e-07
		94	31	0.0166	0.000781
		160	67	0.0161	0.000535

opening and PTL grain size at low catalyst loading. The relationships lack perfect clarity due to their practically unavoidable uncertainty.

At 0.085 mg Ir cm^{-2}, the Tafel plots are significantly more non-linear than at high catalyst loadings. In fact, it appeared that the benefit of slightly higher MEA temperature at moderate current densities between 1,000 and 10,000 A m^{-2} outweighed any detrimental effect that CL dehydration would have inflicted. The primary takeaway of Figure 5.5 is that at 0.085 mg Ir cm^{-2}, the Tafel plots with the three PTL materials are spaced apart more than at 0.595 mg Ir cm^{-2}, indicating that catalyst utilization was more sensitive to PTL surface properties as catalyst loading was reduced. Revisiting Figure 5.4, catalyst utilization appeared dependent on both in-plane conductivity of the CL within pore openings and mass transport between the pores and compressed spaces of the CL.

In PEMWE, CL dehydration can lead to two mechanisms through which the mass transport overpotential increases: reduction of ionomer conductivity and kinetic limitations at the catalyst surface. The experiments did not fully explain which of these mechanisms was dominant, but additional results may lead to reasonable speculation.

Feed Rate Sensitivity Results.

In Figure 5.6, two variables are plotted versus the stoichiometric feed rate, the bubble coverage and HFR. Upon reducing the stoichiometric feed rate from 2,000, both the apparent bubble coverage and the HFR decrease. For bubble coverage, it is suspected that the anode CL temperature is not very accurately represented by the outlet temperature or anode plate temperature near the outlet and the temperature may have been underestimated. The HFR outcome was understood to be due to the increase in cell temperature with decreasing feed rate, which increased the membrane conductivity and

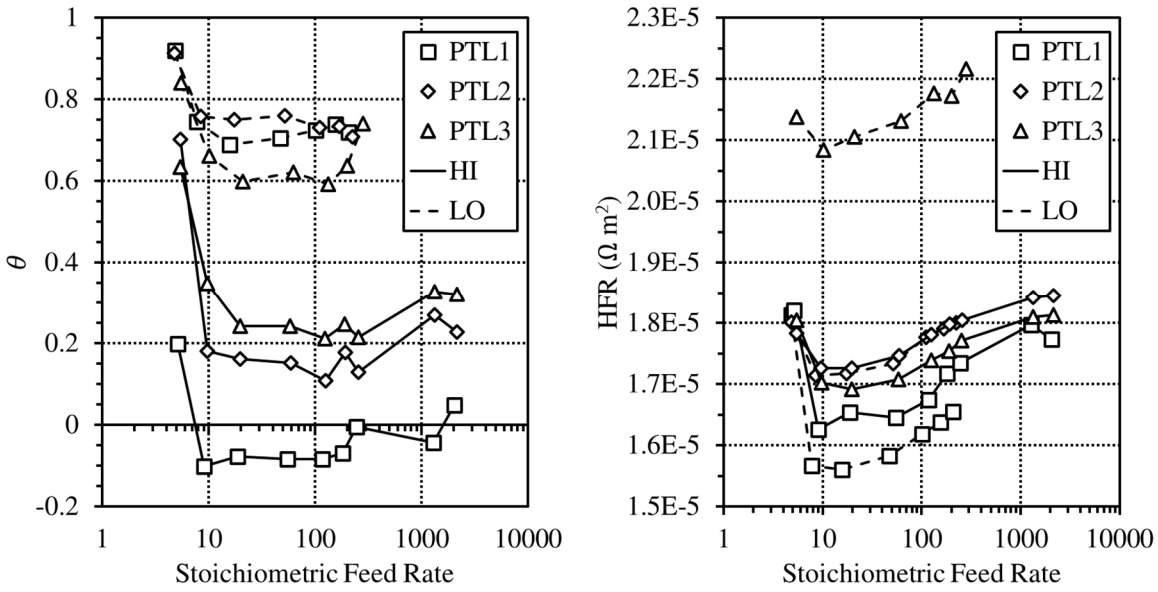

Figure 5.6: Bubble coverage at the anode and high-frequency resistance of the cell at a temperature setpoint of 55 °C with low feed rates using pore opening sizes of 33 μm (PTL1), 94 μm (PTL2), and 160 μm (PTL3) and catalyst loadings of 0.595 (HI) and 0.085 mg Ir cm^{-2} (LO).

may have also caused higher compression between the PTL and CL via membrane swelling. At extremely low stoichiometric feed rates of less than 20, both the apparent bubble coverage and the HFR increased sharply. While the apparent bubble coverage should not include any contribution from reduced catalyst utilization attributed to in-plane CL resistance, it does not provide any quantification of catalyst underutilization due to each the ionomer resistance and kinetic limitations. Figure 5.6 strongly suggests that catalyst underutilization is caused by an increase in resistance, but while this may be true to some extent, it may be an example of correlation having the appearance of causation. Knowledge of the rate order of the A-OER(G) strongly implies that kinetic limitations must be present if ionomer dehydration occurs. Simulations from Chapter 3 suggest that mass transport accounts for between 10 and 50 mV of the overpotential, depending on feed rate. This is in absence of the consideration of ionomer resistance or the heterogeneity of the PTL/CL interface. Experimental data shows a residual overpotential of between 95 and 110 mV, part of which is associated with kinetics limitations. The takeaway from this result is that concentration overpotentials and ionomer resistance overpotentials may be similar in magnitude.

In Figure 5.7, the Nyquist plots of the three PTLs at two different catalyst loadings and cell potentials under wet/wet conditions with 80 mL min^{-1} of liquid water feed at 55 °C are compared. At high catalyst loadings, there are no signs of diffusion-limited current for any material. This is not to say that kinetic limitations due to mass transport are not present, but that the current density is less than the limiting current density. Upon reducing the catalyst loading, diffusion impedance artifacts at low frequencies start to appear, becoming more prevalent with increasing cell potential and PTL particle surface size. This suggests

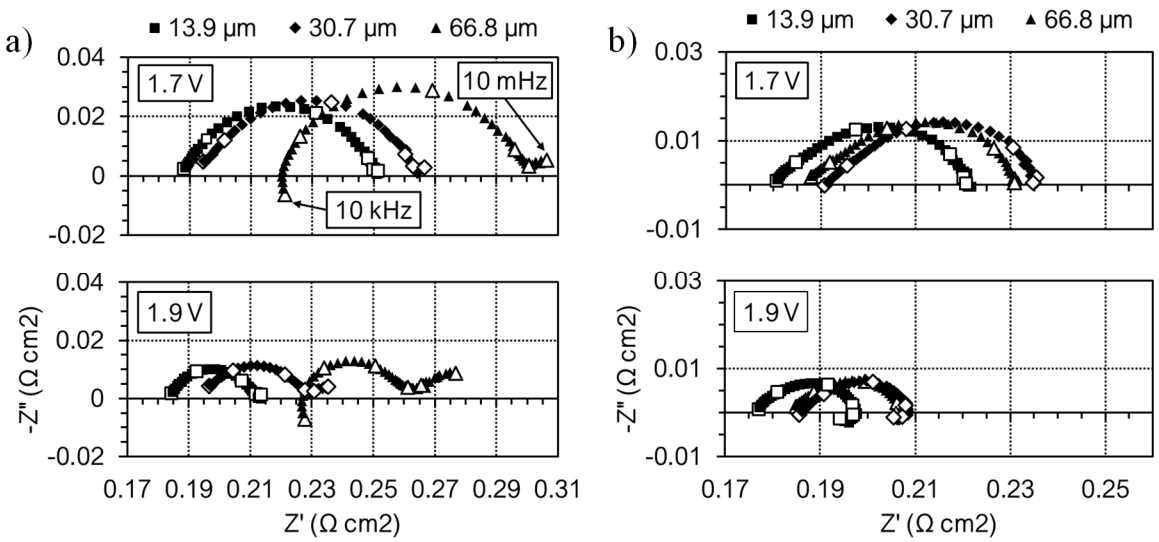

Figure 5.7: Nyquist plots describing cell impedance at 1.7 and 1.9 V with 80 mL min^{-1} feed to each electrode for the three PTLs at 55°C, a) 0.085 and b) 0.595 mg Ir cm^{-2}. Datasets span the frequency range logarithmically from 10 kHz to 10 mHz with enlarged, hollow points marking each decade. Grain sizes are given above the plots (J. Lopata, et al. 2020).

that the inhibition of water transport from the pore to the compressed regions of the anode CL is limiting the catalyst utilization. This behavior presents itself strongly when the CL is very thin and the distance from the PTL pores to reaction sites between the PTL particles and membrane are very long. The relative extents to which kinetic limitations and ionomer resistance limit catalyst utilization cannot be quantified with the experimental data presented, but it is strongly suggested that the two phenomena have comparable impacts, and neither one nor the other alone can explain mass transport overpotential.

CL Model for PEMWE

What limits catalyst utilization? Here, a 1D porous electrode approach is used to deconvolute the total mass transport overpotential into diffusion overpotential η_{diff} and ionomer resistance overpotential η_e. The governing equation is

$$-\sigma_e \frac{d^2\phi_e}{dz^2} = j_{\Pi} \tag{5.1}$$

$$j_{\Pi} = \sum_{\Pi} s_{\Pi} a^{\xi}_{w,wv,\Pi} j_0 \exp\left\{\frac{\alpha F \eta_{s,\Pi}}{\mathscr{R}T}\right\} \tag{5.2}$$

in which ϕ_e is the electrolyte potential. The right-hand side of Equation 5.2 is the sum of the current contributions of the liquid and gas phases. The terms of σ_e, the effective electrolyte conductivity, in Equation 5.3 is obtained from Yadav and Fedkiw for liquid water and water vapor and volume-weighted with a Bruggeman approximation:

$$\sigma_e = 100\, s_{e,S}^{1.5} \left(4.80713\, s \exp\left\{-\frac{10440}{\mathscr{R}T}\right\} + (0.6977\, h_r)^3 \exp\left\{-\frac{10440\, h_r^{-0.25}}{\mathscr{R}T}\right\} \right) \tag{5.3}$$

in which $s_{e,S}$ is the volume fraction of ionomer in the entire continuum. Writing Equation 5.1 in terms of one dependent variable ϕ_e one obtains,

$$-\sigma_e \frac{d^2\phi_e}{dz^2} = \sum_{\Pi} s_{\Pi} a_{w,wv,\Pi}^{\xi} j_0 \exp\left\{\frac{\alpha F\left(\phi_m - \phi_e - \phi_{eq,\Pi}^{red}\right)}{\mathscr{R}T}\right\} \tag{5.4}$$

To ease the solution process, Equation 5.4 is first expressed in its dimensionless form. The dimensionless variables are defined as

$$\phi^* = \frac{\alpha F}{\mathscr{R}T}\phi \tag{5.5}$$

$$z^* = z/L_{CL} \tag{5.6}$$

and the dimensionless form of Equation 5.4, assuming that the electron-conducting phase is much more conductive than the ionomer phase, is

$$\frac{d^2\phi_e^*}{dz^{*2}} = -\sum_{\Pi} \frac{s_{\Pi} a_{w,wv,\Pi}^{\xi} j_0 \alpha F L_{CL}^2}{\sigma_e \mathscr{R}T} \exp\left\{\phi_m^* - \phi_e^* - \phi_{eq,\Pi}^{red\,*}\right\} \tag{5.7}$$

which has exponential nonlinearity. This can be simplified under the assumption that ϕ_e^* does not deviate far from its value at $z^* = 1$, which is typically the case. The exponential term in Equation 5.7 can then be expressed as a first-order Taylor series approximation centered at $\phi_e^*|_{z^*=1}$, which is defined as 0:

$$\exp\left\{\left(\phi_m^* - \phi_e^* - \phi_{eq,\Pi}^{red*}\right)\right\} \cong (1 - \phi_e^*)\exp\left\{\phi_m^* - \phi_{eq,\Pi}^{red*}\right\} \tag{5.8}$$

Substituting the right-hand side of Equation 5.8 for the exponential in Equation 5.7, the ordinary differential equation becomes linear and expressed in terms of j_1^*, the dimensionless transfer current density at $z^* = 1$:

$$\frac{d^2\phi_e^*}{dz^{*2}} - j_1^{*2}\phi_e^* = -j_1^{*2} \tag{5.9}$$

$$j_1^{*2} = \sum_{\Pi} \frac{s_{\Pi} a_{w,wv,\Pi}^{\xi} j_0 \alpha F L_{CL}^2}{\sigma_e \mathscr{R}T} \exp\left\{\phi_m^* - \phi_{eq,\Pi}^{red*}\right\} \tag{5.10}$$

The solution to Equation 5.9 with $\vec{\imath}_e|_{z^*=0} = 0$ and $\phi_e^*|_{z^*=1} = 0$ is as follows:

$$\phi_e^* = 1 - \frac{\cosh\left\{j_1^* z^*\right\}}{\cosh\left\{j_1^*\right\}} \tag{5.11}$$

$$\frac{d\phi_e^*}{dz^*} = -\frac{j_1^* \sinh\left\{j_1^* z^*\right\}}{\cosh\left\{j_1^*\right\}} \tag{5.12}$$

$$\frac{d^2\phi_e^*}{dz^{*2}} = -\frac{j_1^{*2} \cosh\left\{j_1^* z^*\right\}}{\cosh\left\{j_1^*\right\}} \tag{5.13}$$

The average transfer current density is proportional to the second-order derivative:

$$j_{avg} = \frac{1}{L_{CL}} \int_0^{L_{CL}} -\frac{\sigma_e \mathscr{R}T}{\alpha F L_{CL}} \frac{d^2\phi_e^*}{dz^{*2}}\, dz^* \tag{5.14}$$

Integrating from 0 to L_{CL} by reducing the order of the derivative and applying the boundary condition at $z = 0$, the average transfer current density is

$$j_{avg} = -\frac{\sigma_e \mathscr{R}T}{\alpha F L_{CL}^2} j_1^* \tanh\left\{j_1^*\right\} \tag{5.15}$$

and the superficial current density is

$$\vec{\imath}_e|_{z=L_{CL}} = j_{avg} L_{CL} \tag{5.16}$$

The overall ionomer resistance overpotential is defined as

$$\eta_e = -\frac{\mathscr{R}T}{\alpha F} \int_0^1 \frac{d\phi_e^*}{dz^*} dz^* \tag{5.17}$$

which, when applying the boundary condition at $z^* = 1$, simplifies to

$$\eta_e = \frac{\mathscr{R}T}{\alpha F} \phi_e^*|_{z^*=0} \tag{5.18}$$

and therefore,

$$\eta_e = \frac{\mathscr{R}T}{\alpha F} \left(1 - \operatorname{sech}\left\{ \sqrt{\frac{\alpha F L^2}{\sigma_e \mathscr{R}T}} j_1^* \right\} \right) \tag{5.19}$$

The overall diffusion overpotential is a current-weighted average of liquid-phase volume fraction overpotential and gas-phase volume fraction and diffusion overpotentials. The

dimensionless A-OER(G) contribution is

$$\frac{i_G}{i_{tot}} = \left(1 + \frac{s}{1-s} h_r^{\frac{\alpha}{2}-2.07} \exp\left\{\phi_{eq,G} - \phi_{eq,L}\right\}\right)^{-1} \tag{5.20}$$

with $i_L/i_{tot} = 1 - i_G/i_{tot}$. η_{diff} is expressed as

$$\eta_{diff} = -\frac{\mathcal{R}T}{\alpha F}\left(\frac{i_G}{i_{tot}} \ln\left\{(1-s)h_r^{2.07-\frac{\alpha}{2}}\right\} + \frac{i_L}{i_{tot}} \ln\{s\}\right) \tag{5.21}$$

Comparing the two overpotentials gives something analogous to the Wagner number (normally the activation to electrolyte resistance overpotential ratio), which will be called the "modified Wagner number for mass transport", or Wa_{mt}:

$$Wa_{mt} = \eta_{diff}/\eta_e \tag{5.22}$$

This quantity describes the dominance of electroactive area reduction over ionomer resistance. A $Wa_{mt} > 1$ indicates that electroactive area reduction contributes most to catalyst underutilization. A $Wa_{mt} < 1$ indicates that ionomer resistance most significantly reduces catalyst utilization.

In Figure 5.8, $\log\{Wa_{mt}\}$ is shown to vary significantly with temperature, pressure, liquid saturation, relative humidity, CL thickness, and ionomer loading. Consider a case in which the CL potential drop is 1.575, temperature is 328.15 K, pressure is 1 bar, liquid saturation and relative humidity are both 0.5, the CL thickness is 5 μm, and j_0 is 26,000 A m^{-3}. Beginning a parametric study with Figure 5.8a, diffusion overpotential becomes more dominant with decreasing temperature, despite a reduction in ionomer conductivity. The higher equilibrium potential at low temperature results in lower surface overpotential, and the transfer coefficient decreases. An increase in pressure also causes higher $\log\{Wa_{mt}\}$ because the equilibrium potential increases. In addition to operating conditions, the anodic environment can contribute to the contributions of η_{diff} and η_e, as seen in Figure 5.8b.

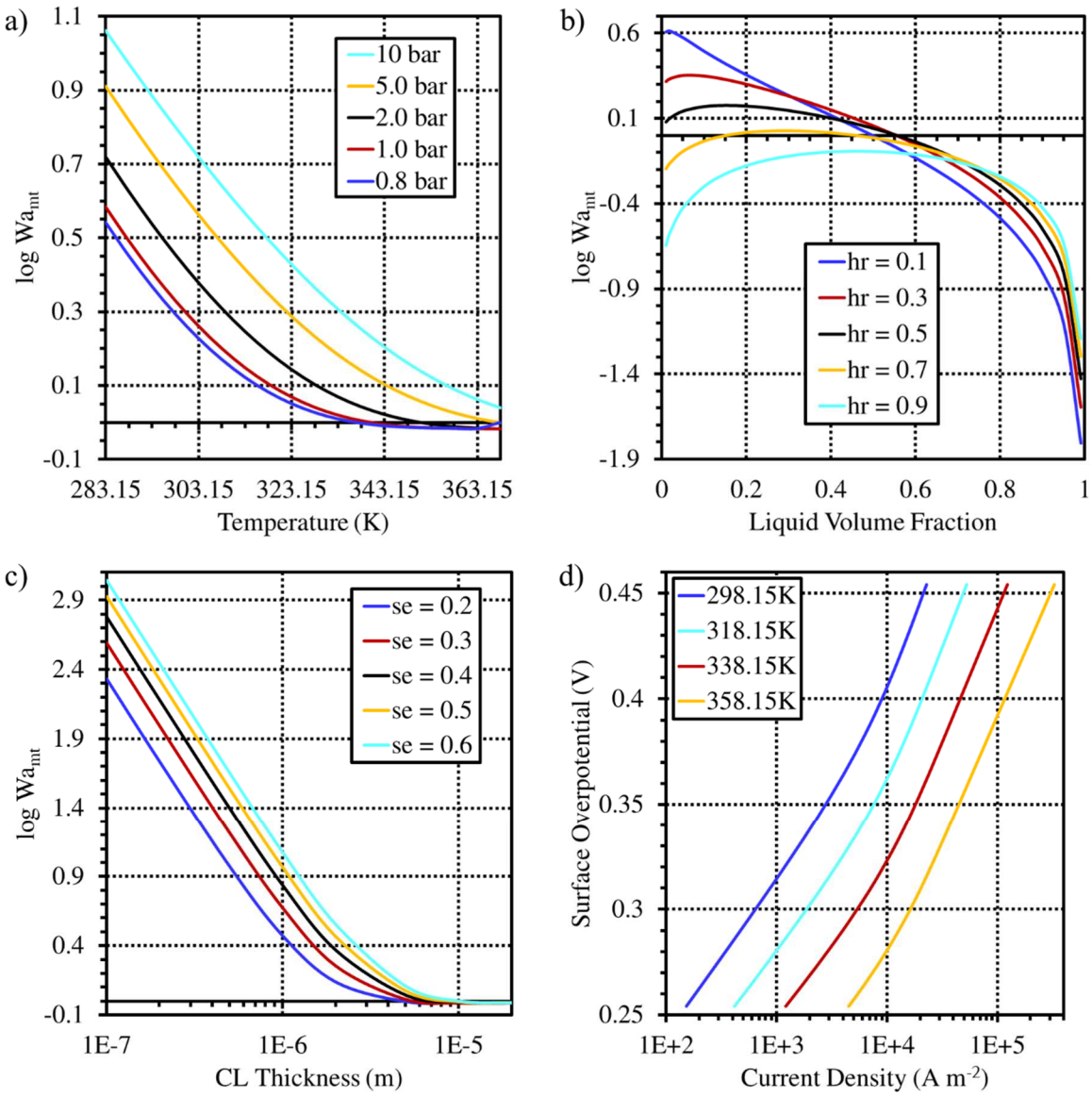

Figure 5.8: Parametric study of the 1D PEMWE CL model with a baseline case in which the values of temperature, pressure, liquid saturation, relative humidity, CL thickness, and ionomer volume fraction are 328.15 K, 1 bar, 0.5, 0.5, 5 μm, and 0.4, respectively. a) Change in log{Wa_{mt}} with temperature and pressure. b) Change in log{Wa_{mt}} with liquid saturation and relative humidity. c) Change in log{Wa_{mt}} with CL thickness and ionomer volume fraction. d) Tafel plots at various temperatures.

High liquid saturation leads to η_e becoming much greater than η_{diff}. The behavior at low liquid saturation depends on the relative humidity. At high relative humidity, ionomer resistance is the dominant mechanism leading to catalyst underutilization because kinetic limitations are small. At low relative humidity, the dominant mechanism is the kinetic limitation at the catalyst surface. When the liquid saturation is about 0.5, η_{diff} and η_e are similar in magnitude, at least for this set of parameters. Figure 5.8c shows that if the CL thickness is reduced, ionomer overpotential is quite small relative to the diffusion overpotential because the ion paths from reaction sites to the membrane are much shorter. The legend shows $s_{e,S}$. When the ionomer volume fraction increases, the effective conductivity increases, causing an increase in $\log\{Wa_{mt}\}$ for thin CLs. For CL thicknesses exceeding 10 μm, ionomer volume fraction has little to no impact. In Figure 5.8d, Tafel plots of surface overpotentials, essentially what are obtained from experiments, exhibit non-linearity similar to that in the experimental Tafel plots in Figure 5.5.

Porous electrode theory therefore supports the conclusion that mass transport overpotential arises from considerable magnitudes of ionomer resistance and diffusion overpotentials, the dominant one depending on operating conditions, the reaction environment, and CL specifications. A simple analytic 1D solution like the one investigated in this section can be applied to electrode interfaces in a 3D model, such as that from Chapter 3, with an empirically supported parameter set. The CL model is most needed when the CL is thick (> 1 μm) and the cell is simulated at high temperature and low pressure, in which case kinetic limitations and ionomer resistance have nearly equal effect.

In the next section, a similar model is applied to the electrode interfaces in the ADWE model from Chapter 4 in order to calculate the overall intraporous electrolyte resistance locally. More is done to account for the interfacial bottleneck resistance.

Electrode/Separator Interface Model for ADWE

In the introduction, the ESI in an ADWE cell was described using the mechanisms proposed by Hofmann (Hofmann 1980) and Dinkelacker (Dinkelacker 1988). A 2D axisymmetric model presented by de Groot and Vreman (de Groot 2020) provides much information about the effects of gap width and void fraction on the interfacial resistance via the restriction of cross-sectional area. A simple circuit model using porous electrode properties that blends Hofmann and Dinkelacker behavior at the ESI is proposed in this section for integration into 3D CFD models.

Governing Equations.

The proposed ESI model is a coupling of a 2D axisymmetric model of the porous diaphragm and a 1D electrode model comprising a circuit representation of the ESI. The ESI circuit consists of parallel resistances associated with the diaphragm space between pores ($R_{p,a,c}$) and between solid surfaces ($R_{m,a,c}$):

$$R_{esi,a,c} = \left(\frac{1}{R_{p,a,c}} + \frac{1}{R_{m,a,c}} \right)^{-1} - \frac{R_{ad}}{2} \tag{5.23}$$

with the subtraction of half the diaphragm resistance included to obtain the resistance of the electrode and ESI only.

Consider a diaphragm sandwiched between two porous electrodes in a zero-gap configuration. The diaphragm is in contact with the solid surfaces and pore openings of the porous electrodes. Similarly to de Groot and Vreman (de Groot 2020), the electric field within the diaphragm near a single pore can be modeled using a 2D axisymmetric model.

However, this model extends the scope to the opposite electrode, which may have different properties. The goal is to obtain a constant factor describing the bulge of the electric field between two pores, which is the ratio of the overall conductivity to the hypothetical conductivity of the diaphragm in the case of no electric field bulge. If the separator is much thinner than the diameter of the pore or the porous electrode has a surface porosity close to 1, the bulge parameter $B \approx 1$. The electric field is described by the 2D axisymmetric Poisson equation:

$$\frac{1}{r}\frac{\partial}{\partial r}\left(r\frac{\partial \phi}{\partial r}\right) + \frac{\partial^2 \phi}{\partial z^2} = 0 \tag{5.24}$$

Defining respectively the dimensionless potential, radius, and through-plane coordinate,

$$\phi^* = \frac{\phi - \phi_c}{\phi_a - \phi_c} \tag{5.25}$$

$$r^* = r/r_{max} \tag{5.26}$$

$$z^* = z/L_{ad} \tag{5.27}$$

a convenient expanded dimensionless form of Equation 5.24 is obtained:

$$\frac{\partial^2 \phi^*}{\partial r^{*2}} + \frac{1}{r^*}\frac{\partial \phi^*}{\partial r^*} + \mathcal{6}^2 \frac{\partial^2 \phi^*}{\partial z^{*2}} = 0 \tag{5.28}$$

$$\mathcal{6} = r_{max}/L_{ad} \tag{5.29}$$

$$r_{max} = \frac{r_{p,a} + r_{m,a} + r_{p,c} + r_{m,c}}{2} \tag{5.30}$$

in which $r_{p,a}$, $r_{m,a}$, $r_{p,c}$, and $r_{m,c}$ are the radii of the anode pore, annular anode matrix thickness, cathode pore radius, and annular cathode matrix thickness. The bulge parameter can be computed as a function of the integral of the z component of the potential gradient across the domain,

$$B = \frac{-2r_{max}}{r_{p,a} + r_{p,c}} \iint_{0\,0}^{1\,1} \frac{\partial \phi^*}{\partial z^*}\, d\phi^* dz^* \tag{5.31}$$

in which the factor preceding the double integral is the reciprocal of the dimensionless conductivity of the diaphragm without any bulge in the electric field. B is assumed to be a characteristic constant for the given diaphragm-electrode assembly so that the 2D axisymmetric model is no longer needed.

Hofmann and Dinkelacker behavior is determined through the use of a Hofmann parameter H and Dinkelacker function $\mathcal{D} = c_1 \exp\{-c_2 \vec{\imath}\} + c_3$. H describes the effect of bubble formation on the effective conductivity through the pore area. If $H = 0$, bubbles act only to impede ionic transport. However, in reality the bubbles generate micro-convection in their immediate vicinity (Hu, et al. 2021) which can diminish the ion-impeding effect. When $H = 1$, bubbles have no effect on ion transport through the pore area. $\mathcal{D}$ describes the effect of bubbles on the effective conductivity through the matrix area. When $\mathcal{D} = 0$, there is no ion transport from reaction sites in this area, and when $\mathcal{D} = 1$, there is no bubble coverage between the solid surfaces and the diaphragm.

The pore resistance is defined as a function of the sum of the electrode ionic resistance $R_{e,a,c}$ and half of the diaphragm resistance:

$$R_{p,a,c} = \frac{\frac{R_{ad}}{2} + R_{e,a,c}}{s^{1-H} \chi_{a,c} \mathcal{B}} \tag{5.32}$$

$$\chi_{a,c} = \frac{r_{p,a,c}^2}{\left(r_{p,a,c} + r_{m,a,c}\right)^2} \tag{5.33}$$

$$\mathcal{B} = B(1 - \mathcal{D}) + \mathcal{D} \tag{5.34}$$

while the matrix resistance is defined as

$$R_{m,a,c} = \frac{R_{ad}}{2\mathcal{D}(1-\chi_{a,c})} \tag{5.35}$$

Recall the porous electrode model described earlier that calculates the average transfer current density in a porous electrode with a highly conductive matrix phase. The overall ionic resistance of such an electrode is represented as follows:

$$R_{e,a,c} = \frac{L_{a,c}\left(\cosh\left\{j^*_{1,a,c}\right\}-1\right)}{\sigma_{eff,a,c}\, j^*_{1,a,c} \sinh\left\{j^*_{1,a,c}\right\}} \tag{5.36}$$

in which $L_{a,c}$ is the thickness of the anode or cathode. The dimensionless transfer current density at the ESI is

$$j^*_{1,a} = \frac{s a_w^2 i_{0,a} \alpha F L_a}{\sigma_e \mathcal{R} T} \exp\left\{\phi^*_m - \phi^{red*}_{eq,\Pi}\right\} \tag{5.37}$$

$$j^*_{1,c} = \frac{s a_{KOH} i_{0,c} \alpha F L_c}{\sigma_e \mathcal{R} T} \exp\left\{\phi^*_m - \phi^{red*}_{eq,\Pi}\right\} \tag{5.38}$$

The resistance in Equation 5.36 is applied to the ESI at the anode and cathode in the 3D ADWE model to observe the effects of the ESI resistance on the current distribution.

Discussion

Integrating the ESI model into the 3D ADWE simulation yields an interesting result. A plot of cell resistance versus current density, polarization curve, and distributions are provided in Figure 5.9 for 2.4 V operation with a balanced solution feed rate of 4.05 L min^{-1} to each electrode. Experimental data at low current densities gives the fitted semi-empirical function its shape. The function asymptotically approaches a set maximum resistance based on polarization curve fits to experimental data. Parameters used in the ESI model were determined using this fit. The result slightly underestimated current at high potential and slightly overestimated current at low potential, which was left as is for the scope of this investigation. The current density distribution, which is shown with a color

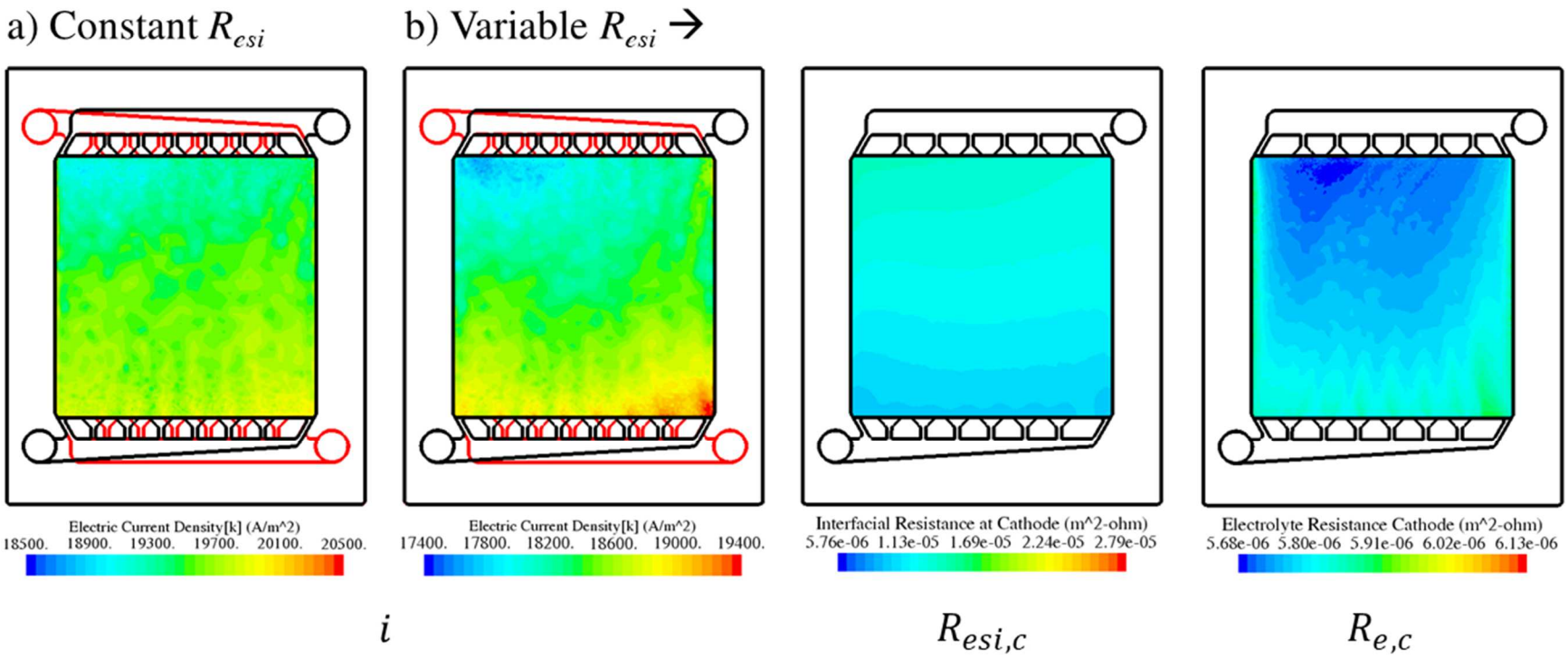

Figure 5.9: Effect of ESI resistance model on the current distribution with a balanced electrolyte feed rate of 4.05 L min^{-1} to each electrode. a) Current distribution under the constant ESI assumption (same as in Figure 4.8). b) Current distribution, total ESI resistance including the electrolyte, and the electrolyte resistance within the pores of the cathode with the ESI model applied to the separator interfaces. Current distributions are shown with color scales of similar size for comparison.

bar scale sized similarly to that of the simulation with a constant ESI assumption, is much more non-uniform with the ESI model. This is due to the increase in intraporous electrolyte resistance within the electrodes with increased void fraction. The bubbles generated in both reactions impede the migration of ions from cathode to anode. Void fractions and concentrations were affected minimally and are not shown as they are very similar to the constant ESI case from Figure 4.8. However, the ESI resistance distribution is provided for the cathode, which experiences higher void fractions than at the anode.

The purpose of deriving a fitted function for the ESI resistance was in part to determine quantitatively which theory best described ion transport in zero-gap alkaline water electrolyzers. In perforated plate cells with an electrolyte gap, which was explained in Chapter 1, Dinkelacker's theory describes the ion transport mechanism well. However, in zero-gap cells with porous metal foam electrodes, ions are more apt to travel through pore areas as suggested by Hofmann. In the ESI model, the Hofmann parameter was set to 0.87 and the Dinkelacker function reached a value of 0.09, indicating that ions had high propensity to travel through pore area and low propensity to travel in areas near the solid matrix in contact with the separator.

Another purpose of the ESI model was to capture the impact of ion migration through the electrolyte phase of the porous electrodes on the resistance, which is supposed to vary with void fraction. The overall resistance of the electrolyte phase within the porous electrodes was similar in magnitude to the resistance due to the reduction of ion transport area through the separator. Accounting for intraporous electrolyte resistance within the electrodes contributes quite noticeably to the current distribution because it the total ESI resistance is low near the inlet and high near the outlet. The intraporous electrolyte

resistance decreased with increasing void fraction because the transfer current shifted toward the separator, reducing the ion migration distances between the reaction sites and the separator.

CLOSING STATEMENTS

Several conditions are required for electrochemical hydrogen production from water. First, there must be an unimpeded pathway for ion migration between the electrocatalytic reaction sites of the anode and cathode. Then, at the endpoints of these pathways, ample water must be adjacent to the catalyst surface. The catalyst must be electrically connected to the external circuit. Finally, evolved gas must either be expelled swiftly to maintain the lowest possible void fraction or must maintain high relative humidity in order to promote the reaction of water vapor. The choice of the latter condition depends on the extent to which the gas phase impedes ion migration between the reaction site and the remainder of the ion pathway. In PEMWE, a high void fraction combined with high relative humidity is beneficial for performance. In ADWE, performance improves with higher solution feed rates, which forces evolved gases away from the electrode surface.

Electrolysis processes depend heavily on fluid flow, making them fair candidates for CFD study. In this work, a P2PM model was utilized, which led to stable solutions under severe water depletion conditions. The PEMWE model demonstrated that bulk porous media properties might have substantial effects on the anodic reaction environment. Bulk properties affect fluid flow within the PTL and the flow field, the liquid water content at the anode, the relative humidity, and likely the anode temperature. Evidently, PTLs can be designed to enhance cell performance by 5-10%.

In ADWE, at least for the cell design scrutinized in this work, manifold geometry impacts void fraction distributions and thereby current density. Calculated alterations to operating conditions can prevent the formation of gas pockets with high KOH concentrations, in this case within the porous cathode. Transport through the separator plays a role as well; when electroosmotic drag is dominant, solution crossover is almost exclusively from cathode to anode. When electroosmotic flow is dominant, solution crossover either diminishes or switches direction, which in this case caused more uniform KOH concentration. There are other important aspects of ADWE to consider, such as gas crossover and shunt current in stacks, that were highlighted herein.

A common theme among CFD models was that there is a kinetic limitation due to the presence of the gas phase. This is not a novel concept, but 3D simulations were able to quantify the magnitude of kinetic limitations across the anode. A major takeaway from the PEMWE model was that the A-OER(G) is likely less favorable at high liquid water feed rates due to low evaporation rates and relative humidity. Reducing the water content in a controlled, uniform manner in order to promote evaporation utilizes the high thermodynamic favorability of the A-OER(G) and enhances overall current density at constant cell potential.

The scientific community has been aware that there are energy losses at the interfaces between the separator/CCM and adjacent functional porous media. These arise due to charge and mass transport bottlenecks whose intensities depend on the porous structure at the surface in contact with the separator/CCM. In PEMWE, charge transport is limited by in-plane CL resistance within the PTL pore openings, dehydration of the proton-conducting ionomer between the PTL grains and the membrane, and the reduction of

effective electrochemical surface area of the catalyst. In ADWE, particularly in a zero-gap configuration, evolved gas easily becomes trapped between the solid matrix of the porous electrode and the separator. This reduces the cross-sectional area of ion transport through the interface as well as the separator. Resistance at this interface can be ameliorated by reducing the size of contact points between the solid and separator or leaving a microns-thick gap between the two components.

This work firmly adds that catalyst resistance, ionomer resistance, and kinetic limitations can all cause significant reduction in PEMWE catalyst utilization, and reducing the catalyst loading heightens the severity of all three by restricting both charge and mass transport in-plane. The dominant mechanism of catalyst utilization limitations depends on whether the reaction site is in a compressed region of the CL or within a PTL pore opening. In other words, the relative contributions of each source of energy loss depends on the location of the reaction site within the heterogeneous CL.

REFERENCES

Abdin, Z, C J Webb, and E MacA Gray. 2017. "Modelling and simulation of an alkaline electrolyser cell." *Energy* 138: 316-331. http://dx.doi.org/10.1016/j.energy.2017.07.053.

Aparicio-Mauricio, Gustavo, Francisca A. Rodríguez, Joep J. H. Pijpers, Martín R. Cruz-Díaz, and Eligio P. Rivero. 2020. "CFD modeling of residence time distribution and experimental validation in a redox flow battery using free and porous flow." *Journal of Energy Storage* 29: 101337. https://doi.org/10.1016/j.est.2020.101337.

Arbabi, F., H. Montazeri, R. Abouatallah, R. Wang, and A. Bazylak. 2016. "Three-Dimensional Computational Fluid Dynamics Modelling of Oxygen Bubble Transport in Polymer Electrolyte Membrane Electrolyzer Porous Transport Layers." *Journal of The Electrochemical Society* 163 (11): F3062-F3069. doi:10.1149/2.0091611jes.

Babic, Ugljesa, Thomas J Schmidt, and Lorenz Gubler. 2018. "Communication-Contribution of Catalyst Layer Proton Transport Resistance to Voltage Loss in Polymer Electrolyte Water Electrolyzers." *Journal of The Electrochemical Society* 165: J3016-J3018. http://dx.doi.org/10.1149/2.0031815jes.

Balzer, R J, and H Vogt. 2003. "Effect of Electrolyte Flow on the Bubble Coverage of Vertical Gas-Evolving Electrodes." *Journal of The Electrochemical Society* 150 (1): E11-E16.

Brauns, Jörn, Jonas Schönebeck, Mikkel R. Kraglund, David Aili, Jaromír Hnát, Jan Žitka, Willem Mues, Jens O. Jensen, Karel Bouzek, and Thomas Turek. 2021. "Evaluation of Diaphragms and Membranes as Separators for Alkaline Diaphragm Water Electrolysis." *Journal of The Electrochemical Society* 168: 014510. https://doi.org/10.1149/1945-7111/abda57.

Carmo, Marcelo, David L Fritz, Jurgen Mergel, and Detlef Stolten. 2013. "A comprehensive review on PEM water electrolysis." *International Journal of Hydrogen Energy* 38: 4901-4934. http://dx.doi.org/10.1016/j.ijhydene.2013.01.151.

Chemical Rubber Company (CRC). 1992. *Aqueous Solutions of Electrolytes.* Boca Raton, FL: CRC Press, Inc.

Chemical Rubber Company (CRC). 1984. *CRC Handbook of Chemistry and Physics.* 65. Edited by R. C. Weast. Boca Raton, FL: CRC Press, Inc.

Choi, Pyoungho, Dmitri G Bessarabov, and Ravindra Datta. 2004. "A simple model for solid polymer electrolyte (SPE) water electrolysis." *Solid State Ionics* 175: 535-539. doi:10.1016/j.ssi.2004.01.076.

Costanza-Robinson, Molly S., and Mark L. Brusseau. 2002. "Air-water interfacial areas in unsaturated soils: Evaluation of interfacial domains." *Water Resources Research* 38 (10): 1195. doi:10.1029/2001WR000738.

Crane Company. 1988. "Flow of fluids through valves, fittings, and pipe." Technical paper.

de Groot, Matheus T, and Albertus W Vreman. 2021. "Ohmic resistance in zero gap alkaline electrolysis with a Zirfon diaphragm." *Electrochimica Acta* 369: 137684. https://doi.org/10.1016/j.electacta.2020.137684.

Debe, M. K., S. M. Hendricks, G. D. Vernstrom, M. Meyers, M. Brostrom, M. Stephens, Q. Chan, J. Willey, M. Hamden, and C. K. Mittelsteadt. 2012. "Initial performance and durability of ultra-low loaded NSTF electrodes for PEM electrolyzers." *Journal of The Electrochemical Society* 159: K165-K176.

Dedigama, Ishanka, Pangiota Angeli, Nicholas van Dijk, Jason Millichamp, Dimitrios Tsaoulidis, Paul R Shearing, and Daniel J L Brett. 2014. "Current density mapping and optical flow visualization of a polymer electrolyte membrane water electrolyzer." *Journal of Power Sources* 265: 97-103. http://dx.doi.org/10.1016/j.jpowsour.2014.04.120.

Dinkelacker, M. 1989. "Gas evolution and bubble formation on electrodes. Zur Gasentwicklung und Blasenbildung an Elektroden." Germany.

Dunlap, P. M., and S. M. Faris. 1962. "Surface tension of aqueous solutions of potassium hydroxide." *Nature* 196: 1312-1313.

Eigeldinger, J, and H Vogt. 2000. "The bubble coverage of gas-evolving electrodes in a flowing electrolyte." *Electrochimica Acta* 45: 4449-4456.

El Ouni, Asma, Bo Guo, Hua Zhong, and Mark L. Brusseau. 2021. "Testing the validity of the miscible-displacement interfacial tracer method for measuring air-water interfacial area: Independent benchmarking and mathematical modeling." *Chemosphere* 263: 128193. https://doi.org/10.1016/j.chemosphere.2020.128193.

Felder, R. M., and R. W. Rousseau. 2005. *Elementary Principles of Chemical Processes.* 3. Hoboken, NJ: John Wiley & Sons, Inc.

González-Buch, C., I. Herraiz-Cardona, E. Ortega, J. García-Antón, and V. Pérez-Herranz. 2013. "Synthessis and characterization of macroporous Ni, Co, and Ni-Co electrocatalytic deposits for hydrogen evolution reaction in alkaline media." *International Journal of Hydrogen Energy* 38: 10157-10169. http://dx.doi.org/10.1016/j.ijhydene.2013.06.016.

Grigoriev, S A, P Millet, S A Volobuev, and V N Fateev. 2009. "Optimization of porous current collectors for PEM water electrolyzers." *International Journal of Hydrogen Energy* 34: 4968-4973. doi:10.1016/j.ijhydene.2008.11.056.

Hammoudi, M, C Henao, K Agbossou, Y Dube, and M L Doumbia. 2012. "New multi-physics approach for modelling and design of alkaline electrolyzers." *International Journal of Hydrogen Energy* 37: 13895-13913. http://dx.doi.org/10.1016/j.ijhydene.2012.07.015.

Hansen, M. K., D. Aili, E. Christensen, C. Pan, S. Eriksen, J. O. Jensen, J. H. Von Barner, Q. Li, and N. J. Bjerrum. 2012. "PEM steam electrolysis at 130°C using a phosphoric acid doped short side chain PFSA membrane." *International Journal of Hydrogen Energy* 37: 10992-11000.

Haverkort, J. W. 2020. "Modeling and Experiments of Binary Electrolytes in the Presence of Diffusion, Migration, and Electro-Osmotic Flow." *Physical Review Applied* 14: 044047. http://dx.doi.org/10.1103/PhysRevApplied.14.044047.

Henao, Christian, Kodjo Agbossou, Mhamed Hammoudi, Yves Dube, and Alben Cardenas. 2014. "Simulation tool based on a physics model and an electrical analogy for an alkaline electrolyser." *Journal of Power Sources* 250: 58-67. http://dx.doi.org/10.1016/j.jpowsour.2013.10.086.

Hine, F, M Yasuda, R Nakamura, and T Noda. 1975. "Hydrodynamic Studies of Bubble Effects on the IR-Drops in a Vertical Rectangular Cell." *Journal of The Electrochemical Society* 122 (9): 1185-1190.

Hofmann, H. 1980. Dissertation, Darmstadt.

Hu, Qian, Hong-bo Liu, Ze Liu, Dinghan Zhong, Jiaxin Han, and Liang-ming Pan. 2021. "A pair of adjacent bubbles evolution at micro-electrode under electrode-normal magnetic field." *Journal of Electroanalytical Chemistry* 880: 114886. http://dx.doi.org/10.1016/j.jelechem.2020.114886.

Hung, Chi-Yuan, Sheng-De Li, Cheng-Chien Wang, and Chuh-Yung Chen. 2012. "Influences of a bipolar membrane and an ultrasonic field on alkaline water electrolysis." *Journal of Membrane Science* 389: 197-204. dx.doi.org/10.1016/j.memsci.2011.10.050.

Immerz, C., B. Bensmann, P. Trinke, M. Suermann, and R. Hanke-Rauschenbach. 2018. "Local Current Density and Electrochemical Impedance Measurements within 50 cm Single-Channel PEM Electrolysis Cell." *Journal of The Electrochemical Society* 165 (16): F1292-F1299. doi:10.1149/2.0411816jes.

Immerz, Christoph, Boris Bensmann, Patrick Trinke, Michel Suermann, and Richard Hanke-Rauschenbach. 2019. "Ortsaufgeloste Stromdichtemessung in PEM-Elektroyse-Zellen." *Chemie Ingenieur Technik* 91: 907-918. doi:10.1002/cite.201800175.

Ito, Hiroshi, Tetsuhiko Maeda, Akihiro Nakano, Atsushi Kato, and Tetsuya Yoshida. 2013. "Influence of pore structural properties of current collectors on the performance of proton exchange membrane electrolyzer." *Electrochimica Acta* 100: 242-248. dx.doi.org/10.1016/j.electacta.2012.05.068.

Kadyk, Thomas, David Bruce, and Michael Eikerling. 2016. "How to Enhance Gas Removal from Porous Electrodes?" *Scientific Reports* 6: 38780. doi:10.1038/srep38780.

Kampmeyer, P. M. 1952. "The temperature dependence of viscosity for water and mercury." *Journal of Applied Physics* 23: 99-102.

Kang, Zhenye, Gaoqiang Yang, Jingke Mo, Shule Yu, David A Cullen, Scott T Retterer, Todd J Toops, et al. 2018. "Developing titanium micro/nano porous layers on planar thin/tunable LGDLs for high-efficiency hydrogen production." *International Journal of Hydrogen Energy* 43: 14618-14628. https://doi.org/10.1016/j.ijhydene.2018.05.139.

Kang, Zhenye, Jingke Mo, Gaoqiang Yang, Scott T Retterer, David A Cullen, Todd J Toops, Johney B Green Jr, Matthew M Mench, and Feng-Yuan Zhang. 2017b. "Investigation of thin/well-tunable liquid/gas diffusion layers exhibiting superior multifunctional performance in low-temperature electrolytic water splitting." *Energy & Environmental Science* 10: 166-175. doi:10.1039/c6ee02368a.

Kang, Zhenye, Jingke Mo, Gaoqiang Yang, Yifan Li, Derrick A Talley, Bo Han, and Feng-Yuan Zhang. 2017a. "Performance Modeling and Current Mapping of Proton Exchange Membrane Electrolyzer Cells with Novel Tin/Tunable Liquid/Gas Diffusion Layers." *Electrochimica Acta* 255: 405-416. https://doi.org/10.1016/j.electacta.2017.09.170.

Kang, Zhenye, Shule Yu, Gaoqiang Yang, Yifan Li, Guido Bender, Bryan S Pivovar, Johney B Green Jr, and Feng-Yuan Zhang. 2019. "Performance improvement of proton exchange membrane electrolyzer cells by introducing in-plane transport enhancement layers." *Electrochimica Acta* 316: 43-51. https://doi.org/10.1016/j.electacta.2019.05.096.

Kell, George S. 1975. "Density, Thermal Expansivity, and Compressibility of Liquid Water from 0° to 150°C: Correlations and Tables for Atmospheric Pressure and Saturation Reviewed and Expressed on 1968 Temperature Scale." *Journal of Chemical and Engineering Data* 20 (1): 97-105.

Kibria, M. F., and M. S. Mridha. 1996. "Electrochemical studies of the nickel electrode for the oxygen evolution reaction." *International Journal of Hydrogen Energy* 21: 179-182. https://doi.org/10.1016/j.jpowsour.2013.05.041.

Kienzlen, V, D Haaf, and W Schnurnberger. 1994. "Location of Hydrogen Gas Evolution on Perforated Plate Electrodes in Zero Gap Cells." *International Journal of Hydrogen Energy* 19 (9): 729-732.

Lafmejani, Saeed S., Anders C. Olesen, and Søren K. Kær. 2017. "VOF modelling of gas-liquid flow in PEM water electrolysis cell micro-channels." *International Journal of Hydrogen Energy* 42: 16333-16344. http://dx.doi.org/10.1016/j.ijhydene.2017.05.079.

Lal, S., A. Lamibrac, J. Eller, and F. N. Büchi. 2018. "Determination of water evaporation rates in gas diffusion layers of fuel cells." *Journal of The Electrochemical Society* 165: F652-F661.

Le Bideau, D., P. Mandin, M. Benbouzid, M. Kim, and M. Sellier. 2019. "Review of necessary thermochemical properties and their sensitivities with temperature and electrolyte mass fractions for alkaline water electrolysis multiphysics modelling." *International Journal of Hydrogen Energy* 44: 4553-4569. https://doi.org/10.1016/j.ijhydene.2018.12.222.

Lee, C. H., B. Zhao, R. Abouatallah, R. Wang, and A. Bazylak. 2019. "Compressible-Gas Invasion into Liquid-Saturated Porous Media: Application to Polymer-Electrolyte-Membrane Electrolyzers." *Physical Review Applied* 11: 054029. https://doi.org/10.1103/PhysRevApplied.11.054029.

Lee, Hae I., Dao T. Dung, Jieun Kim, Jae H. Pak, Sang K. Kim, Hyun S. Cho, Won C. Cho, and Chang H. Kim. 2020a. "The synthesis of a Zirfon-type porous separator with reduced gas crossover for alkaline electrolyzer." *International Journal of Energy Research* 44: 1875-1885.

Lee, Hae I., Muhammad Mehdi, Sang K. Kim, Hyun S. Cho, Min J. Kim, Won C. Cho, Young W. Rhee, and Chang H. Kim. 2020b. "Advanced Zirfon-type porous separator for a high-rate alkaline electrolyser operating in a dynamic mode." *Journal of Membrane Science* 616: 118541.

Lemmon, E. W., M. O. McLinden, and D. G. Friend. 2017. "Thermophysical Properties of Fluid Systems." In *NIST Chemistry WebBook*, edited by P. J. Linstrom and W. G. Mallard. Gaithersburg, MD: National Institute of Standards and Technology.

LeRoy, Rodney L, and Christopher T Bowen. 1980. "The Thermodynamics of Aqueous Water Electrolysis." *Journal of The Electrochemical Society* 127 (9): 1954-1962.

Leverett, M. C. 1940. "Capillary Behavior in Porous Solids." *AIME*. Tulsa. 152-169.

Li, Z., and K. S. Pitzer. 1996. "Thermodynamics of aqueous KOH over the full range to saturation and to 573 K." *Journal of Solution Chemistry* 25: 813-821. http://refhub.elsevier.com/S0013-4686(21)01092-6/sbref0055.

Liu, Chang, Marcelo Carmo, Guido Bender, Andreas Everwand, Thomas Lickert, James L. Young, Tom Smolinka, Detlef Stolten, and Werner Lehnert. 2018. "Performance enhancement of PEM electrolyzers through iridium-coated titanium porous transport layers." *Electrochemistry Communications* 97: 96-99. https://doi.org/10.1016/j.elecom.2018.10.021.

Lopata, J. S., S-G. Kang, H-S. Cho, C-H. Kim, J. W. Weidner, and S. Shimpalee. 2021a. "Investigating influence of geometry and operating conditions on local current, concentration, and crossover in alkaline water electrolysis using computational fluid dynamics." *Electrochimica Acta* 390: 138802. https://doi.org/10.1016/j.electacta.2021.138802.

Lopata, J., Z. Kang, J. Young, G. Bender, J. W. Weidner, and S. Shimpalee. 2020. "Effects of the Transport/Catalyst Layer Interface and Catalyst Loading on Mass and Charge Transport Phenomena in Polymer Electrolyte Membrane Water Electrolysis Devices." *Journal of The Electrochemical Society* 167: 064507. https://doi.org/10.1149/1945-7111/ab7f87.

Lopata, Joseph, John W. Weidner, H-S. Cho, N. Tippayawong, and S. Shimpalee. 2022. "Evidence of Improved PEM Water Electrolysis Performance via Facilitating the Gas-Phase Oxygen Evolution Reaction." Manuscript submitted for publication, Department of Chemical Engineering, University of South Carolina.

Lopata, Joseph, Z. Kang, J. Young, G. Bender, John W. Weidner, H-S. Cho, and S. Shimpalee. 2021b. "Resolving Anodic Current and Temperature Distributions in a Polmer Electrolyte Membrane Water Electrolysis Cell Using a Pseudo-Two-Phase Computational Fluid Dynamics Model." *Journal of The Electrochemical Society* 168: 054518. https://doi.org/10.1149/1945-7111/abfe7b.

Marrero, Thomas R. 1970. "Gaseous Diffusion Coefficients. A Comprehensive Critical Evaluation of Experimental Studies and Correlations of Results." Dissertation, University of Maryland, College Park, MD.

Mat, Mahmut D, Kemal Aldas, and Olusegun J Ilegbusi. 2004. "A two-phase flow model for hydrogen evolution in an electrochemical cell." *International Journal of Hydrogen Energy* 29: 1015-1023. doi:10.1016/j.ijhydene.2003.11.007.

Mazúr, Petr, Jakub Polonský, Martin Paidar, and Karel Bouzek. 2012. "Non-conductive TiO2 as the anode catalyst support for PEM water electrolysis." *International Journal of Hydrogen Energy* 37: 12081-12088.

Mo, Jingke, Zhenye Kang, Gaoqiang Yang, Yifan Li, Scott T Retterer, David A Cullen, Todd J Toops, et al. 2017. "In situ investigation on ultrafast oxygen evolution reactions of water spltting in proton exchange membrane electrolyzer cells." *Journal of Materials Chemistry A* 5: 18469-18475. doi:10.1039/c7ta05681h.

Mo, Jingke, Zhenye Kang, Scott T Retterer, David A Cullen, Todd J Toops, Johney B Green Jr., Matthew M Mench, and Feng-Yuan Zhang. 2016. "Discovery of true electrochemical reactions for ultrahigh catalyst mass activity in water splitting." *Science Advances* 2: e1600690. doi:10.1126/sciadv.1600690.

Mularczyk, Adrian, Andreas Michalski, Michael Striednig, Robert Herrendörfer, Thomas J. Schmidt, Felix N. Büchi, and Jens Eller. 2021. "Mass Transport Limitations of

Water Evaporation in Polymer Electrolyte Fuel Cell Gas Diffusion Layers." *Energies* 14: 2967. https://doi.org/10.3390/en14102967.

Nagai, N, M Takeuchi, T Kimura, and T Oka. 2003. "Existence of optimum space between electrodes on hydrogen production by water electrolysis." *International Journal of Hydrogen Energy* 28: 35-41.

2004. "Concentrated Solutions." Chap. 12 in *Electrochemical Systems*, by John Newman and Karen E. Thomas-Alyea, 297-316. Hoboken, NJ: John Wiley & Sons, Inc.

Ni, Meng, Michael K H Leung, and Dennis Y C Leung. 2008. "Energy and exergy analysis of hydrogen production by a proton exchange membrane (PEM) electrolyzer plant." *Energy Conversion and Management* 49: 2748-2756. doi:10.1016/j.enconman.2008.03.018.

Nouri-Khorasani, Amin, Emile Tabu Ojong, Tom Smolinka, and David P Wilkinson. 2017. "Model of oxygen bubbles and performance impact in the porous transport layer of PEM water electrolysis cells." *International Journal of Hydrogen Energy* 42: 28665-28680. https://doi.org/10.1016/j.ijhydene.2017.09.167.

Novotný, P., and O. Söhnel. 1988. "Densities of binary aqueous solutions of 306 inorganic substances." *Journal of Chemical and Engineering Data* 33: 49-55.

Olesen, Anders C., Carsten Rømer, and Søren K. Kær. 2016. "A numerical study of the gas-liquid, two-phase flow maldistribution in the anode of a high pressure PEM water electrolysis cell." *International Journal of Hydrogen Energy* 41: 52-68. http://dx.doi.org/10.1016/j.ijhydene.2015.09.140.

Onda, Kazuo, Toshio Murakami, Takeshi Hikosaka, Misaki Kobayashi, Ryouhei Notu, and Kohei Ito. 2002. "Performance Analysis of Polymer-Electrolyte Water Electrolysis Cell at a Small-Unit Test Cell and Performance Prediction of Large Stacked Cell." *Journal of The Electrochemical Society* 149 (8): A1069-A1078. doi:10.1149/1.1492287.

Reigel, H., J. Mitrovic, and K. Stephan. 1998. "Role of mass transfer on hydrogen evolution aqueous media." *Journal of Applied Electrochemistry* 28: 10-17.

Rodríguez, Jesús, Simonetta Palmas, Margarita Sánchez-Molina, Ernesto Amores, Laura Mais, and Roberto Campana. 2019. "Simple and Precise Approach for Determination of Ohmic Contribution of Diaphragms in Alkaline Water Electrolysis." *MDPI Membranes* 9 (129). http://dx.doi.org/10.3390/membranes9100129.

Satjaritanun, P., M. O'Brien, D. Kulkarni, S. Shimpalee, C. Capuano, K. E. Ayers, N. Danilovic, D. Y. Parkinson, and I. V. Zenyuk. 2020. "Observation of Preferential Pathways for Oxygen Removal through Porous Transport Layers of Polymer Electrolyte Water Electrolyzers." *iScience* 23: 101783. https://doi.org/10.1016/j.isci.2020.101783.

Schalenbach, Maximilian, Wiebke Lueke, and Detlef Stolten. 2016. "Hydrogen Diffusivity and Electrolyte Permeability of the Zirfon PERL Separator for Alkaline Water Electrolysis." *Journal of The Electrochemical Society* 14: F1480-F1488. http://dx.doi.org/10.1149/2.1251613jes.

Schuler, Tobias, Ruben De Bruycker, Thomas J Schmidt, and Felix N Büchi. 2019. "Polymer Electrolyte Water Electrolysis: Correlating Porous Transport Later Structural Properties and Performance: Part I. Tomographic Analysis of Morphology and Topology." *Journal of The Electrochemical Society* 166: F270-F281. http://dx.doi.org/10.1149/2.0561904jes.

Schuler, Tobias, Taro Kimura, Thomas J Schmidt, and Felix N Büchi. 2020. "Towards a generic understanding of oxygen evolution reaction kinetics in polymer electrolyte water electrolysis." *Energy and Environmental Science* 13: 2153-2166. doi:10.1039/d0ee00673d.

Schuler, Tobias, Thomas J Schmidt, and Felix N Büchi. 2019. "Polymer Electrolyte Water Electrolysis: Correlating Performance and Porous Transport Layer Structure: Part II. Electrochemical Performance Analysis." *Journal of The Electrochemical Society* 166: F555-F565. http://dx.doi.org/10.1149/2.1241908jes.

See, Dawn M., and Ralph E. White. 1997. "Temperature and Concentration Dependence of the Specific Conductivity of Concentrated Solutions of Potassium Hydroxide." *Journal of Chemical and Engineering Data* 42: 1266-1268.

Shimpalee, S., P. Satjaritanun, S. Hirano, N. Tippayawong, and J. W. Weidner. 2019. "Multiscale Modeling of PEMFC Using Co-Simulation Approach." *Journal of The Electrochemical Society* 166 (8): F534-F543. doi:10.1149/2.0291911jes.

Springer, T. E., T. A. Zawadzinski, and S. Gottesfeld. 1991. "Polymer Electrolyte Fuel Cell Model." *Journal of The Electrochemical Society* 138 (8): 2334-2342.

Steiner, Myles A., Collin D. Barraugh, Chase W. Aldridge, Isabel Barraza Alvarez, Daniel J. Friedman, Nicholas J. Ekins-Daukes, Todd G. Deutsch, and James L. Young. 2019. "Photoelectrochemical water splitting using strain-balanced multiple quantum well photovoltaic cells." *Sustainable Energy & Fuels* 3 (10): 2837. https://doi.org/10.1039/C9SE00276F.

Toghyani, S., E. Afshari, and E. Baniasadi. 2018. "Metal foams as flow distributors in comparison with serpentine and parallel flow fields in proton exchange membrane electrolyzer cells." *Electrochimica Acta* 290: 506-519.

Toghyani, S., E. Afshari, E. Baniasadi, and S. A. Atayabi. 2018. "Thermal and electrochemical analysis of different flow field patterns in a PEM electrolyzer." *Electrochimica Acta* 267: 234-245. https://doi.org/10.1016/j.electacta.2018.02.078.

Toghyani, Somayeh, Ebrahim Afshari, and Ehsan Baniasadi. 2019. "Three-dimensional computational fluid dynamics modeling of proton exchange membrane electrolyzer

with new flow field pattern." *Journal of Thermal Analysis and Calorimetry* 135: 1911-1919. https://doi.org/10.1007/s10973-018-7236-5.

Trinke, P., P. Haug, J. Brauns, B. Bensmann, R. Hanke-Raucshenbach, and T. Turek. 2018. "Hydrogen Crossover in PEM and Alkaline Water Electrolysis: Mechanisms, Direct Comparison and Mitigation Strategies." *Journal of The Electrochemical Society* 165 (7): F502-F513. http://dx.doi.org/10.1149/2.0541807jes.

Udell, K. S. 1983. "Heat transfer in porous media heated from above with evaporation, condensation, and capillary effects." *ASME Journal of Heat Transfer* 105: 485-492.

Ulleberg, Øystein. 2003. "Modeling of advanced alkaline electrolyzers: a system simulation approach." *International Journal of Hydrogen Energy* 28: 21-33.

Ursúa, Alfredo, Luis M. Gandía, and Pablo Sanchis. 2012. "Hydrogen Production From Water Electrolysis: Current Status and Future Trends." *Proceedings of the IEEE*. 410-426. doi:10.1109/JPROC.2011.2156750.

Vogt, H. 1990. "The Concentration Overpotential of Gas Evolving Electrodes as a Multiple Problem of Mass Transfer." *Journal of The Electrochemical Society* 137 (4): 1179-1184.

Vogt, H, and R J Balzer. 2005. "The bubble coverage of gas-evolving electrodes in stagnant electrolytes." *Electrochimica Acta* 50: 2073-2079. doi:10.1016/j.electacta.2004.09.025.

Wang, Chao-Yang, and C. Beckermann. 1993. "A two-phase mixture model of liquid-gas flow and heat transfer in capillary porous media - I. Formulation." *International Journal of Heat and Mass Transfer* 36 (11): 2747-2758.

White, Ralph E., C. W. Walton, H. S. Burney, and R. N. Beaver. 1986. "Predicting Shunt Currents in Stacks of Bipolar Plate Cells." *Journal of The Electrochemical Society* 133 (3): 485-492.

Yadav, R., and P. S. Fedkiw. 2012. "Analysis of EIS Technique and Nafion 117 Conductivity as a Function of Temperature and Relative Humidity." *Journal of the Electrochemical Society* 159 (3): B340-B346.

Ye, Feng, Jianling Li, Xindong Wang, Tongtao Wang, Shanmei Li, Haojie Wei, Qingfeng Li, and Erik Christensen. 2010. "Electrocatalytic properties of Ti/Pt-IrO2 anode for oxygen evolution in PEM water electrolysis." *International Journal of Hydrogen Energy* 35 (15): 8049-8055.

Zawodzinski Jr., Thomas A., Charles Derouin, Susan Radzinski, Ruth J. Sherman, Van T. Smith, Thomas E. Springer, and Shimshon Gottesfeld. 1993. "Water Uptake by and Transport Through Nafion® 117 Membranes." *Journal of The Electrochemical Society* 140: 1041.

Zeng, Kai, and Dongke Zhang. 2010. "Recent progress in alkaline water electrolysis for hydrogen production and applications." *Progress in Energy and Combustion Science* 36 (3): 307-326. https://doi.org/10/1016/j.pecs.2009.11.002.

Zenyuk, I. V., A. Lamibrac, J. Eller, D. Y. Parkinson, F. Marone, F. N. Büchi, and Adam Z. Weber. 2016. "Investigating Evaporation in Gas Diffusion Layers for Fuel Cells with X-ray Computed Tomagraphy." *Journal of Physical Chemistry C* 120 (50): 28701-28711. https://doi.org/10.1021/acs.jpcc.6b10658.

APPENDIX A

PHYSICAL INTERPRETATION OF VECTOR INVERSION APPLIED TO GRADIENTS

A so-called “scalar quotient” analogous to the scalar product formally defined in linear algebra is defined geometrically here. The definition of the scalar product is:

$$\boldsymbol{a} \cdot \boldsymbol{b} = \|\boldsymbol{b}\| \, proj\{\boldsymbol{a}, \boldsymbol{b}\} \tag{A.1}$$

Therefore, the scalar quotient would be

$$\boldsymbol{a} \div \boldsymbol{b} = \frac{proj\{\boldsymbol{a}, \boldsymbol{b}\}}{\|\boldsymbol{b}\|} = \frac{\boldsymbol{a} \cdot \boldsymbol{b}}{\|\boldsymbol{b}\|^2} \tag{A.2}$$

It is common to consider vectors non-invertible because they lack a universal identity (though the unit vector is sufficient), but the operations defined here are sufficient for the task at hand. Though inconsistent with orthodox linear algebra, $\boldsymbol{a} \div \boldsymbol{b}$ could be expressed as $\boldsymbol{a} \cdot \boldsymbol{b^{-1}}$ in which $\boldsymbol{b^{-1}} = \boldsymbol{b}/\|\boldsymbol{b}\|^2$. A “slash” quotient $\boldsymbol{a/b} = \boldsymbol{a} \times \boldsymbol{b^{-1}}$ could also be defined given due reason.